ABSTRACT

COHEN, SEAN E. A Numerical Investigation into the Expansion of a Plasma Plume due to Ablation of a Graphite Target by a Nano-second Laser Pulse. (Under the direction of Dr. Alina Chertock.)

This thesis is concerned with the implementation of an effective numerical method to solve the laser ablation problem modeled by fluid dynamic equations and, thereafter, numerically investigate the behavior of the solutions as a result of varying physical and numerical parameters. Sharp results are obtained that effectively simulate the expansion of the plasma plume resulting from the nano-second laser pulse using both the Navier-Stokes equations and the quasi-gas dynamic equations. In particular, we are able to simulate the one-dimensional expansion with a wide array of parameters. Numerically, we determine parameters that most effectively balance efficiency with accuracy. We also run numerical experiments that test a wide array of physical parameters and note their effects on the behavior of the solutions. The two-dimensional, and quasi two-dimensional, simulations provide great insight to the behavior of the plasma expansion as well as a vital tool in the computation of the laser ablation problem.

In Chapters 2 and 3 we study the one-dimensional problem. Our objectives include the implementation of a numerical method that efficiently handles the problem while providing the desired accuracy. With the numerical method set, we then turn our attention to documenting the effects of the numerical parameters involved in the approximation. Of great concern is the influence of the relaxation parameter controlling the viscosity and thermal diffusion in the quasi-gas dynamic mathematical model. We are able to produce results with a varied range of physical parameters. In particular, we are able to implement initial conditions that more realistically mimic the physical experiments. The results are found to be in agreement with physical experiments. Since such experiments are expensive and difficult to perform, we are able to gain insight into the behavior of the expansion under disparate configurations.

Chapters 4 and 5 present results of our exploration into the two-dimensional problem. With an efficient one-dimensional numerical scheme under our belts, we are able to simulate the highly computationally demanding two-dimensional problem. We first present the quasi-two dimensional radially symmetric model. This model simplifies the two-dimensional model by treating the angular dimension in the polar coordinate realization as constant. In this way we are able to simulate a two-dimensional problem while working in only one dimension. We then tackle the full two-dimensional problem. The results show the effectives of the quasi-gas dynamics model in providing an appropriate amount of smoothing in order to efficiently and accurately realize solutions. This numerical scheme is of great importance and interest to the scientists studying laser ablation.

A Numerical Investigation into the Expansion of a Plasma Plume due to Ablation of a Graphite Target by a Nano-second Laser Pulse

by
Sean E Cohen

A dissertation submitted to the Graduate Faculty of
North Carolina State University
in partial fulfillment of the
requirements for the Degree of
Doctor of Philosophy

Applied Mathematics

Raleigh, North Carolina

2011

APPROVED BY:

Dr. Zhilin Li	Dr. Michael Shearer
Dr. Pierre Gremaud	Dr. Alina Chertock Chair of Advisory Committee

DEDICATION

To my beautiful wife Susie and our lovely children, Eva and Ezra. Thank you for making it through this with me and for rooting me along the entire way. To my wonderful parents and sister, for always believing in my ability to succeed. To my gracious and skilled advisor, Alina Chertock, for her strength in motivating me to push on and her expertise and knowledge.

BIOGRAPHY

The author was born in Miami Beach, FL and was raised in northwest Broward County. He attended the University of Florida, where he entered into the Electrical Engineering program. After graduating, the call of the mountains and travel led him out west, spending the winter in Colorado and the following summer traveling throughout the western states. It was then that the decision to study mathematics blossomed. In particular, a theoretical linear algebra class had opened his eyes to the beauty of mathematics.

His future wife joined him in Vermont, where his education in Mathematics began in earnest. After earning a master's degree in Mathematics at the University of Vermont, the two headed to California to start a hemp clothing business and live in the mountains of Lake Tahoe. Although mathematical opportunities were scarce, there was tutoring. After marrying, we bought a house in North Carolina house and began making children.

In Asheville, the author taught mathematics at the University of North Carolina Asheville as an adjunct instructor. It is here where his passion for teaching blossomed. The camaraderie of the mathematics department made a great impression on the author and he began to focus on striving towards graduate school. North Carolina State University offered the best opportunity for he and his family. The author's interest in applied mathematics and, in particular, climate dynamics and computer simulations directed him towards numerical analysis, partial differential equations and stochastic processes.

ACKNOWLEDGEMENTS

It is my pleasure to thank the many people who helped make this thesis possible.

First and foremost, I would like to express my deepest gratitude to my Ph.D. advisor, Dr. Alina Chertock. This thesis would not have been possible without her guidance, motivation, and expertise. From my first semester of graduate school she has been my mentor. Throughout my thesis-writing period, she has provided superb teaching, great direction, and excellent company.

Besides my advisor, I would like to thank the rest of my thesis committee: Dr. Michael Shearer, Dr. Zhilin Li, and Dr. Pierre Gremaud for their encouragement, insight, and knowledge. I will always look back on my education with fond memories of you.

It is an honor for me to thank my classmates whose collaboration and bravery in the face of the epic challenge that is graduate mathematics helped me stay on target, focus my strengths, and overcome my weaknesses. In particular, Karen Bliss, Adam Attarian, Amanda Criner, and Minshiung Li.

Also, a heartfelt acknowledgement to my friends and family who have supported me throughout this endeavor.

I am grateful for the financial support provided by the National Science Foundation.

Finally, I would like to thank my family. My wife Susie and children Eva and Ezra have provided me with the emotional support to complete this work. My sister Nicoelle for always being available with advice and support. And my parents Eddie and Patricia Cohen for providing me with life, love, and happiness.

TABLE OF CONTENTS

LIST OF TABLES

LIST OF FIGURES

Chapter 1

Introduction

The computation of laser ablation is an area of research that encompasses many important topics of mathematics, including mathematical modeling, numerical methods for partial differential equations (PDEs), and data analysis. Laser ablation is the process of removing material from a solid surface by irradiating it with a laser beam. The action of the short laser pulse striking the target results in a high-pressure, high-temperature region near the target which then expands into the low pressure region. There are many applications, including laser drilling where it is possible to drill small, deep holes through very hard materials, and removing coatings from a surface without damaging the underlying surface. Applications are found in dentistry and laser machinery. The process of laser ablation can also produce a plasma - a partially ionized gas with free electrons - which itself has many applications. Among these applications are growing thin films and bulk crystals. A plasma bunch appears as a result of the laser pulse striking the target material, which in this thesis is taken to be carbon. The plasma expands into the surrounding atmosphere and covers the substrate in a thin film. The film's quality is largely determined by the velocity of the carbon flow. Shock waves, which are likely to occur due to the low pressure setting, are detrimental to the film quality. The shock wave decelerates the motion of the carbon flow, or even reverses part of the flow. Controlling the velocity of the shock wave front is an important problem in the growth of thin films.

The physical problem being modeled here is the expansion of the plasma metamorphized by the ablation of the target material. The nanosecond laser pulse strike results in an extremely high-temperature, high-pressure plasma that expands into the surrounding atmosphere according to the laws of fluid dynamics. After the laser strike, the high temperature and high pressure laser blast transforms the strike material into a plasma. The plasma expands from the high energy region into the surrounding low pressure, low temperature atmosphere. The evolution of this expansion can be modeled by the Navier-Stokes (NS) equations. Due to the computational difficulties inherent in these equations, a variation of the Navier-Stokes equations has

been proposed in [72]. This so-called quasi-gas dynamic (QGD) system is derived in [35]. The main component of the QGD equations that differs from the NS equations is the addition of a relaxation parameter that controls the additional dissipative terms provided by the QGD model and has the dimension of time. For performing simulations, these extra terms can be used to control the amount of artificial viscosity introduced to increase the computational stability. The derivation of the system is presented in detail in Chapter 2. For now, let us note that the difference between NS and QGD is that while the NS equations use spatial averaging at the kinetic description, QGD is derived using both spatial and temporal averaging. The time averaging leads to a loss in the conservation of momentum that is expressed in terms of the relaxation parameter.

Some of the challenges that laser ablation poses to computation include the need to handle large gradients in the initial conditions, accurate resolution and location of shocks that can occur depending on physical parameters, and reducing computational cost so that multi-dimensional models may be computed. The need for accurate computation of laser ablation is acutely necessary in the study of plasma expansion. Unfortunately, the huge pressure and temperature jump between the relatively tiny strike region and the surrounding atmosphere tends to wreak havoc on numerical schemes. Of course, we can produce results for this problem with standard finite difference schemes. However, stability constraints on the time evolution are prohibitive. Also, the spatial mesh grids that must be constructed to handle the implementation of the initial value problem limit the numerical experiments which scientists would like to carry out. These huge computational costs also inhibit the implementation of higher dimensional models.

The computation of laser ablation using the QGD equations was carried out in [72], [115]. The problem was solved using standard second-order finite differences in space and first-order forward differences in time. Besides the excessive smoothing of shock fronts, the scheme is computationally expensive. Monte Carlo direct simulation of the gas dynamics is used to investigate the expansion of the laser plume into a buffer gas in [46]. In [54], a hybrid model is developed to study the expansion. The early stages of computation ignore diffusion and use a macroscopic description of the expansion. Afterwards, diffusion and energy exchange are taken into account, and the expansion is described using a microscopic approach computed by direct Monte Carlo simulation. Also, models for different applications have been developed. E.g., in [32], a pseudo one-dimensional model is developed for laser drilling which elegantly, efficiently, and accurately measures the drilling depth. The process is assumed to be axis-symmetric. Non-dimensionalizing the heat transfer shows that radial diffusion is negligible relative to the vertical diffusion. Radial averaging provides the one-dimensional formulation.

By utilizing a semidiscrete finite-volume method we are able to cut the spatial mesh grid size by over ninety percent. Also, the semidiscrete scheme allows us to implement efficient ODE solvers which allow for larger time steps. The computational savings then allow for a

thorough numerical investigation of the physical problem, the model's parameters, and even the parameters associated with the numerical scheme. The implementation of the two-dimensional model gives us a broader, and previously not available, picture of the physical expansion of the ablated plasma modeled using the quasi-gas dynamics equations. The numerical results imply that the plasma behaves in very much the same way as a gas or fluid. The ability to represent the expansion of the plasma using the equations of fluid dynamics points to this relationship. Furthermore, the initial conditions of the numerical problem (representing the laser strike as a "dam-break" problem) imply that the expansion of the plasma is driven by forces created by the relatively, extremely high-pressure, high-temperature strike zone.

There are several goals to this numerical investigation. The first goal is to implement a stable method that greatly reduces the cost of computation. The desired result is a method whose computational savings allow it to be applied to multi-dimensional QGD models. In particular, we want to gain the efficiency needed to solve the two-dimensional problem. The second goal is to more accurately resolve the shocks that are present in the solutions, including their locations. The finite volume method employed is able to accurately capture the behavior of the shock evolution. The resolution of the shocks is greatly increased over the finite difference method. In the binary gas problem, the surrounding atmosphere is taken to be nitrogen. Extra terms are included to couple the interaction between the gases. Previous computations of this problem were marred by excessive smoothing of the shocks and inaccuracy in the location of shock wave propagating through the nitrogen atmosphere. In particular, there was a delay in the appearance of the shock which should coincide with the propagation of the carbon jet. These deficiencies are corrected using the numerical scheme employed here. The third goal is to be able to handle more physically relevant initial conditions. When initial pressure conditions in the strike zone are raised to values coinciding with those from physical experiments, previous computations were only able to resolve solutions when the initial pressure in the surrounding atmosphere is kept unreasonably high. The numerical method employed here is able to resolve solutions for these conditions even as the initial pressure in the surrounding atmosphere drops towards zero. Also, we are able to test other modifications to the initial conditions such as adjusting the size of the strike zone. Finally, we introduce analysis of the relaxation parameter by studying the behavior of solutions as the value of this parameter approaches zero. We also provide results for the computation of laser ablation with the NS equations, which coincides with removal of the QGD diffusive terms. This computation has been previously difficult to carry out with the severe restrictions due to stability concerns.

The method employed here provides a computational advantage and the ability to conduct complete numerical investigations that were previously unobtainable, such as the two-dimensional modeling. It also provides the efficiency and accuracy needed by researchers. In the following, we describe conservation laws and the numerical methods used to approximate

them.

1.1 Mathematical Models

The study of the flow of fluids is important in a variety of scientific applications, among which are atmospheric sciences, aerodynamics, nuclear physics, and pollution control. The formulation of the equations describing the dynamics of fluid flow stand among the greatest achievements in science. Among the many excellent references on fluid dynamics are [3, 11, 29, 89, 63]. When we speak of the flow of fluids we typically have in mind one of two states of matter, liquids or gases. These states of matter differ from solids in that they do not have a preferred shape. The removal of a shear force applied to a solid will result in its returning to its original shape. I.e, the solid is perfectly elastic. Fluids however will deform continuously when acted upon by a shear force. We say that the fluid flows.

There are also two distinct conceptual ways of viewing and describing fluid flow. They are derived from the scale of observation. In particular we can observe phenomena at the microscopic level or the macroscopic level. In the microscopic, or statistical, description, the fluid flow is predicted by the interaction of individual molecules. At this level of description the fundamental variables are the position, mass and velocity of each individual molecule. The macroscopic, or continuum, description of a fluid flow is that of fluid particles moving along stream lines. The stream lines are the integral curves of the velocity field

Although it is possible to study the flow of a fluid by studying the interaction of the molecules by which it is comprised, we are concerned with the gross movement of the fluid. I.e., we are concerned with the continuum description of the flow.

This description is derived from the three fundamental conservation principles, which are

1. Conservation of mass
2. Conservation of momentum
3. Conservation of energy

We now provide a description of general conservation laws.

1.1.1 Systems of Conservation Laws

A system of conservation laws in multi-dimensions can be represented in the general form

$$\frac{\partial \mathbf{w}}{\partial t} + \sum_{k=1}^{d} \frac{\partial}{\partial x_k} \mathbf{f}_k(\mathbf{w}) = 0, \tag{1.1}$$

where $\mathbf{w}$ is an m-vector consisting of the quantities of interest, $\mathbf{x} = (x_1, \ldots, x_d)^T$, and the flux functions, $\mathbf{f}_k : \mathbb{R}^m \to \mathbb{R}^m$ for $k = 1, \ldots, d$, are at least continuously differentiable. The flux functions are generally nonlinear. In practice, $\mathbf{x}$ is the spatial variable and $d = 1, 2$ or 3. For example, if $d = 2$, then $\mathbf{x} = (x, y)^T$ and

$$\frac{\partial \mathbf{w}}{\partial t} + \frac{\partial}{\partial x}\mathbf{f}_1(\mathbf{w}) + \frac{\partial}{\partial y}\mathbf{f}_2(\mathbf{w}) = 0. \tag{1.2}$$

The derivation of conservation laws follows from the fact that in a physical system, the quantity being measured is conserved as the system evolves. Some examples of conserved quantities are mass, momentum, energy, and electric charge. The conservation law is derived by noting that any change of one of these conserved quantities in some region can only result from a net change in flux of the quantity into or out of the region [111], [92]. Suppose that $\Omega \in \mathbb{R}^d$ is a bounded domain inside the fluid and $\partial\Omega$ is its smooth boundary. Let us consider density given by $\rho(\mathbf{x}, t)$. Then the amount of ρ in the region Ω is given by the volume integral,

$$\int_\Omega \rho(\mathbf{x}, t) d\mathbf{x}. \tag{1.3}$$

Since the quantity ρ is conserved, its value only changes due to fluid entering or exiting the region. The rate at which the mass is exiting the region is given by $\tilde{\mathbf{f}}(\rho) \cdot \mathbf{n}$, where $\mathbf{n}$ is the unit outward normal on the boundary and $\tilde{\mathbf{f}} = (\tilde{f}_1(\rho), \tilde{f}_2(\rho), \ldots, \tilde{f}_d(\rho))$, where $\tilde{f}_k$ is the flux of ρ in the x_k-direction, $k = 1, \ldots, d$. Therefore,

$$\frac{d}{dt}\int_\Omega \rho(\mathbf{x}, t) d\mathbf{x} = -\int_{\partial\Omega} \tilde{\mathbf{f}}(\rho) \cdot \mathbf{n}\, dS, \tag{1.4}$$

where dS is the surface measure on the boundary $\partial\Omega$. The negative sign indicates that the change in mass decreases if the net flow is outwards. The divergence theorem states that the outward flux of a quantity through its boundary is equal to the volume integral of the divergence of that quantity inside the region. I.e.,

$$\int_{\partial\Omega} \tilde{\mathbf{f}}(\rho) \cdot \mathbf{n}\, dS = \int_\Omega \nabla \cdot \tilde{\mathbf{f}}(\rho) d\mathbf{x}. \tag{1.5}$$

Thus, we can deduce that

$$\int_\Omega \left(\frac{\partial \rho}{\partial t} + \nabla \cdot \tilde{\mathbf{f}}(\rho) \right) d\mathbf{x} = 0. \tag{1.6}$$

Since Ω is an arbitrary region and the integrand is a continuous function, we obtain the general form for conservation laws given in (1.1). Equation (1.1) is supplied with appropri-

ate initial and boundary conditions. In particular, the Riemann problem consists of initial conditions which are constant in different regions.

A linear system of partial differential equations (PDEs) in one spatial dimension can be written as

$$\mathbf{w}_t + A\mathbf{w}_x = 0, \tag{1.7}$$

where $\mathbf{w}$ is defined above in (1.1) and A is the $m \times m$ matrix of constant coefficients. Note that the subscript notation used here indicates the partial derivative in the indicated direction and will be used interchangeably. If A is diagonalizable with real eigenvalues, then we say the system of PDEs, (1.7), is *hyperbolic*. Furthermore, if the eigenvalues are distinct, we say the system is *strictly hyperbolic*. For linear systems in one dimension the diagonalizability of the matrix A gives rise to the decoupling of the equations. This lends itself to writing the solution as a linear combination of m waves traveling at constant speeds given by the eigenvalues of A.

In two or more dimensions we need this hyperbolicity condition to be satisfied not only for each of the coefficient matrices, but also for any linear combination of these matrices. For example, in two dimensions we have

$$\mathbf{w}_t + A\mathbf{w}_x + B\mathbf{w}_y = 0. \tag{1.8}$$

Then we say the system is hyperbolic if the matrix $\tilde{A} = \alpha A + \beta B$ is diagonalizable with real eigenvalues for all $\alpha, \beta \in \mathbb{R}$.

For nonlinear systems the situation becomes more complicated as solutions generally involve shock and/or rarefaction waves. In one dimension we can rewrite (1.1) as

$$\mathbf{w}_t + \mathbf{f}_1(\mathbf{w})_x = 0. \tag{1.9}$$

Furthermore, we can write this system in the following quasi-linear form:

$$\mathbf{w}_t + A(\mathbf{w})\mathbf{w}_x = 0, \tag{1.10}$$

where $A(\mathbf{w})$ is the Jacobian matrix consisting of the partial derivatives of the m components of the flux function, $\mathbf{f}_1 = (f_{11}, f_{12}, \ldots, f_{1m})^T$, with respect to the components of the solution. I.e.,

$$A(\mathbf{w}) = \begin{pmatrix} \frac{\partial f_{11}}{\partial w_1} & \cdots & \frac{\partial f_{11}}{\partial w_m} \\ \vdots & \vdots & \vdots \\ \frac{\partial f_{1m}}{\partial w_1} & \cdots & \frac{\partial f_{1m}}{\partial w_m} \end{pmatrix} \tag{1.11}$$

A one-dimensional nonlinear system of PDEs is hyperbolic at a point (x,t) if the Jacobian matrix $A(\mathbf{w})$ is diagonalizable with real eigenvalues at said point. Similar to above, in multi-dimensions we need any linear combination of the Jacobian matrices of the flux functions $\mathbf{f}_k,\ k=1,\ldots,d$ to be a diagonalizable matrix with real eigenvalues. The quasi-linear system (1.10) is hyperbolic in a region if it satisfies this hyperbolicity condition for all $\mathbf{w}$ in the region. We strongly recommend [77], [114] and [41] for details on hyperbolic systems of PDEs. Further general information on PDEs can be found in [99, 92, 111, 119, 57] and specifically on hyperbolic PDEs in [25, 37, 40, 84, 53, 116, 104, 101].

Characteristic curves are curves in the solution space along which the PDE becomes an ordinary differential equation (ODE). The union of the solutions, the integral surface, of the ODEs that pass through the initial curve, which itself must not be a characteristic curve, is the solution of the PDE. This is best imagined as flowing out from each point of the given initial curve along the characteristic curve that passes through this point. In linear problems these curves are parallel and their slopes, characteristic speeds, are given by the eigenvalues of the coefficient matrix. In nonlinear problems the eigenvalues of the Jacobian matrices depend on the solution, in which case the initial data is distorted as the solution evolves. So, as the solution evolves we see regions on the wave that move faster or slower than other regions resulting in compression or expansion. If two characteristics intersect, then we are faced with the quandary that the solution has different values at the same point. This is imagined as the integral surface folding over on itself. Thus, we can no longer speak of derivatives of the solution at these points.

Instead of giving up at this, we turn our attention to the weak form of the partial differential equation. In this manner we may speak of discontinuous solutions.

We call $\mathbf{w}(\mathbf{x},t)$ a weak solution of (1.1), if

$$\int_0^\infty \int_\Omega (\mathbf{w}\phi_t + \sum_{k=1}^{d} \mathbf{f}_k(\mathbf{w}) \frac{\partial \phi}{\partial x_k}) d\mathbf{x}dt = -\int_\Omega \mathbf{w}(\mathbf{x},0)\phi(\mathbf{x},0)d\mathbf{x}, \tag{1.12}$$

for all $\phi(\mathbf{x},t) \in C_0^1$, i.e., ϕ is smooth and has compact support.

As mentioned above, shocks occur when two characteristics carrying conflicting information meet. Let Σ be a surface separating Ω into two regions, Ω_1 and Ω_2. Let $\mathbf{w}|_{\Omega_1} = \mathbf{w}_1$ and $\mathbf{w}|_{\Omega_2} = \mathbf{w}_2$ be the constant initial states in each region. Then $\mathbf{w}$ is a weak solution of equation (1.1) if and only if it is a classical solution in both Ω_1 and Ω_2, and the Rankine-Hugoniot jump condition, see [92, 77], holds along Σ. The Rankine-Hugoniot jump condition is given by

$$n_t[\mathbf{w}] + \sum_{k=1}^{d} n_{x_k}[\mathbf{f}_k(\mathbf{w})] = 0. \tag{1.13}$$

where the unit normal vector is given by $\mathbf{n} = (n_t, n_{x_1}, \ldots, n_{x_d})$. Here we have the jump of the

solution across Σ given by

$$[\mathbf{w}] = \mathbf{w}_2 - \mathbf{w}_1, \tag{1.14}$$

and the jump of the flux functions is given by

$$[\mathbf{f}_k(\mathbf{w})] = \mathbf{f}_k(\mathbf{w}_2) - \mathbf{f}_k(\mathbf{w}_1). \tag{1.15}$$

In one dimension ($d = 1$), we can represent the surface Σ by $(t, \xi(t))$, and (1.13) can be written as

$$s[\mathbf{w}] = [\mathbf{f}_1(\mathbf{w})], \tag{1.16}$$

where $s = \frac{d\xi}{dt}$ is the speed at which the discontinuity propagates. For linear systems, the shock speed becomes the eigenvalue of the coefficient matrix corresponding with the eigenvector representing the jump in initial states. Note, this implies a specific relationship between the initial states for a shock to occur.

The entropy condition is used to determine whether a weak solution is the physically correct solution. The condition ensures that the characteristic curves behave correctly. Physically, this is related to the expansion of gases and that the energy of the expansion is overtaking that which is in front of it.

For the scalar conservation law in one-dimension ($w_t + f_{11}(w)_x = 0$), the Lax entropy condition, see, e.g., [92, 77], states that a discontinuity propagating with speed s given by (1.16) satisfies the entropy condition if

$$f'_{11}(w_1) > s > f'_{11}(w_2). \tag{1.17}$$

One of the ways to obtain an entropy solution is by considering the vanishing viscosity problem, which is given by

$$\frac{\partial \mathbf{w}}{\partial t} + \sum_{k=1}^{d} \frac{\partial}{\partial x_k} \mathbf{f}_k(\mathbf{w}) = \epsilon \triangle \mathbf{w}. \tag{1.18}$$

The hyperbolic problem, of course, breaks down as a differential equation when a shock forms. In (1.18), $\epsilon > 0$ is a small parameter. We expect the solutions to this parabolic problem to approach the hyperbolic solution as $\epsilon \to 0$. Near discontinuities, where the spatial derivatives become very large, the viscosity term $\epsilon \triangle \mathbf{w}$ exerts its influence of smoothing the solution.

More generally, we can consider the solution $\mathbf{w}^\epsilon$ of the regularized system,

$$\frac{\partial \mathbf{w}^\epsilon}{\partial t} + \sum_{k=1}^{d} \frac{\partial}{\partial x_k} \mathbf{f}_k(\mathbf{w}^\epsilon) = \mathbf{R}^\epsilon(\mathbf{w}^\epsilon), \quad \epsilon > 0. \tag{1.19}$$

Here $\mathbf{R}^\epsilon$ is a regularizing term that can model diffusion, viscosity, friction, etc. Near a shock wave, the viscous terms become important. In physical phenomena, shock waves manifest as smooth transitions over very small regions [77], and the viscous terms provide this smoothing.

1.1.2 Euler Equations

Euler's equations of gas dynamics were written down more than two hundred and fifty years ago, and yet to this day they still are the backbone of fluid dynamics. The article "Principes generaux du mouvement des fluides" was published in 1757 in *Mmoires de l'Academie des Sciences de Berlin*. The equations describe the flow of an inviscid fluid through space and time. The quantities that describe the motion are density, velocity and energy. For compressible fluids an equation of state must be given.

The derivation of these equations follows from the three fundamental principles of conservation. To see this let us consider a one-dimensional pipe with a given velocity $u(x,t)$. In gas dynamics compression or expansion can cause the density ρ to vary. The total mass in a section of pipe, say $[x_1, x_2]$, is given by the basic integral form of a conservation law,

$$\frac{d}{dt} \int_{x_1}^{x_2} \rho(x,t)\, dx = F_1(t) - F_2(t), \tag{1.20}$$

where $F_i(t)$ is the flux at the endpoint x_i, $i = 1, 2$. So, the total mass in a section of the pipe can only change if there is a difference in the fluxes at the endpoints. The flux of density at (x,t) is given by $\rho(x,t) \cdot u(x,t)$. So the conservation law for the density ρ becomes

$$\rho_t + (\rho u)_x = 0. \tag{1.21}$$

This is known as **conservation of mass**. Now we need a second equation for velocity. While velocity is not conserved, momentum is conserved. The density of momentum ρu can only change due to the flux of momentum at the endpoints. Now, momentum flux is made up of two components: Momentum carried along by motion, i.e., momentum $\times$ velocity $= \rho u^2$, and microscopic flux due to pressure, p.

So the momentum flux is $\rho u^2 + p$, and the **conservation of momentum** is thus given by

$$(\rho u)_t + (\rho u^2 + p)_x = 0. \tag{1.22}$$

We now have a new unknown, pressure $p(x,t)$. Pressure is not a conserved quantity, so we introduce the density of energy, $E(x,t)$. We use an equation of state to determine the pressure in terms of mass, momentum, and energy, i.e., $p = p(\rho, u, E)$. Similar to above, there is a contribution to the flux of energy by the motion of the flow, Eu. Also, the microscopic momentum flux leads to a flux in kinetic energy, pu. The **conservation of energy** is given by

$$E_t + ((E+p)u)_x = 0. \tag{1.23}$$

These three equations give us the system of one-dimensional Euler equations,

$$\rho_t + (\rho u)_x = 0, \tag{1.24}$$

$$(\rho u)_t + (\rho u^2 + p)_x = 0, \tag{1.25}$$

$$E_t + ((E+p)u)_x = 0. \tag{1.26}$$

The system is completed by specifying an equation of state. We are interested in compressible fluids, where an equation of state relating pressure to density, velocity and energy must be appended. The multi-dimensional formula for an ideal polytropic gas is given by

$$E = \frac{p}{\gamma - 1} + \frac{\rho}{2} ||\mathbf{u}||^2. \tag{1.27}$$

γ is the adiabatic gas constant. There are many resources available on equations of state and more generally, thermodynamics (see, e.g., [12, 30, 102]).

The Euler equations in multi-dimensions are given by

$$\frac{\partial \rho}{\partial t} + \nabla \cdot (\rho \mathbf{u}) = 0, \tag{1.28}$$

$$\frac{\partial (\rho \mathbf{u})}{\partial t} + \nabla \cdot (\mathbf{u} \otimes (\rho \mathbf{u})) + \nabla p = 0, \tag{1.29}$$

$$\frac{\partial E}{\partial t} + \nabla \cdot ((E+p)\mathbf{u}) = 0. \tag{1.30}$$

Here we have $\mathbf{u}$ is the velocity vector. For example, in three dimensions $\mathbf{u} = (u, v, w)^T$. The symbol $\otimes$ is called the dyadic product of two vectors having the same dimension. The product may be represented as a matrix, e.g. in three dimensions we get the following.

$$\mathbf{x} \otimes \mathbf{y} = \begin{pmatrix} x_1 y_1 & x_1 y_2 & x_1 y_3 \\ x_2 y_1 & x_2 y_2 & x_2 y_3 \\ x_3 y_1 & x_3 y_2 & x_3 y_3 \end{pmatrix}$$

It can be shown that the Euler equations are hyperbolic. Indeed, solutions of the Euler

equations are expected to have shocks and/or rarefaction waves. The eigenvalues of the Jacobian of the flux functions, considered here in the multi-dimensional sense described earlier, give the wave speeds. The conservative variables in the solution vector $\mathbf{w}$ are density ρ, momentum $\rho\mathbf{u}$, and energy E. In one-dimension, the solution vector looks like $\mathbf{w} = (\rho, \rho u, E)^T$. Then the flux for the one-dimensional Euler equations is given by

$$\mathbf{f}(\mathbf{w}) = \begin{pmatrix} \rho u \\ \rho u^2 + p \\ (E+p)u \end{pmatrix} \tag{1.31}$$

Note that the equation of state provide us with a formula for pressure in terms of the solution vector. The Jacobian for our one-dimensional example is given by the following matrix.

$$\mathbf{f}'(\mathbf{w}) = \begin{pmatrix} 0 & 1 & 0 \\ \frac{1}{2}u^2(\gamma-3) & u(3-\gamma) & \gamma-1 \\ \frac{1}{2}(\gamma-1)u^3 - uH & H-(\gamma-1)u^2 & u\gamma \end{pmatrix}$$

Here we use the formula for enthalpy $H = (E+p)/\rho$ to simplify calculations. The eigenvalues of this matrix are given by the fluid velocity and the speed of sound in the fluid added and subtracted from the fluid velocity. For the one-dimensional problem we have $(\lambda_1, \lambda_2, \lambda_3) = (u-c, u, u+c)$, where the speed of sound is given by $c = \sqrt{(\gamma p)/\rho}$. For a more detailed analysis of the eigenvalues of the Euler flux Jacobian, see Appendix A.1.

1.1.3 Navier-Stokes Equations

The Navier-Stokes equations are a mathematical model that describes the way viscous fluids flow and are named after Claude-Louis Navier and George Gabriel Stokes. The equations are a continuation of the Euler equations and are derived from the same conservation laws with the inclusion of the physical effects of viscosity [114]. While the ideas of viscosity, pressure, and capillary action were studied heuristically by early philosophers and scientists, such as Leonardo da Vinci, the development of Newtonian mechanics saw these concepts begin to be written down in mathematical formulation. Navier first discovered the correct equations of motion for viscous fluids through a heuristic understanding of the effects of viscosity on the fluid flow. In 1845 Stokes formulated the equations in the context of fluid dynamics. The equations aim to reproduce the fluid flow given some initial perturbation to the velocity, density and energy of the fluid.

In particular, we will be working with the Navier-Stokes with heat conduction. In this formulation, the effects of viscosity and heat conduction are added to the Euler equations. The

one-dimensional version (see [35]) is given as

$$\frac{\partial \rho}{\partial t} + \frac{\partial (\rho u)}{\partial x} = 0, \tag{1.32}$$

$$\frac{\partial (\rho u)}{\partial t} + \frac{\partial (\rho u^2)}{\partial x} + \frac{\partial p}{\partial x} = \frac{\partial \Pi}{\partial x}, \tag{1.33}$$

$$\frac{\partial E}{\partial t} + \frac{\partial ((E+p)u)}{\partial x} + \frac{\partial q}{\partial x} = \frac{\partial \Pi u}{\partial x}. \tag{1.34}$$

The effects of viscosity, Π, are given by

$$\Pi = \left(\frac{4}{3}\eta + \eta \left(\frac{5}{3} - \gamma \right) B \right) \frac{\partial u}{\partial x}. \tag{1.35}$$

The coefficient B is related to temperature and intermolecular interaction. The dynamic viscosity η and the adiabatic index γ are also used to calculate the viscous stress tensor.

The thermal conductivity component, or heat flux, q is proportional to the gradient of temperature and is given by

$$q = -\kappa \frac{\partial T}{\partial x}, \tag{1.36}$$

where κ is the thermal conductivity. Temperature is calculated using the ideal gas law, see equation (2.18). In order to close the system of equations (1.32)-(1.34) we use the equation of state given by

$$E = \frac{\rho u^2}{2} + p(\gamma - 1). \tag{1.37}$$

In two dimensions, the NS equations read like this:

$$\frac{\partial \rho}{\partial t} + \frac{\partial (\rho u)}{\partial x} + \frac{\partial (\rho v)}{\partial y} = 0, \tag{1.38}$$

$$\frac{\partial (\rho u)}{\partial t} + \frac{\partial (\rho u^2)}{\partial x} + \frac{\partial (\rho v u)}{\partial y} + \frac{\partial p}{\partial x} = \frac{\partial \Pi^{(xx)}}{\partial x} + \frac{\partial \Pi^{(yx)}}{\partial y}, \tag{1.39}$$

$$\frac{\partial (\rho v)}{\partial t} + \frac{\partial (\rho u v)}{\partial x} + \frac{\partial (\rho v^2)}{\partial y} + \frac{\partial p}{\partial y} = \frac{\partial \Pi^{(xy)}}{\partial x} + \frac{\partial \Pi^{(yy)}}{\partial y}, \tag{1.40}$$

$$\begin{aligned} \frac{\partial E}{\partial t} + \frac{\partial (u(E+p))}{\partial x} + \frac{\partial (v(E+p))}{\partial y} + \frac{\partial q^{(x)}}{\partial x} + \frac{\partial q^{(y)}}{\partial y} &= \frac{\partial}{\partial x}\left(\Pi^{(xx)} u + \Pi^{(xy)} v \right) \\ &\quad + \frac{\partial}{\partial y}\left(\Pi^{(yx)} u + \Pi^{(yy)} v \right), \end{aligned} \tag{1.41}$$

where the viscous stress tensor is given by

$$\Pi^{(xx)} = \eta \left(2\frac{\partial u}{\partial x} - \left[\frac{2}{3} - \frac{\zeta}{\eta} \right] \text{div } \vec{u} \right), \tag{1.42}$$

$$\Pi^{(xy)} = \eta \left(\frac{\partial v}{\partial x} + \frac{\partial u}{\partial y} \right), \tag{1.43}$$

$$\Pi^{(yx)} = \eta \left(\frac{\partial u}{\partial y} + \frac{\partial v}{\partial x} \right), \tag{1.44}$$

$$\Pi^{(yy)} = \eta \left(2\frac{\partial v}{\partial y} - \left[\frac{2}{3} - \frac{\zeta}{\eta} \right] \text{div } \vec{u} \right). \tag{1.45}$$

The parameter ζ in (1.45)is the bulk viscosity. Finally, the heat flux in equation (1.41) is given by

$$q^{(x)} = -\kappa \frac{\partial T}{\partial x}, \tag{1.46}$$

$$q^{(y)} = -\kappa \frac{\partial T}{\partial y}. \tag{1.47}$$

Again, we close the system of equations (1.38)-(1.41) with equation of state given by

$$E = \rho(u^2 + v^2)/2 + p(\gamma - 1). \tag{1.48}$$

It is noted that the equation of state provides a description of the thermodynamics of the system and is an approximate statement on the nature of the medium [114].

1.2 Numerical Methods

Since exact answers to practical mathematical problems are usually unobtainable, numerical approximations provide a tool for analyzing these problems. Numerical methods have been used for centuries, even millennium. Ancient tablets provide numerical algorithms for approximating square roots. Some of the most important algorithms, which still enjoy widespread popularity and use, are named after some of the most prolific mathematicians from the eighteenth century. For example, we have Newton's method, Euler's method, and Lagrange interpolation. The proliferation of computational methods has been to mathematical modeling what the microscope and telescope were to biology and astronomy.

The numerical schemes employed to solve PDEs and, in particular, conservation laws include finite volume methods [5, 4, 28, 47, 19, 8], finite difference methods or WENO schemes [21, 78, 79] and finite element methods [10]. Of particular interest are upwind schemes [16, 20, 33]. There are many examples of high resolution methods [17, 60], positivity preserving and other

types of non-oscillatory schemes [2, 20], and adaptive mesh schemes [15, 49].

1.2.1 Finite Volume Method

Finite Volume (FV) methods are the most popular methods for systems of conservation laws [77] thanks to their ability to capture nonsmooth (discontinuous) solutions in an accurate and non-oscillatory manner. In these methods, the solution is realized in terms of cell averages which are evolved according to the integral formulation of the problem.

For simplicity, we present here a one-dimensional version,

$$\frac{\partial \mathbf{w}(x,t)}{\partial t} + \frac{\partial \mathbf{f}(\mathbf{w}(x,t))}{\partial x} = 0. \tag{1.49}$$

Here, $\mathbf{w}$ is the vector of quantities being measured, $\mathbf{f}$ is the flux function, and x and t are the spatial and time variables, repsectively. The conservation law, (1.49), is represented in integral form as

$$\frac{d}{dt}\int_a^b \mathbf{w}(x,t)dt = \mathbf{f}(\mathbf{w}(a,t)) - \mathbf{f}(\mathbf{w}(b,t)). \tag{1.50}$$

In order to do develop a FV approximation to (1.49), we create a grid over the spatial domain by letting $x_j = j\Delta x,\ x_{j\pm\frac{1}{2}} = x_j \pm \frac{\Delta x}{2},\ j = 1, \cdots N$, where N indicates the size of the grid. We denote the j^{th} grid cell by

$$C_j = (x_{j-\frac{1}{2}}, x_{j+\frac{1}{2}}). \tag{1.51}$$

We then denote the approximate cell average of $\mathbf{w}(x,t)$ over the grid cell C_i at time t^n as $\bar{\mathbf{w}}_j^n$, given by the following formula.

$$\bar{\mathbf{w}}_j^n \approx \frac{1}{\Delta x}\int_{x_{j-\frac{1}{2}}}^{x_{j+\frac{1}{2}}} \mathbf{w}(x,t^n)dx. \tag{1.52}$$

Note that, if $\mathbf{w}(x,t)$ is smooth, the midpoint rule gives a second-order approximation to the integral in (1.52). We now would like to derive a formula for the evolution in time of this cell average. If we integrate (1.50) in time from t^n to t^{n+1}, and divide through by Δx, we get the following equation.

$$\frac{1}{\Delta x}\int_{x_{j-\frac{1}{2}}}^{x_{j+\frac{1}{2}}} \mathbf{w}(x,t^{n+1})dx = \frac{1}{\Delta x}\int_{x_{j-\frac{1}{2}}}^{x_{j+\frac{1}{2}}} \mathbf{w}(x,t^n)dx - \frac{1}{\Delta x}\left[\int_{t^n}^{t^{n+1}} \mathbf{f}(\mathbf{w}(x_{j+\frac{1}{2}},t))dt - \int_{t^n}^{t^{n+1}} \mathbf{f}(\mathbf{w}(x_{j-\frac{1}{2}},t))dt\right] \tag{1.53}$$

This formula gives us the exact evolution in time of the cell averages. Note that the spatial integrals in (1.53) are the cell averages $\bar{\mathbf{w}}_j^{n+1}$ and $\bar{\mathbf{w}}_j^n$. Note also that we can not evaluate the time integrals on the right-hand side of (1.53) since these functions are in general changing along the grid interfaces over time. We can rewrite (1.53) using the cell averages as

$$\bar{\mathbf{w}}_j^{n+1} = \bar{\mathbf{w}}_j^n - \frac{1}{\Delta x}\left[\int_{t^n}^{t^{n+1}} \mathbf{f}(\mathbf{w}(x_{j+\frac{1}{2}}, t))dt - \int_{t^n}^{t^{n+1}} \mathbf{f}(\mathbf{w}(x_{j-\frac{1}{2}}, t))dt\right]. \tag{1.54}$$

The approximation of the flux functions here becomes the main challenge and the choice of how to approximate the integrals on the right-hand side of (1.54) determines the class of finite volume scheme.

In order to further discuss the nuances involved in approximating flux functions, let us denote the approximation of the average of the time integral of the flux functions, called the numerical flux, as $\mathbf{F}^n_{j\pm\frac{1}{2}}$. I.e.,

$$\mathbf{F}^n_{j+\frac{1}{2}} \approx \frac{1}{\Delta t}\int_{t^n}^{t^{n+1}} \mathbf{f}(\mathbf{w}(x_{j+\frac{1}{2}}, t))dt. \tag{1.55}$$

We can then represent equation (1.53) in terms of these approximate flux functions and the cell averages. This is given below in equation (1.56),

$$\bar{\mathbf{w}}_j^{n+1} = \bar{\mathbf{w}}_j^n - \frac{\Delta t}{\Delta x}\left(\mathbf{F}^n_{j+\frac{1}{2}} - \mathbf{F}^n_{j-\frac{1}{2}}\right). \tag{1.56}$$

There are several factors that go into the determination of an appropriate approximation of the flux. In particular, we would like to choose the numerical flux so as to obtain a convergent numerical method. The notion of convergence in numerical methods involves two conditions. The method should be consistent and stable. Consistency denotes the ability of the numerical method to accurately approximate the PDE. Stability demands that small changes in initial data result in small changes in the numerical approximation. To further discuss these components in detail, let us introduce notation to represent the numerical flux in terms of the values by which it will be calculated. For convenience, we introduce the notation $\widehat{\mathbf{F}}$, where

$$\widehat{\mathbf{F}}_{j+\frac{1}{2}}(\bar{\mathbf{w}}_j^n, \bar{\mathbf{w}}_{j+1}^n) = \mathbf{F}^n_{j+\frac{1}{2}}. \tag{1.57}$$

This notation makes it clear that the numerical flux depends only on the cell averages on either side of the flux boundary. If we rewrite (1.56) using this notation, we get an alternative representation of this cell average update formula, given below in (1.58). Note that this method

has a three-point stencil,

$$\bar{\mathbf{w}}_j^{n+1} = \bar{\mathbf{w}}_j^n - \frac{\Delta t}{\Delta x}\left(\widehat{\mathbf{F}}_{j+\frac{1}{2}}(\bar{\mathbf{w}}_j, \bar{\mathbf{w}}_{j+1}) - \widehat{\mathbf{F}}_{j-\frac{1}{2}}(\bar{\mathbf{w}}_{j-1}, \bar{\mathbf{w}}_j)\right). \tag{1.58}$$

In determining if a method is consistent, we need to check that it approximates the integral given in (1.55). Note that if the function $\mathbf{w}(x,t) = \mathbf{c}$ is a constant vector, then the integral is equal to $\mathbf{f}(\mathbf{c})$. Thus, we can check for consistency by determining if it satisfies the following condition,

$$\widehat{\mathbf{F}}_{j+\frac{1}{2}}(\mathbf{c}, \mathbf{c}) = \mathbf{f}(\mathbf{c}). \tag{1.59}$$

Also, we expect the numerical flux to satisfy a Lipshitz continuity condition. E.g., for some constant L,

$$|\widehat{\mathbf{F}}_{j+\frac{1}{2}}(\bar{\mathbf{w}}_j, \bar{\mathbf{w}}_{j+1}) - \mathbf{f}(\mathbf{c})| \leq \mathrm{L}\, \max\left(|\bar{\mathbf{w}}_j - \mathbf{c}|, |\bar{\mathbf{w}}_{j+1} - \mathbf{c}|\right). \tag{1.60}$$

Recall that, for hyperbolic problems, information propagates along the characteristics at finite speed. Thus, the domain of dependence for a fixed point (X,T) is a bounded set. The bounds of this set are determined by the eigenvalues of the flux of the Jacobian. In order for the numerical method to be stable, it must necessarily satisfy the Courant-Friederichs-Lewy (CFL) condition. The CFL condition states that the numerical domain of dependence must contain the actual domain of dependence of the PDE. This is obviously necessary, since if there exists information contributing to the evaluation of a quantity that is not being considered by the numerical method, then a change in the initial data outside the numerical domain of dependence would not affect the approximation, while the true solution would change.

An easy way to see this is by studying the linear scalar advection problem given below,

$$u_t + a u_x = 0, \tag{1.61}$$

where a is the advection speed. The CFL condition for the advection equation is given by

$$\nu = \left|\frac{a\Delta t}{\Delta x}\right| \leq 1, \tag{1.62}$$

where a is the advection speed and ν is called the Courant number. Figure 1.1 conveniently illustrates this restriction.

The domain of dependence for the fixed point (X,T) is the single point $x - at$. Thus, the numerical domain of dependence must contain this point, and so we need the distance traveled at speed a over the time step Δt to be less than Δx. For hyperbolic problems, this speed is

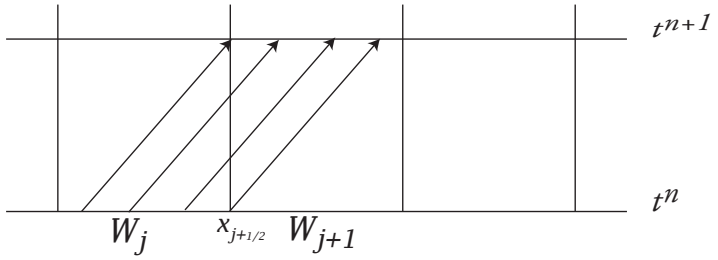

Figure 1.1: Domain of dependence for advection

given by the eigenvalue of the flux Jacobian. For example, if we have a system of N hyperbolic equations, the Courant number is determined by the maximum wave speed. Letting λ_k for $k = 1, \ldots, N$ represent the eigenvalues of the Jacobian, we get

$$\nu = \frac{\Delta t}{\Delta x} \max_k |\lambda_k| \,. \tag{1.63}$$

It is restated that the CFL condition is only a necessary condition for stability.

Godunov-type Schemes

The core class of finite volume methods are Godunov-type schemes, named after Sergei Godunov the Russian mathematician credited for developing the algorithm. In [42], the data available at time t^n is reconstructed as a piecewise constant over the grid cells. The update in time is accomplished by solving exactly the resulting Riemann problem at each cell interface. Originally, Godunov developed the algorithm to solve the nonlinear Euler equations of gas dynamics. However, its effectiveness has fostered the development of an entire class of methods which have transformed computational fluid dynamics. In general, the algorithm involves three distinct steps:

Godunov's Method

1. Reconstruct a piecewise polynomial function using the cell averages available at time t^n.
2. Evolve the hyperbolic problem with this initial data to obtain the updated piecewise polynomial approximation.

3. Average (project) this new approximation over the grid cells to obtain the updated cell averages.

As mentioned above, a piecewise polynomial function is reconstructed over the grid cells. In fact, the order of the numerical scheme is tied to the order of this piecewise reconstruction. In general, the piecewise reconstruction is given as

$$\mathbf{w}(x, t^n) \approx \mathbf{p}_j^n(x), \quad \text{for } x \in (x_{j-\frac{1}{2}}, x_{j+\frac{1}{2}}). \tag{1.64}$$

It is noted that the polynomial pieces are typically discontinuous at the cell interfaces $x = x_{j\pm\frac{1}{2}}$. The stability of the finite volume method is, in general, guaranteed when (1.64) is non-oscillatory, which is accomplished by the use of slope limiters. A library of non-oscillatory reconstructions is available, see e.g., [1, 31, 41, 48, 50, 55, 62, 68, 77, 78, 79, 82, 86, 87, 88, 95, 105, 106, 112, 117]. A more detailed description of the linear piecewise reconstruction is provided in the subsequent section presenting the semidiscrete central upwind scheme.

The piecewise reconstruction allows for an exact evolution of the the solution, which is comprised of a finite set of waves traveling at constant speeds. However, depending on the configuration of the grid cells, Godunov's method requires the solutions to the Riemann problems that arise at the grid interfaces, and so Riemann solvers are needed at each time step. There is considerable attention given to solving Riemann problems, see, e.g., [13, 14, 26, 27, 75, 107, 108]. It is noted that the solutions to Riemann problems are not always available, limiting the types of problems to which the method may be applied. For systems, this can be even more complicated by waves traveling in different directions.

Now we turn our attention to the task of defining the numerical flux functions in terms of the cell averages available on either side of the flux interface. In particular, we will consider two ways to configure the control volumes over which the flux function is integrated. These are described in the figure below. As we will see, the Godunov-type schemes are divided into upwind and central schemes.

Upwind Schemes

Upwind methods attempt to use information about the behavior of the solution in determining the numerical flux function. Recall, solutions to hyperbolic problems are waves that propagate with a finite speed. Upwind methods anticipate the arrival of information along the characteristics on which they travel. Thus, these methods are able to produce results with less diffusion.

Consider again the one-dimensional system (1.49). In upwind schemes, the cell averages at time $t = t^{n+1}$ are obtained by approximating the integrals on the right-hand side of (1.54). Since the piecewise polynomial reconstruction is, in general, discontinuous at the cell interfaces,

$x = x_{j\pm\frac{1}{2}}$, upwind schemes depend on the approximate solution of the Riemann problems that arise there. See, e.g., [14, 19, 31, 41, 42, 62, 77, 114]. As mentioned above, these are generally expensive and complicated (or impossible) to approximate.

Central Schemes

Central schemes have the advantage of being readily applicable to a wide range of problems. They have the distinct and important advantage of simplicity, since they do not require any information about the solution. A drawback of these schemes is that they may exhibit excessive smoothing or spurious oscillations.

Finite volume schemes based on the staggered control volumes shown in Figure 1.2 lead to centered schemes. There are many examples of staggered central schemes. See, e.g.,[7, 8, 17, 56, 78, 79, 81, 88, 85, 95, 96, 97, 98, 100]. These schemes offer a much simpler, Riemann-solver-free approach. The solution is evolved in terms of cell averages over the staggered grid:

$$\bar{\mathbf{w}}_{j+\frac{1}{2}}^{n+1} = \frac{1}{2\Delta x}\left(\int_{x_{j-\frac{1}{2}}}^{x_{j+\frac{1}{2}}} \mathbf{p}_j^n(x)dx + \int_{x_{j-\frac{1}{2}}}^{x_{j+\frac{1}{2}}} \mathbf{p}_{j+1}^n(x)dx\right) - \frac{1}{\Delta x}\left[\int_{t^n}^{t^{n+1}} \mathbf{f}(\mathbf{w}(x_{j+1},t))dt - \int_{t^n}^{t^{n+1}} \mathbf{f}(\mathbf{w}(x_j,t))dt\right]. \tag{1.65}$$

As seen in Figure 1.2, when an appropriate CFL condition is satisfied, the solution $\mathbf{w}(x,t)$ remains smooth along the lines $x = x_{j\pm\frac{1}{2}}$ for $t \in [t^n, t^{n+1}]$ and so the integrals on the right-hand side of (1.65) can be easily evaluated.

1.2.2 Semidiscrete Central Upwind Scheme

The semidiscrete central upwind (CU) scheme, developed in [64, 65, 66, 67, 68, 69, 70, 71], combines the best of both central and upwind schemes. In particular, it combines the simplicity and universality of central schemes with the higher accuracy and lower dissipation of central schemes.

The CU scheme has its roots in the Lax-Friedrichs (LxF) method, ("...the stable all purpose benchmark for approximate solutions of nonlinear systems"[113]), and the staggered central scheme in [95]. The main idea is to use more precise information about the local speeds of propagation to more accurately estimate the width of the Riemann fans. This gives the scheme its *upwind* nature. The simplicity of *central* schemes is retained because it integrates over the Riemann fan without utilizing a Riemann problem solver or characteristic decompositon. The result is better resolution of shocks as well as a method that admits a semi-discrete formulation, an important result that allows for coupling with appropriate ODE solvers. It is emphasized that these local speeds are the only additional information required to modify the staggered

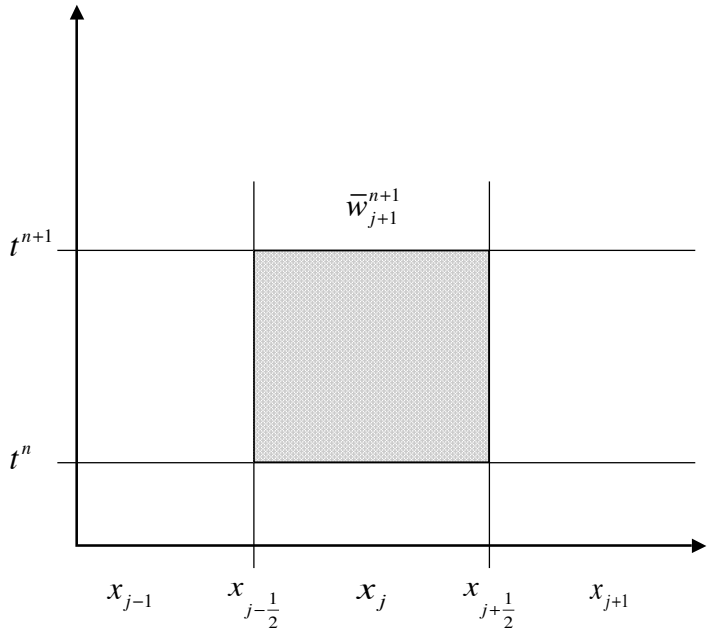

(a) Upwind control volume

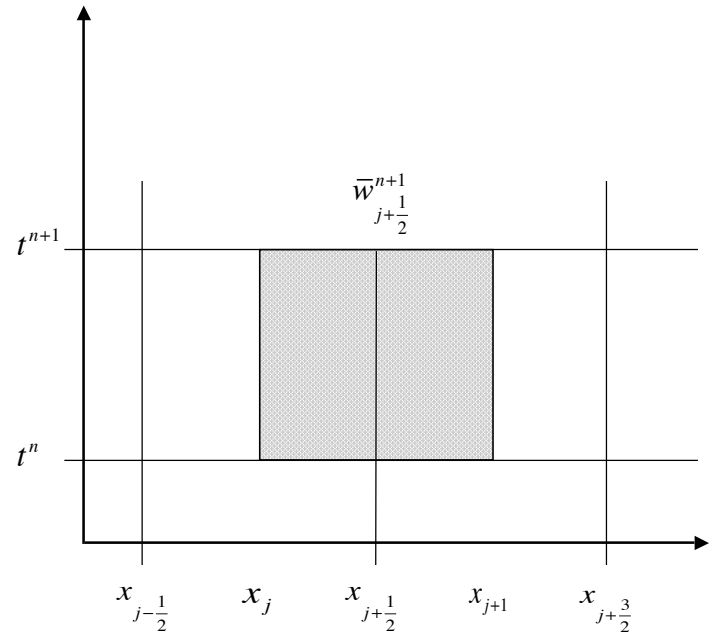

(b) Central (staggered) control volume

Figure 1.2: Control Volumes

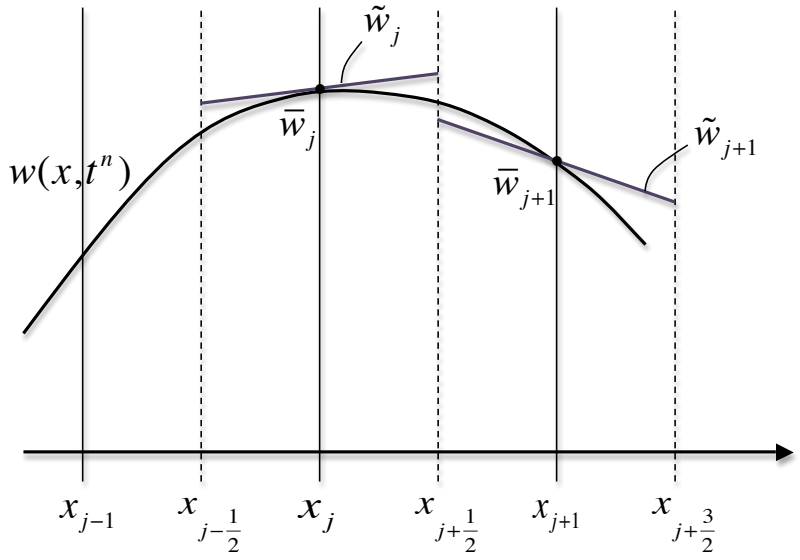

Figure 1.3: Interpolant Schematic

scheme in [95].

Semidiscrete scheme for 1-D conservation laws

In this section, we describe a derivation of the one-dimensional CU scheme for conservation laws, which was originally developed in [70, 66, 64]. We consider uniform spatial grids and use the notation: $x_j = j\Delta x,\ x_{j\pm\frac{1}{2}} = x_j \pm \frac{\Delta x}{2},\ t^n = n\Delta t,\ \mathbf{w}_j^n = \mathbf{w}(x_j, t^n)$.

The integral formulation of equation (1.49) is given as

$$\frac{d}{dt}\int_{x_{j-\frac{1}{2}}}^{x_{j+\frac{1}{2}}} \mathbf{w}(x,t)dx = \mathbf{f}(\mathbf{w}(x_{j-\frac{1}{2}},t)) - \mathbf{f}(\mathbf{w}(x_{j+\frac{1}{2}},t)). \tag{1.66}$$

As previously mentioned, we use the cell averages to interpolate a piecewise polynomial reconstruction of degree $r-1$, where r is the order of the scheme. For example, the second-order scheme we are establishing here uses a piecewise linear polynomial. As such, we consider the problem with the piecewise linear initial condition,

$$\tilde{\mathbf{w}}(x,t^n) = \mathbf{p}_j^n(x) := \sum_j \left[\bar{\mathbf{w}}j^n + (\mathbf{w}_x)_j^n(x - x_j)\right]\mathbf{1}_{[x_{j-\frac{1}{2}},x_{j+\frac{1}{2}}]}, \quad x_{j-\frac{1}{2}} < x < x_{j+\frac{1}{2}}, \tag{1.67}$$

obtained from the cell averages at the previous step. Note that (1.67) is continuous except for possible discontinuities at the interface points, $x_{j\pm\frac{1}{2}}$. The spatial derivative in (1.67) may be approximated by the use of an appropriate slope limiter in order to suppress spurious oscillations or excessive smearing. A library of such limiters is available (see, e.g., [41, 62, 77, 83, 95, 112, 117]), and one can compute the numerical derivatives using one's favorite limiter. In our numerical experiments, we have used the generalized minmod reconstruction [83, 95, 117] given by

$$(\mathbf{w}_x)_j^n \approx \mathbf{s}_j^n = \text{minmod}\left(\theta\frac{\bar{\mathbf{w}}(x+\Delta x)-\bar{\mathbf{w}}(x)}{\Delta x}, \frac{\bar{\mathbf{w}}(x+\Delta x)-\bar{\mathbf{w}}(x-\Delta x)}{2\Delta x}, \theta\frac{\bar{\mathbf{w}}(x)-\bar{\mathbf{w}}(x-\Delta x)}{\Delta x}\right). \tag{1.68}$$

The parameter $\theta \in [1,2]$ is chosen in an optimal manner as to balance dissipation and oscillation, where $\theta = 2$ corresponds to the most oscillation. The multivariable minmod function is defined by

$$\text{minmod}(x_1, x_2, \ldots) = \begin{cases} \min_j\{x_j\}, & \text{if } x_j > 0 \ \forall j, \\ \max_j\{x_j\}, & \text{if } x_j < 0 \ \forall j, \\ 0, & \text{otherwise.} \end{cases} \tag{1.69}$$

The piecewise reconstruction $\tilde{\mathbf{w}}(x, t^n)$ is then evolved exactly according to (1.54).

Recall, that the reconstruction (1.67) may contain discontinuities at the interface points $x_{j\pm\frac{1}{2}}$, see Figure 1.4. These discontinuities propagate with speeds which may be estimated by the eigenvalues of the Jacobian of the flux. These right- and -left-sided local speeds are given in equations (1.70) and (1.71).

$$a^+_{j+\frac{1}{2}} = \max_{\omega\in C(\mathbf{w}^-_{j+\frac{1}{2}}, \mathbf{w}^+_{j+\frac{1}{2}})} \left\{\lambda_N(\frac{\delta \mathbf{f}}{\delta \mathbf{w}}(\omega)), 0\right\}, \tag{1.70}$$

$$a^-_{j+\frac{1}{2}} = \min_{\omega\in C(\mathbf{w}^-_{j+\frac{1}{2}}, \mathbf{w}^+_{j+\frac{1}{2}})} \left\{\lambda_1(\frac{\delta \mathbf{f}}{\delta \mathbf{w}}(\omega)), 0\right\}. \tag{1.71}$$

Here, $\lambda_1 < \cdots < \lambda_N$ are the eigenvalues of the Jacobian $\frac{\delta \mathbf{f}}{\delta \mathbf{w}}$. The curve, $C(\mathbf{w}^-_{j+\frac{1}{2}}, \mathbf{w}^+_{j+\frac{1}{2}})$ is a curve in phase space that connects the point values, $\mathbf{w}^\pm_{j+\frac{1}{2}}$, which are the the values of the piecewise polynomial, (1.67), evaluated on either side of the grid interface points. See Figure 1.4. These point values are given by

$$\mathbf{w}^+_{j+\frac{1}{2}} = \mathbf{p}_{j+1}(x_{j+\frac{1}{2}}) \text{ and } \mathbf{w}^-_{j+\frac{1}{2}} = \mathbf{p}_j(x_{j+\frac{1}{2}}). \tag{1.72}$$

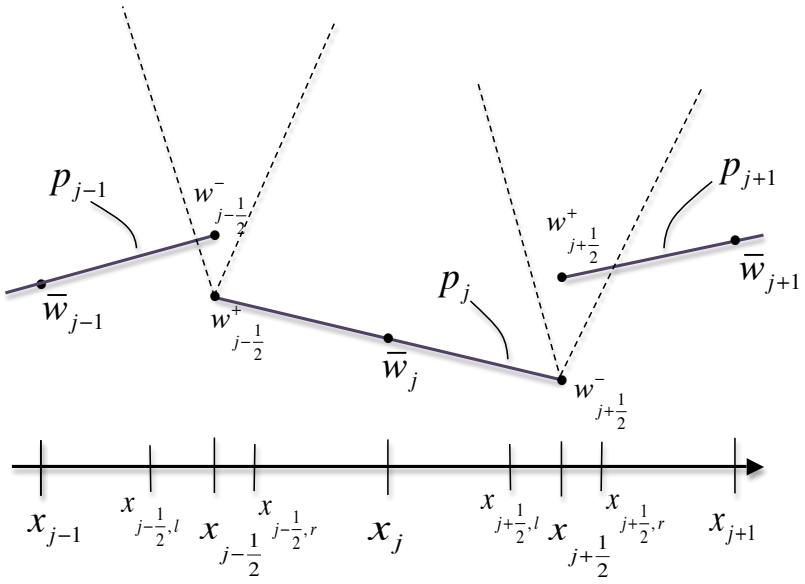

Figure 1.4: Semi-discrete Schematic

The local speeds, $a^{\pm}_{j+\frac{1}{2}}$, are used to narrow the control volumes over which Riemann fans are integrated. In this way, the non-smooth parts of the computed solution are averaged over smaller cells. The development of the CU scheme allows for the separation of the spatial domain into regions which are either smooth or non-smooth. This allows for the avoidance of costly Riemann solvers, thus retaining the simplicity of central schemes.

Thanks to the finite speed of propagation, the smooth and non-smooth regions are separated by points $x^n_{j+\frac{1}{2},l} := x_{j+\frac{1}{2}} + \Delta t a^-_{j+\frac{1}{2}}$ and $x^n_{j+\frac{1}{2},r} := x_{j+\frac{1}{2}} + \Delta t a^+_{j+\frac{1}{2}}$. In particular, the smooth regions are contained in the intervals $[x^n_{j-\frac{1}{2},r}, x^n_{j+\frac{1}{2},l}]$ and the non-smooth regions are contained in the intervals $[x^n_{j+\frac{1}{2},l}, x^n_{j+\frac{1}{2},r}]$.

First, according to the development of the CU scheme, let us consider integration over the smooth region around x_j which does not contain the Riemann fans. We would like to evolve the piecewise polynomial (1.67) over the interval surrounding x_j to obtain the new average over this interval. Let this average be denoted by $\bar{\mathbf{v}}^{n+1}_j$, where

$$\bar{\mathbf{v}}^{n+1}_j = \frac{1}{x^n_{j+\frac{1}{2},l} - x^n_{j-\frac{1}{2},r}} \left[\int_{x^n_{j-\frac{1}{2},r}}^{x^n_{j+\frac{1}{2},l}} \mathbf{p}^n_j(x)\, dx - \int_{t^n}^{t^{n+1}} \Big(\mathbf{f}(\mathbf{w}(x^n_{j+\frac{1}{2},l}, t)) - \mathbf{f}(\mathbf{w}(x^n_{j-\frac{1}{2},r}, t)) \Big)\, dt \right]. \tag{1.73}$$

To obtain $\bar{\mathbf{v}}^{n+1}_{j+\frac{1}{2}}$, the integration is divided between the smooth and non-smooth part of the domain, $[x^n_{j+\frac{1}{2},l}, x^n_{j+\frac{1}{2},r}]$. The piecewise polynomial $\mathbf{p}^n_j(x)$ is integrated over the interval $[x^n_{j+\frac{1}{2},l}, x^n_{j+\frac{1}{2}}]$, and $\mathbf{p}^n_{j+1}(x)$ is integrated over the interval $[x^n_{j+\frac{1}{2}}, x^n_{j+\frac{1}{2},r}]$. Thus, the formula (1.74) for $\bar{\mathbf{v}}^{n+1}_{j+\frac{1}{2}}$ is obtained,

$$\begin{aligned} \bar{\mathbf{v}}^{n+1}_{j+\frac{1}{2}} = \frac{1}{x^n_{j+\frac{1}{2},r} - x^n_{j+\frac{1}{2},l}} \Bigg[& \int_{x^n_{j+\frac{1}{2},l}}^{x^n_{j+\frac{1}{2}}} \mathbf{p}^n_j(x)\, dx + \int_{x^n_{j+\frac{1}{2}}}^{x^n_{j+\frac{1}{2},r}} \mathbf{p}^n_{j+1}(x)\, dx \\ & - \int_{t^n}^{t^{n+1}} \Big(\mathbf{f}(\mathbf{w}(x^n_{j+\frac{1}{2},r}, t)) - \mathbf{f}(\mathbf{w}(x^n_{j+\frac{1}{2},l}, t)) \Big)\, dt \Bigg], \end{aligned} \tag{1.74}$$

and the solution is realized at time t^{n+1} in terms of the approximate cell averages $\bar{\mathbf{v}}^{n+1}_j$ and $\bar{\mathbf{v}}^{n+1}_{j+\frac{1}{2}}$. The cells in question are non-uniformally distributed over the the domain. As well, there are twice as many cells as the original number of cells. The next step in the development of the CU scheme is to project these averages back onto the uniform original grid consisting of cells $[x_{j-\frac{1}{2}}, x_{j+\frac{1}{2}}]$. To accomplish this, a conservative, non-oscillatory piecewise quadratic function is reconstructed from the cell averages $\bar{\mathbf{v}}^{n+1}_j$ and $\bar{\mathbf{v}}^{n+1}_{j+\frac{1}{2}}$. This function is denoted by $\tilde{\mathbf{v}}^{n+1}$ and

is given in (1.75).

$$\tilde{\mathbf{v}}^{n+1}(x) := \sum_j \left(\tilde{\mathbf{v}}_j^{n+1}(x) \cdot 1_{[x_{j-\frac{1}{2},r}, x_{j+\frac{1}{2},l}]} + \tilde{\mathbf{v}}_{j+\frac{1}{2}}^{n+1}(x) \cdot 1_{[x_{j+\frac{1}{2},l}, x_{j+\frac{1}{2},r}]} \right), \quad x_{j-\frac{1}{2},r} < x < x_{j+\frac{1}{2},r}. \tag{1.75}$$

In (1.75), $\tilde{\mathbf{v}}_j^{n+1}(x)$ and $\tilde{\mathbf{v}}_{j+\frac{1}{2}}^{n+1}(x)$ are the piecewise quadratic functions on the indicated intervals. Now, according to the development of the CU scheme, the updated cell averages $\bar{\mathbf{w}}_j^{n+1}$ are calculated by integrating $\tilde{\mathbf{v}}^{n+1}$ over the original grid cells, as seen below:

$$\bar{\mathbf{w}}_j^{n+1} = \frac{1}{\Delta x} \int_{x_{j-\frac{1}{2}}}^{x_{j+\frac{1}{2}}} \tilde{\mathbf{v}}^{n+1}(x) dx. \tag{1.76}$$

We now continue with the derivation of the semi-discrete second-order central scheme. In order to achieve this, equation (1.76) is used to express the time derivative $\bar{\mathbf{w}}_j(t)$, as follows:

$$\frac{d}{dt}\bar{\mathbf{w}}_j(t) = \lim_{\Delta t \to 0} \frac{\bar{\mathbf{w}}_j^{n+1}(t) - \bar{\mathbf{w}}_j^n(t)}{\Delta t} = \lim_{\Delta t \to 0} \frac{1}{\Delta t} \left[\left(\frac{1}{\Delta x} \int_{x_{j-\frac{1}{2}}}^{x_{j+\frac{1}{2}}} \tilde{\mathbf{v}}^{n+1}(x) dx \right) - \bar{\mathbf{w}}_j^n \right]. \tag{1.77}$$

We can begin to tackle the integral of $\tilde{\mathbf{v}}^{n+1}(x)$ by separating the regions of integration as follows.

$$\int_{x_{j-\frac{1}{2}}}^{x_{j+\frac{1}{2}}} \tilde{\mathbf{v}}^{n+1}(x) dx = \int_{x_{j-\frac{1}{2}}}^{x_{j-\frac{1}{2},r}} \tilde{\mathbf{v}}_{j-\frac{1}{2}}^{n+1}(x) dx + \int_{x_{j-\frac{1}{2},r}}^{x_{j+\frac{1}{2},l}} \tilde{\mathbf{v}}_j^{n+1}(x) dx + \int_{x_{j+\frac{1}{2},l}}^{x_{j+\frac{1}{2}}} \tilde{\mathbf{v}}_{j+\frac{1}{2}}^{n+1}(x) dx. \tag{1.78}$$

The first and last integrals on the right-hand side of (1.78) can be approximated by noting that the width of the Riemann fans originating at $x_{j\pm\frac{1}{2}}$ are bounded by $\Delta t(a^+_{j\pm\frac{1}{2}} - a^-_{j\pm\frac{1}{2}})$. Since we can assume the slopes of $\tilde{\mathbf{v}}_{j\pm\frac{1}{2}}^{n+1}$ are uniformly bounded independent of Δt, we get the following approximations of these integrals.

$$\int_{x_{j-\frac{1}{2}}}^{x_{j-\frac{1}{2},r}} \tilde{\mathbf{v}}_{j-\frac{1}{2}}^{n+1}(x) dx \approx \Delta t a^+_{j-\frac{1}{2}} \bar{\mathbf{v}}_{j-\frac{1}{2}}^{n+1} \tag{1.79}$$

$$\int_{x_{j+\frac{1}{2},l}}^{x_{j+\frac{1}{2}}} \tilde{\mathbf{v}}_{j+\frac{1}{2}}^{n+1}(x) dx \approx -\Delta t a^-_{j+\frac{1}{2}} \bar{\mathbf{v}}_{j+\frac{1}{2}}^{n+1} \tag{1.80}$$

Also, due to the conservative nature of the piecewise reconstruction, (1.75), we get the following formula,

$$\frac{1}{x^n_{j+\frac{1}{2},l} - x^n_{j-\frac{1}{2},r}} \int_{x_{j-\frac{1}{2},r}}^{x_{j+\frac{1}{2},l}} \tilde{\mathbf{v}}_j^{n+1}(x) dx = \bar{\mathbf{v}}_j^{n+1}. \tag{1.81}$$

Substituting equations (1.79), (1.80), and (1.81) into (1.78) gives us the following expression for the integral of $\tilde{\mathbf{v}}^{n+1}(x)$.

$$\int_{x_{j-\frac{1}{2}}}^{x_{j+\frac{1}{2}}} \tilde{\mathbf{v}}^{n+1}(x)dx = \Delta t a^{+}_{j-\frac{1}{2}} \bar{\mathbf{v}}^{n+1}_{j-\frac{1}{2}} + \left(x^{n}_{j+\frac{1}{2},l} - x^{n}_{j-\frac{1}{2},r}\right) \bar{\mathbf{v}}^{n+1}_{j} - \Delta t a^{-}_{j+\frac{1}{2}} \bar{\mathbf{v}}^{n+1}_{j+\frac{1}{2}}. \tag{1.82}$$

We can now substitute this expression into equation (1.77). This results in the following derivation for the time derivative of $\bar{\mathbf{w}}_j(t)$.

$$\frac{d}{dt}\bar{\mathbf{w}}_j(t) = \frac{a^{+}_{j-\frac{1}{2}}}{\Delta x} \lim_{\Delta t \to 0} \bar{\mathbf{v}}^{n+1}_{j-\frac{1}{2}} + \lim_{\Delta t \to 0} \frac{1}{\Delta t} \left(\left(\frac{x^{n}_{j+\frac{1}{2},l} - x^{n}_{j-\frac{1}{2},r}}{\Delta x} \right) \bar{\mathbf{v}}^{n+1}_{j} - \bar{\mathbf{w}}^{n}_{j} \right) - \frac{a^{-}_{j+\frac{1}{2}}}{\Delta x} \lim_{\Delta t \to 0} \bar{\mathbf{v}}^{n+1}_{j+\frac{1}{2}}. \tag{1.83}$$

Now, each of these limits is evaluated individually. In order to evaluate these limits, we must first recall equations (1.73) and (1.74), which provide the formulas for the cell averages over the non-uniform grid consisting of both smooth and non-smooth intervals that are involved in the limit calculations. Let us begin with the first term on the right-hand side of equation (1.83), which involves the cell average $\bar{\mathbf{v}}^{n+1}_{j-\frac{1}{2}}$ over the non-smooth interval $[x^{n}_{j-\frac{1}{2},l}, x^{n}_{j-\frac{1}{2},r}]$. Substituting the appropriate version of (1.74) into this term gives us the following configuration of the limit.

$$\begin{aligned} \lim_{\Delta t \to 0} \bar{\mathbf{v}}^{n+1}_{j-\frac{1}{2}} = \lim_{\Delta t \to 0} \Bigg(\frac{1}{x^{n}_{j-\frac{1}{2},r} - x^{n}_{j-\frac{1}{2},l}} \Bigg[& \int_{x^{n}_{j-\frac{1}{2},l}}^{x^{n}_{j-\frac{1}{2}}} \mathbf{p}^{n}_{j}(x)\, dx + \int_{x^{n}_{j-\frac{1}{2}}}^{x^{n}_{j-\frac{1}{2},r}} \mathbf{p}^{n}_{j+1}(x)\, dx \\ & - \int_{t^n}^{t^{n+1}} \left(\mathbf{f}(\mathbf{w}(x^{n}_{j-\frac{1}{2},r}, t)) - \mathbf{f}(\mathbf{w}(x^{n}_{j-\frac{1}{2},l}, t)) \right) dt \Bigg] \Bigg). \end{aligned} \tag{1.84}$$

Since we are considering the limit as $\Delta t \to 0$, we have that $x^{n}_{j-\frac{1}{2},l} \to x^{n}_{j-\frac{1}{2}}$, by definition of $x^{n}_{j-\frac{1}{2},l}$, and similarly $x^{n}_{j-\frac{1}{2},r} \to x^{n}_{j-\frac{1}{2}}$. Thus, $\mathbf{p}^{n}_{j}(x)$ and $\mathbf{p}^{n+1}_{j}(x)$ approach their values at the grid point $x_{j-\frac{1}{2}}$, namely and respectively, the point values $\mathbf{w}^{-}_{j-\frac{1}{2}}$ and $\mathbf{w}^{+}_{j-\frac{1}{2}}$. Therefore, the spatial integrals may be evaluated as the product of this point value and the length of the integration interval. Note, for example, that $x^{n}_{j-\frac{1}{2}} - x^{n}_{j-\frac{1}{2},l} = -\Delta t a^{-}_{j-\frac{1}{2}}$. Similarly, the flux functions in the temporal integrals may also be evaluated at these point values. Thus, we get the following expression for $\bar{\mathbf{v}}^{n+1}_{j-\frac{1}{2}}$.

$$\begin{aligned} \bar{\mathbf{v}}^{n+1}_{j-\frac{1}{2}} = \frac{1}{\Delta t (a^{+}_{j-\frac{1}{2}} - a^{-}_{j-\frac{1}{2}})} \Big[& -\Delta t a^{-}_{j-\frac{1}{2}} \mathbf{w}^{-}_{j-\frac{1}{2}} + \Delta t a^{+}_{j-\frac{1}{2}} \mathbf{w}^{+}_{j-\frac{1}{2}} \\ & - \left(\Delta t \mathbf{f}(\mathbf{w}^{+}_{j-\frac{1}{2}}) - \Delta t \mathbf{f}(\mathbf{w}^{-}_{j-\frac{1}{2}}) \right) \Big] \end{aligned} \tag{1.85}$$

Thus, the Δt's take care of themselves and the limit in (1.84) may be written as follows.

$$\lim_{\Delta t \to 0} \bar{\mathbf{v}}_{j-\frac{1}{2}}^{n+1} = \frac{1}{(a_{j-\frac{1}{2}}^{+} - a_{j-\frac{1}{2}}^{-})} \Bigg[a_{j-\frac{1}{2}}^{+} \mathbf{w}_{j-\frac{1}{2}}^{+} - a_{j-\frac{1}{2}}^{-} \mathbf{w}_{j-\frac{1}{2}}^{-} - \Big(\mathbf{f}(\mathbf{w}_{j-\frac{1}{2}}^{+}) - \mathbf{f}(\mathbf{w}_{j-\frac{1}{2}}^{-}) \Big) \Bigg] \tag{1.86}$$

Note that we get the evaluation of the limit in the third term of the right-hand side of (1.84) for free by simply replacing the $j - \frac{1}{2}$ subscripts with $j + \frac{1}{2}$. This is written below for our convenience.

$$\lim_{\Delta t \to 0} \bar{\mathbf{v}}_{j+\frac{1}{2}}^{n+1} = \frac{1}{(a_{j+\frac{1}{2}}^{+} - a_{j+\frac{1}{2}}^{-})} \Bigg[a_{j+\frac{1}{2}}^{+} \mathbf{w}_{j+\frac{1}{2}}^{+} - a_{j+\frac{1}{2}}^{-} \mathbf{w}_{j+\frac{1}{2}}^{-} - \Big(\mathbf{f}(\mathbf{w}_{j+\frac{1}{2}}^{+}) - \mathbf{f}(\mathbf{w}_{j+\frac{1}{2}}^{-}) \Big) \Bigg] \tag{1.87}$$

Now we would like to address the middle term of the right-hand side of (1.84). Here we are working with the term reproduced for us below in equation (1.88). First, we substitute the expression for $\bar{\mathbf{v}}_j^{n+1}$ into the equation and then evaluate the integrals. The temporal integrals are evaluated analagously to the previous derivation. After noting that the spatial integral is simply a linear function, it is integrated as the product of the average of the values of the integrand at the endpoints of the interval of integration and the length of this interval. This is written in equation (1.90). Next, in equation (1.91), we perform some algebra to rearrange the terms. In this equation, we note that the first term is equal to the last term and thus negate

each other. Finally, we are left with the desired expression (1.92).

$$\lim_{\Delta t\to 0}\frac{1}{\Delta t}\left[\left(\frac{x^n_{j+\frac{1}{2},l}-x^n_{j-\frac{1}{2},r}}{\Delta x}\right)\bar{\mathbf{v}}^{n+1}_j-\bar{\mathbf{w}}^n_j\right] \tag{1.88}$$

$$=\lim_{\Delta t\to 0}\frac{1}{\Delta t}\left[\frac{(x^n_{j+\frac{1}{2},l}-x^n_{j-\frac{1}{2},r})}{\Delta x}\cdot\frac{1}{x^n_{j+\frac{1}{2},l}-x^n_{j-\frac{1}{2},r}}\left(\int_{x^n_{j-\frac{1}{2},r}}^{x^n_{j+\frac{1}{2},l}}\mathbf{p}^n_j(x)\,dx\right.\right.$$

$$\left.\left.-\int_{t^n}^{t^{n+1}}\Big(\mathbf{f}(\mathbf{w}(x^n_{j+\frac{1}{2},l},t))-\mathbf{f}(\mathbf{w}(x^n_{j-\frac{1}{2},r},t))\Big)\,dt\right)-\bar{\mathbf{w}}^n_j\right] \tag{1.89}$$

$$=\lim_{\Delta t\to 0}\frac{1}{\Delta t}\left[\frac{1}{\Delta x}\left(\frac{\Delta x+\Delta t(a^-_{j+\frac{1}{2}}-a^+_{j-\frac{1}{2}})}{2}\left(\mathbf{w}^-_{j+\frac{1}{2}}+\mathbf{w}^+_{j-\frac{1}{2}}\right)\right.\right.$$

$$\left.\left.-\Delta t\left(\mathbf{f}(\mathbf{w}^-_{j+\frac{1}{2}})-\mathbf{f}(\mathbf{w}^+_{j-\frac{1}{2}})\right)\right)-\bar{\mathbf{w}}^n_j\right] \tag{1.90}$$

$$=\lim_{\Delta t\to 0}\left[\frac{1}{2\Delta t}\left(\mathbf{w}^-_{j+\frac{1}{2}}+\mathbf{w}^+_{j-\frac{1}{2}}\right)+\frac{1}{\Delta x}\left(a^-_{j+\frac{1}{2}}\mathbf{w}^-_{j+\frac{1}{2}}-a^+_{j-\frac{1}{2}}\mathbf{w}^+_{j-\frac{1}{2}}\right)\right.$$

$$\left.-\frac{1}{\Delta x}\left(\mathbf{f}(\mathbf{w}^-_{j+\frac{1}{2}})-\mathbf{f}(\mathbf{w}^+_{j-\frac{1}{2}}\right)-\frac{1}{\Delta t}\bar{\mathbf{w}}^n_j\right] \tag{1.91}$$

$$=\frac{1}{\Delta x}\left(a^-_{j+\frac{1}{2}}\mathbf{w}^-_{j+\frac{1}{2}}-a^+_{j-\frac{1}{2}}\mathbf{w}^+_{j-\frac{1}{2}}\right)-\left(\mathbf{f}(\mathbf{w}^-_{j+\frac{1}{2}})-\mathbf{f}(\mathbf{w}^+_{j-\frac{1}{2}}\right). \tag{1.92}$$

Now we are ready to compute the right-hand side of (1.83). This accomplished by substituting in the limits evaluated in equations (1.85), (1.86), and (1.92). Then equation (1.83) becomes,

$$\begin{aligned}\frac{d}{dt}\bar{\mathbf{w}}_j(t)=&\frac{a^+_{j-\frac{1}{2}}}{\Delta x}\cdot\frac{1}{(a^+_{j-\frac{1}{2}}-a^-_{j-\frac{1}{2}})}\left[a^+_{j-\frac{1}{2}}\mathbf{w}^+_{j-\frac{1}{2}}-a^-_{j-\frac{1}{2}}\mathbf{w}^-_{j-\frac{1}{2}}-\left(\mathbf{f}(\mathbf{w}^+_{j-\frac{1}{2}})-\mathbf{f}(\mathbf{w}^-_{j-\frac{1}{2}})\right)\right]\\&+\frac{1}{\Delta x}\left(a^-_{j+\frac{1}{2}}\mathbf{w}^-_{j+\frac{1}{2}}-a^+_{j-\frac{1}{2}}\mathbf{w}^+_{j-\frac{1}{2}}\right)-\left(\mathbf{f}(\mathbf{w}^-_{j+\frac{1}{2}})-\mathbf{f}(\mathbf{w}^+_{j-\frac{1}{2}}\right)\\&-\frac{a^-_{j+\frac{1}{2}}}{\Delta x}\cdot\frac{1}{(a^+_{j+\frac{1}{2}}-a^-_{j+\frac{1}{2}})}\left[a^+_{j+\frac{1}{2}}\mathbf{w}^+_{j+\frac{1}{2}}-a^-_{j+\frac{1}{2}}\mathbf{w}^-_{j+\frac{1}{2}}-\left(\mathbf{f}(\mathbf{w}^+_{j+\frac{1}{2}})-\mathbf{f}(\mathbf{w}^-_{j+\frac{1}{2}})\right)\right].\end{aligned} \tag{1.93}$$

In keeping with the heuristics of finite-volume methods, we would like to express the right-hand side here as a difference in numerical fluxes at the cell boundaries. This is accomplished by separating the $\{j+\frac{1}{2}\}$ terms from the $\{j-\frac{1}{2}\}$ terms and performing some obligatory algebra.

Thus, the resulting CU scheme can be written in the conservative form as

$$\frac{d}{dt}\bar{\mathbf{w}}_j(t)=-\frac{\mathbf{H}_{j+\frac{1}{2}}(t)-\mathbf{H}_{j-\frac{1}{2}}(t)}{\Delta x}, \tag{1.94}$$

where the numerical fluxes are given by

$$\mathbf{H}_{j+\frac{1}{2}}(t)=\frac{a^+_{j+\frac{1}{2}}\mathbf{f}\left(\mathbf{w}^-_{j+\frac{1}{2}}\right)-a^-_{j+\frac{1}{2}}\mathbf{f}\left(\mathbf{w}^+_{j+\frac{1}{2}}\right)}{a^+_{j+\frac{1}{2}}-a^-_{j+\frac{1}{2}}}+\frac{a^+_{j+\frac{1}{2}}a^-_{j+\frac{1}{2}}}{a^+_{j+\frac{1}{2}}-a^-_{j+\frac{1}{2}}}\left[\mathbf{w}^+_{j+\frac{1}{2}}-\mathbf{w}^-_{j+\frac{1}{2}}\right]. \tag{1.95}$$

The expression for the CU numerical flux $\mathbf{H}_{j-\frac{1}{2}}(t)$ is analogous to the numerical flux at $x_{j+\frac{1}{2}}$.

Semidiscrete scheme for 2-D conservation laws

The one-dimesional semi-discrete central-upwind scheme can be generalized to the two-dimensional case by applying the one-dimensional numerical flux in both the x and y directions [66]. The scheme is presented below. Let us consider the two-dimensional conservation law

$$\mathbf{w}_t+\mathbf{f}(\mathbf{w})_x+\mathbf{g}(\mathbf{w})_y=0. \tag{1.96}$$

We again consider uniform spatial grids and use the notation: $x_j=j\Delta x,\ y_k=k\Delta y,\ x_{j\pm\frac{1}{2}}=x_j\pm\frac{\Delta x}{2},\ y_{k\pm\frac{1}{2}}=y_k\pm\frac{\Delta y}{2},\ t^n=n\Delta t,\ \mathbf{w}^n_{(j,k)}=\mathbf{w}(x_j,y_k,t^n)$. We begin with an appropriate order conservative piecewise polynomial reconstruction,

$$\tilde{\mathbf{w}}(x,y,t^n)=\sum_{j,k}\mathbf{p}^n_{j,k}(x,y)\chi_{j,k}, \tag{1.97}$$

where $\chi_{j,k}$ is the characteristic function over the the $(j,k)^{th}$ cell, $\mathcal{C}_{j,k}=[x_{j-\frac{1}{2}},x_{j+\frac{1}{2}}]\times[y_{k-\frac{1}{2}},y_{k+\frac{1}{2}}]$. Here we use the generalized minmod piecewise linear reconstruction at time t^n, given by

$$\mathbf{p}_{j,k}:=\tilde{\mathbf{w}}(x,y)=\bar{\mathbf{w}}_{j,k}+(\mathbf{w}_x)_{j,k}(x-x_j)+(\mathbf{w}_y)_{j,k}(y-y_k),\quad (x,y)\in\mathcal{C}_{j,k}. \tag{1.98}$$

The cell average, $\bar{\mathbf{w}}_{j,k}$, is given by

$$\bar{\mathbf{w}}_{j,k}(t)=\iint\limits_{\mathcal{C}_{j,k}}\mathbf{w}(x,y,t)dxdy. \tag{1.99}$$

The numerical derivatives in (1.98) are computed componentwise using the minmod slope limiter, with $\theta \in [1,2]$, introduced in the one-dimensional case. I.e.,

$$(\mathbf{w}_x)_{j,k} \approx \text{minmod}\left(\theta\frac{\bar{\mathbf{w}}(x+\Delta x,y)-\bar{\mathbf{w}}(x,y)}{\Delta x}, \frac{\bar{\mathbf{w}}(x+\Delta x,y)-\bar{\mathbf{w}}(x-\Delta x,y)}{2\Delta x}, \theta\frac{\bar{\mathbf{w}}(x,y)-\bar{\mathbf{w}}(x-\Delta x,y)}{\Delta x}\right), \tag{1.100}$$

$$(\mathbf{w}_y)_{j,k} \approx \text{minmod}\left(\theta\frac{\bar{\mathbf{w}}(x,y+\Delta y)-\bar{\mathbf{w}}(x,y)}{\Delta y}, \frac{\bar{\mathbf{w}}(x,y+\Delta y)-\bar{\mathbf{w}}(x,y-\Delta y)}{2\Delta y}, \theta\frac{\bar{\mathbf{w}}(x,y)-\bar{\mathbf{w}}(x,y-\Delta y)}{\Delta y}\right). \tag{1.101}$$

The point values at the flux interfaces are computed using the values of the linear reconstruction at the interfaces. These are denoted by the superscripts E, W, N, S, representing east, west, north, and south. These point values are given below.

$$\mathbf{w}^E_{j,k} = \bar{\mathbf{w}}_{j,k} + \frac{\Delta x}{2}(\mathbf{w}_x)_{j,k}, \quad \mathbf{w}^W_{j,k} = \bar{\mathbf{w}}_{j,k} - \frac{\Delta x}{2}(\mathbf{w}_x)_{j,k}, \tag{1.102}$$

$$\mathbf{w}^N_{j,k} = \bar{\mathbf{w}}_{j,k} + \frac{\Delta y}{2}(\mathbf{w}_y)_{j,k}, \quad \mathbf{w}^S_{j,k} = \bar{\mathbf{w}}_{j,k} - \frac{\Delta y}{2}(\mathbf{w}_y)_{j,k}. \tag{1.103}$$

As in the one-dimensional case, we may have discontinuities along $x = x_{j\pm\frac{1}{2}}$ or $y = y_{j\pm\frac{1}{2}}$. The one-sided local speeds of propagation are estimated by the Jacobians of the flux functions, $\mathbf{f}(\mathbf{w})$ and $\mathbf{g}(\mathbf{w})$, in each direction. These values are given below, where a refers to the speeds in the x-direction and b refers to the speed in the y-direction.

$$a^+_{j+\frac{1}{2},k} = \max\left\{\lambda_N\left(\frac{\partial \mathbf{f}}{\partial \mathbf{w}}(\mathbf{w}^W_{j+1,k}\right), \lambda_N\left(\frac{\partial \mathbf{f}}{\partial \mathbf{w}}(\mathbf{w}^E_{j,k})\right), 0\right\}, \tag{1.104}$$

$$a^-_{j+\frac{1}{2},k} = \min\left\{\lambda_1\left(\frac{\partial \mathbf{f}}{\partial \mathbf{w}}(\mathbf{w}^W_{j+1,k}\right), \lambda_1\left(\frac{\partial \mathbf{f}}{\partial \mathbf{w}}(\mathbf{w}^E_{j,k})\right), 0\right\}, \tag{1.105}$$

$$b^+_{j,k+\frac{1}{2}} = \max\left\{\lambda_N\left(\frac{\partial \mathbf{g}}{\partial \mathbf{w}}(\mathbf{w}^S_{j,k+1}\right), \lambda_N\left(\frac{\partial \mathbf{g}}{\partial \mathbf{w}}(\mathbf{w}^N_{j,k})\right), 0\right\}, \tag{1.106}$$

$$b^-_{j,k+\frac{1}{2}} = \min\left\{\lambda_1\left(\frac{\partial \mathbf{g}}{\partial \mathbf{w}}(\mathbf{w}^S_{j,k+1}\right), \lambda_1\left(\frac{\partial \mathbf{g}}{\partial \mathbf{w}}(\mathbf{w}^N_{j,k})\right), 0\right\}. \tag{1.107}$$

As in the one-dimensional case, the semi-discrete scheme by integrating over the non-uniform domains corresponding to the smooth and non-smooth regions of the reconstruction. After projecting back to the original grid and taking limits we obtain the following semi-discrete, two-dimensional scheme:

$$\frac{d}{dt}\bar{\mathbf{w}}_{j,k}(t) = -\frac{\mathbf{H}^x_{j+\frac{1}{2},k} - \mathbf{H}^x_{j-\frac{1}{2},k}}{\Delta x} - \frac{\mathbf{H}^y_{j,k+\frac{1}{2}} - \mathbf{H}^y_{j,k-\frac{1}{2}}}{\Delta y}, \tag{1.108}$$

with the numerical fluxes $\mathbf{H}^x$ and $\mathbf{H}^y$ are given by,

$$\mathbf{H}^x_{j+\frac{1}{2},k}(t) = \frac{a^+_{j+\frac{1}{2},k}\mathbf{f}\left(\mathbf{w}^E_{j,k}\right) - a^-_{j+\frac{1}{2},k}\mathbf{f}\left(\mathbf{w}^W_{j+1,k}\right)}{a^+_{j+\frac{1}{2},k} - a^-_{j+\frac{1}{2},k}} + \frac{a^+_{j+\frac{1}{2},k}a^-_{j+\frac{1}{2},k}}{a^+_{j+\frac{1}{2},k} - a^-_{j+\frac{1}{2},k}}\left[\mathbf{w}^W_{j+1,k} - \mathbf{w}^E_{j,k}\right], \quad (1.109)$$

$$\mathbf{H}^y_{j,k+\frac{1}{2}}(t) = \frac{b^+_{j,k+\frac{1}{2}}\mathbf{g}\left(\mathbf{w}^N_{j,k}\right) - b^-_{j,k+\frac{1}{2}}\mathbf{g}\left(\mathbf{w}^S_{j,k+1}\right)}{b^+_{j,k+\frac{1}{2}} - b^-_{j,k+\frac{1}{2}}} + \frac{b^+_{j,k+\frac{1}{2}}b^-_{j,k+\frac{1}{2}}}{b^+_{j,k+\frac{1}{2}} - b^-_{j,k+\frac{1}{2}}}\left[\mathbf{w}^S_{j,k+1} - \mathbf{w}^N_{j,k}\right]. \quad (1.110)$$

1.2.3 Finite Difference Methods

Finite difference methods consist of a discrete grid and a grid function that represent a differential equation by replacing the derivatives by finite difference approximations. For linear problems, this results in a large system of algebraic equations which may be solved by computer. The solution to the finite difference scheme is realized as an approximation to the point values of the exact solution. Finite difference schemes are generally straight forward and easy to implement. Also, they are readily applicable to all linear and non-linear partial differential equations, with the caveat that stability and accuracy issues may be overwhelming.

Let $w(x,t)$ be a smooth function in one dimension. A one-sided approximation may be used to obtain a first-order accurate approximation to the spatial derivative w_x at the point $(\bar{x},t)$. The left and right one-sided approximations are given below:

$$w_x(\bar{x},t) \approx \frac{w(\bar{x}+\Delta x,t) - w(\bar{x},t)}{\Delta x}, \text{ or} \quad (1.111)$$

$$\approx \frac{w(\bar{x},t) - w(\bar{x}-\Delta x,t)}{\Delta x}. \quad (1.112)$$

A second-order accurate approximation of the second spatial derivative w_{xx} at the point $(\bar{x},t)$ is given by

$$w_{xx}(\bar{x},t) \approx \frac{w(\bar{x}-\Delta x,t) - 2w(\bar{x},t) + w(\bar{x}+\Delta x,t)}{(\Delta x)^2}. \quad (1.113)$$

Furthermore, in the following, we encounter parabolic diffusion in the form

$$w_t = (\Lambda w_x)_x. \quad (1.114)$$

Now, the right-hand side of (1.114) is discretized conservatively. To maintain second order accuracy the following finite difference scheme is used, where Λ is approximated using the midpoint rule and the derivatives are approximated by one-sided differences. This scheme uses

a smaller stencil than using central differences for the derivatives while maintaing second-order.

$$\begin{aligned}\frac{dw_j}{dt} &= \frac{1}{\Delta x}\left[\frac{\Lambda_{j+1}+\Lambda_j}{2}\frac{w_{j+1}-w_j}{\Delta x} - \frac{\Lambda_j+\Lambda_{j-1}}{2}\frac{w_j-w_{j-1}}{\Delta x}\right] \\ &= \frac{1}{2\Delta x^2}\left[(\Lambda_{j+1}+\Lambda_j)(w_{j+1}-w_j) - (\Lambda_j+\Lambda_{j-1})(w_j-w_{j-1})\right] \\ &= \frac{1}{2\Delta x^2}\left[\Lambda_{j+1}\left(w_{j+1}-w_j\right) + \Lambda_j\left(w_{j+1}-2w_j+w_{j-1}\right) + \Lambda_{j-1}\left(w_{j-1}-w_j\right)\right]. \end{aligned} \tag{1.115}$$

If we discretize the left-hand side of (1.115) using an explicit ODE solver then, analogous to the heat equation, the method is restricted by the CFL condition of $\Delta t \sim (\Delta x)^2$ (see Appendix **??**). The two dimensional setup is described in detail in Section 5.2.

In the two-dimensional functions encountered later, the need arises for the computation of mixed derivatives. These can, in general, be derived by applying a finite difference in one direction, and then reapplying the finite difference in the next direction. Say we would like to find an approximation for the mixed derivative w_{xy} at the point $(\bar{x}, \bar{y})$. Assume $w(x, y)$ is smooth. If we first apply a second-order accurate centered difference in the x direction and then apply the same centered difference in the y direction, we obtain the following approximation:

$$w_{xy} \approx \frac{w(\bar{x}+\Delta x, \bar{y}+\Delta y) - w(\bar{x}-\Delta x, \bar{y}+\Delta y)}{4\Delta x \Delta y} - \frac{w(\bar{x}+\Delta x, \bar{y}-\Delta y) - w(\bar{x}-\Delta x, \bar{y}-\Delta y)}{4\Delta x \Delta y} \tag{1.116}$$

1.2.4 ODE Solvers

It is common practice when solving time-dependent PDEs to obtain a semidiscrete method of lines scheme. The result is an ODE system in the time variable. This allows for the utilization of an appropriate ODE solver, of which there are many to choose from. See, e.g., [9, 51, 91, 34, 90, 58, 59, 38, 73, 103, 52, 39, 44, 45].

For hyperbolic conservation laws, the method of lines approximation results in

$$\mathbf{w}_t = L(\mathbf{w}), \tag{1.117}$$

where $L(\mathbf{w})$ denotes the spatial discretization of the PDE, e.g., see the semidiscrete central upwind scheme (1.108).

This allows us to apply appropriate ODE solvers depending on the problem. We chose the strong stability preserving (SSP) high-order method presented in [43] in order to take advantage of the stability it provides and the positivity preserving.

In particular, we us the optimal third-order SSP Runge-Kutta method given by

$$\begin{aligned}
\mathbf{w}^{(1)} &= \mathbf{w}^n + \Delta t L(\mathbf{w}^n), \\
\mathbf{w}^{(2)} &= \frac{3}{4}\mathbf{w}^n + \frac{1}{4}\mathbf{w}^{(1)} + \frac{1}{4}\Delta t L(\mathbf{w}^{(1)}), \\
\mathbf{w}^{n+1} &= \frac{1}{3}\mathbf{w}^n + \frac{2}{3}\mathbf{w}^{(2)} + \frac{2}{3}\Delta t L(\mathbf{w}^{(2)}).
\end{aligned} \tag{1.118}$$

We also utilize the the variable time-step DUMKA procedure put forth in [94, 93]. This high-order integration produces accurate results, and its larger stability domains (in comparison with the standard Runge-Kutta methods) allow for larger time steps; the explicit form retains simplicity, and the embedded formulas permit an efficient stepsize control. In practice these methods preserve all the advantages of explicit methods and work as fast as implicit methods.

Chapter 2

One-Dimensional Laser Ablation - Single Gas

2.1 Mathematical Model

The quasi-gas dynamic (QGD) equations are a mathematical model for gas and fluid dynamic problem [35]. We now present the model derived in a general multi-dimensional setting, as given in [35]. We then move to the one-dimensional description of the single gas model in the following sections. The equations are a generalization of the Navier-Stokes equations. The QGD equations include dissipative terms which are attenuated by a small parameter. This parameter, called the relaxation parameter, is used to promote numerical stability. Thus the QGD equations are applicable to a wider range of problems. Similar to the derivation of the Euler and Navier-Stokes equations, the QGD equations can be derived from the general system of conservation laws. The essential distinction of the derivation of the QGD equations from the Navier-Stokes equations is the use of time-spatial averaging in defining the quantities of interest of the fluid, namely velocity, density, and temperature. The extra terms in the QGD equations arise from the additional smoothing provided by the time averaging.

The modeling of gas-dynamic problems may be carried out using the Newton equations to describe the motion of each atom. However, this is not practical due to the large number of atoms that need to be described. Kinetic theory takes into account the collisions between molecules to explain pressure. In classical fluid dynamics, the approach uses averaging procedures to transition from the large number of separate particles to the continuous description. In the Navier-Stokes theory, spatial averaging is used as follows.

The spatial averages are obtained by averaging the quantities over a given volume. Let ΔV be the volume of a ball of radius r, and let $N(t)$ be the number of molecules present inside the ball at time t. Then we have the following definitions for the average density, momentum, and

energy, where m_0 is the mass of a particle and $\tilde{\mathbf{u}}_i, \quad i = 1 \dots N(t)$, are the velocities of each particle and $\mathbf{x}$ is the vector of spatial variables.

$$\rho(\mathbf{x}, t) = \frac{m_0}{\Delta V} N(t) \tag{2.1}$$

$$(\rho \mathbf{u})(\mathbf{x}, t) = \frac{m_0}{\Delta V} \sum_{i=1}^{N(t)} \tilde{\mathbf{u}}_i(t) \tag{2.2}$$

$$E(\mathbf{x}, t) = \frac{m_0}{\Delta V} \sum_{i=1}^{N(t)} \frac{\|\tilde{\mathbf{u}}_i\|^2(t)}{2} \tag{2.3}$$

Spatial-time averaging includes an additional smoothing out over time. Over a small time interval Δt we get the following expressions for the quantities given above.

$$\rho(\mathbf{x}, t) = \frac{m_0}{\Delta V} \int_t^{t+\Delta t} N(\tau)\, d\tau, \tag{2.4}$$

$$(\rho \mathbf{u})(\mathbf{x}, t) = \frac{m_0}{\Delta V} \int_t^{t+\Delta t} \sum_{j=1}^{N(t)} \tilde{\mathbf{u}}_i(\tau)\, d\tau, \tag{2.5}$$

$$E(\mathbf{x}, t) = \frac{m_0}{\Delta V} \int_t^{t+\Delta t} \sum_{j=1}^{N(t)} \frac{\|\tilde{\mathbf{u}}_i\|^2(\tau)}{2}\, d\tau. \tag{2.6}$$

In traditional fluid mechanics, the mass flux density is given by $\mathbf{j}_m = \rho \tilde{\mathbf{u}}$. In spatial averaging the principle of mass conservation holds. I.e.,

$$\frac{\partial \rho(\mathbf{x}, t)}{\partial t} + \operatorname{div}(\rho(\mathbf{x}, t) \tilde{\mathbf{u}}(\mathbf{x}, t)) = 0. \tag{2.7}$$

However, in spatial-time averaging the instantaneous values of momentum and density may change over Δt. Therefore, we must express the mass flux density in a more general form by adding a term to the velocity that accounts for the gradient of the velocity vector. In the QGD equations this is done by writing the mass flux density as $\mathbf{j}_m = \rho(\tilde{\mathbf{u}} - \mathbf{w})$. This extra term begets the differences between the QGD equations and the Navier-Stokes equations.

The additional dissipative terms introduced by the averaging of time in the gas dynamic equations consist of spatial derivatives of ρ, $\tilde{\mathbf{u}}$ and p multiplied by the so-called relaxation parameter $\tau = \tau(\rho, T)$, [35]. This additional averaging takes into account the influence of small fluctuations in the number of particles in a small volume Δv and has the dimensions of time. These fluctuations are neglected in classical gas dynamics. This addition is introduced in [35]

as

$$\mathbf{w} = \tau \left(\mathrm{div}(\rho \tilde{\mathbf{u}} \otimes \tilde{\mathbf{u}}) + \bigtriangledown p - \rho \phi \right). \tag{2.8}$$

The only foreign term is the force of the exterior field, ϕ, which is ignored in the following derivation, [35]. This expression can be rewritten and substituted into the mass flux density equation to obtain

$$\mathbf{j}_m = \rho(\mathbf{u} - \mathbf{w}) = \rho \mathbf{u} - \tau \mathrm{div}(\rho \mathbf{u} \otimes \mathbf{u}) - \tau R T \bigtriangledown \rho - \tau R \rho \bigtriangledown T. \tag{2.9}$$

The first term is the contribution to the mass flux density by the convective motion of the gas. The second term is the contribution given by the gradient in velocity. The third and fourth terms account for self-diffusion and thermo-diffusion, respectively.

The relaxation parameter τ is essentially proportional to the Maxwell relaxation time, μ/p, where μ is the coefficient of viscosity. It can be determined by individually examining the terms in (2.9). E.g., let us consider the third term which accounts for self-diffusion. The self-diffusion coefficient is known from experiments for many media. For polytropic gases, this coefficient is given by

$$D = \frac{\mu}{\rho \mathrm{Sc}}, \tag{2.10}$$

where Sc is the Schmidt number. The mass flux density that accounts for self-diffusion has the form

$$j_\rho = -D \bigtriangledown \rho. \tag{2.11}$$

Comparing this with the third term in equation (2.9), we see that $\frac{\mu}{\rho \mathrm{Sc}} = \tau R T$. This provides us with the following expression for τ,

$$\tau = \frac{\mu}{\rho \mathrm{Sc}} \cdot \frac{1}{RT} = \frac{\mu}{p \mathrm{Sc}}. \tag{2.12}$$

By examining the other terms in the mass flux density we arrive at similar formulas for τ, with different orders of accuracy, see [35].

When performing computer simulations, however, τ no longer must be related to the molecular properties of the gas. It may be determined by the mesh size, convergence conditions, and accuracy concerns of the numerical problem [35]. There are many examples of artificial viscosity in literature, see, e.g., [24, 118].

Plasma Expansion into Vacuum

Now we present the model for plasma expansion into a vacuum after fast evaporation of the target material caused by the laser blast. We consider here the one-dimensional (1-D) problem, in which a laser pulse strikes a graphite target at a small angle to its axis. The gas is described by three functions of the Eulerian coordinate x and time t. We have $\rho(x,t)$ - gas density, $u(x,t)$ - macroscopic velocity, and $p(x,t)$ - pressure. The quasi-gas dynamic (QGD) equations that describe the model are a consequence of integral conservation laws, [35], and are given by

$$\frac{\partial \rho}{\partial t} + \frac{\partial j_m}{\partial x} = 0, \tag{2.13}$$

$$\frac{\partial (\rho u)}{\partial t} + \frac{\partial (j_m u)}{\partial x} + \frac{\partial p}{\partial x} = \frac{\partial \Pi}{\partial x} \tag{2.14}$$

$$\frac{\partial E}{\partial t} + \frac{\partial (j_m H)}{\partial x} + \frac{\partial q}{\partial x} = \frac{\partial \Pi u}{\partial x} + Q \tag{2.15}$$

$$j_m = \rho(u - w), \quad w = \frac{\tau}{\rho}\frac{\partial}{\partial x}(\rho u^2 + p). \tag{2.16}$$

The energy E is related to pressure by the equation of state given in (1.37). The total specific enthalpy H is calculated by

$$H = \frac{E + p}{\rho}, \tag{2.17}$$

and the temperature T is determined by the ideal gas law,

$$T = \frac{p}{\rho R}, \tag{2.18}$$

where the gas constant $R = \mathcal{R}/M_{mol}$ is calculated via the absolute gas constant, $\mathcal{R}$, and the molar mass of the gas, M_{mol}. The other components entering into the equations (2.13)–(2.16) are given by

$$\Pi = \Pi^{NS} + \tau \left[u \left(\rho u u_x + p_x \right) + \left(u p_x + \gamma p u_x \right) \right], \tag{2.19}$$

$$\Pi^{NS} = \left(\frac{4}{3}\eta + \eta \left(\frac{5}{3} - \gamma \right) B \right) \frac{\partial u}{\partial x}, \tag{2.20}$$

$$q = q^{NS} - \tau \rho u \left[\frac{u}{\gamma - 1} \frac{\partial}{\partial x} \left(\frac{p}{\rho} \right) + p u \frac{\partial}{\partial x} \left(\frac{1}{\rho} \right) \right], \tag{2.21}$$

$$q^{NS} = -\kappa \frac{\partial T}{\partial x}. \tag{2.22}$$

Equation (2.19) represents the viscous stress tensor. The first term Π^{NS} is the viscous stress component from the Navier-Stokes (NS) equations with regard to bulk viscosity, [11]. Equation (2.21) is the heat flux, in which the first term q^{NS} is the thermal conductivity component from

the NS equations. The term Q in equation (2.15) for energy describes gas heating by optical radiation.

By expanding the j_m terms in equation (2.13)-(2.16), we obtain a representation of the quasi-gas dynamics equations that discernibly consists of Euler's equations of gas dynamics. This is given below, where w is given in (2.16).

$$\rho_t + (\rho u)_x = (\rho w)_x, \tag{2.23}$$

$$(\rho u)_t + (\rho u^2 + p)_x = \Pi_x + (\rho w u)_x, \tag{2.24}$$

$$E_t + ((E+p)u)_x = (\Pi u)_x + Q - q_x + (w(E+p))_x. \tag{2.25}$$

The coefficient B in (2.19) is taken in the form,

$$B = Z_{rot}(\gamma - 1)(7 - 2\omega)(5 - 2\omega)/20, \tag{2.26}$$

where

$$Z_{rot} = 23/\left(1 + 0.5\sqrt{91.5\pi^3/T} + (\pi + \pi^2/4)(91.5/T)\right), \tag{2.27}$$

and constant $\omega > 0$ describes the intermolecular interaction in the gas, see, e.g., [18, 35].

The parameter τ may be chosen experimentally to necessitate computational stability. The dynamic viscosity η and thermal conductivity κ are related to τ by the following equations:

$$\tau = \frac{\eta}{pSc}, \qquad \kappa = \frac{\eta\gamma R}{Pr\,(\gamma - 1)}, \tag{2.28}$$

with Pr and Sc being the Prandtl and Schmidt numbers, respectively.

Relation between the QGD and Navier-Stokes Equations

The QGD equations (2.13)–(2.16) differ from the NS equations (1.32)-(1.34) in additional terms involving the relaxation parameter τ as a coefficient [11, 35, 74], and are distinct from the NS equations in that the conserved quantities are found using time-spatial averaging versus the spatial averaging used in NS equations. The QGD equations are dissipative as demonstrated by the theorem of nondecreasing total thermodynamic entropy in a closed volume in [35] and act as regularizers.

As mentioned previously, the QGD equations become the NS equations when $\tau = 0$. To retrieve the NS equations we need to prescribe theoretical values for the dynamic viscosity η and the thermal conductivity κ, since in the previous derivation they are tied to τ. This is

accomplished with the following formulas:

$$\eta = \eta^* \left(\frac{T}{T^*}\right)^{\omega}, \qquad \kappa = \frac{\eta\gamma R}{Pr(\gamma-1)}. \tag{2.29}$$

Here the $*$ notation refers to standard conditions. For nitrogen these are $T^* = 300$ K, $P^* = 10^5$ Pa and $\eta^* = 1.66 \times 10^{-5}$ kg/ms.

2.2 Numerics

In this section, we provide an overview of the numerics involved in computing the solution to the QGD system described in the previous section.

We first rewrite the system (2.13)–(2.15) in the vector form:

$$\mathbf{u}_t + \mathbf{f}(\mathbf{u})_x = \mathbf{D}(\mathbf{u}). \tag{2.30}$$

Here, $\mathbf{u}$ is the unknown vector of conservative variables, $\mathbf{f}$ represents the the convective nonlinear flux and $\mathbf{D}$ the nonlinear diffusion term:

$$\mathbf{u} = \begin{pmatrix} \rho \\ \rho u \\ E \end{pmatrix}, \quad \mathbf{f}(\mathbf{u}) = \begin{pmatrix} \rho u \\ \rho u^2 + p \\ (E+p)u \end{pmatrix}, \quad \mathbf{D}(\mathbf{u}) = \begin{pmatrix} (\rho w)_x \\ (\Pi + \rho w u)_x \\ (\Pi u - q + w(E+p))_x \end{pmatrix}. \tag{2.31}$$

Note that Q in equation (2.15), describing heating by optical radiation, is taken to be identically zero, and w is given in (2.16).

In the following discussion we consider (for simplicity) a uniform spatial grid of size Δx and use the notation: $x_j = j\Delta x$, $x_{j\pm\frac{1}{2}} = (j \pm \frac{1}{2})\Delta x$. According to the central-upwind approach, the computed solution is realized at each time t in terms of cell averages,

$$\overline{\mathbf{u}}_j(t) = \frac{1}{\Delta x} \int\limits_{x_{j-\frac{1}{2}}}^{x_{j+\frac{1}{2}}} \mathbf{u}(x,t)\,dx, \tag{2.32}$$

which are evolved in time by solving the following system of ODEs:

$$\frac{d}{dt}\overline{\mathbf{u}}_j(t) = -\frac{\mathbf{H}_{j+\frac{1}{2}}(t) - \mathbf{H}_{j-\frac{1}{2}}(t)}{\Delta x} + \frac{\mathbf{P}_{j+\frac{1}{2}}(t) - \mathbf{P}_{j-\frac{1}{2}}(t)}{\Delta x}, \tag{2.33}$$

where the hyperbolic $\mathbf{H}_{j+\frac{1}{2}}$ and parabolic $\mathbf{P}_{j+\frac{1}{2}}$ numerical fluxes are constructed as follows (in the sequel, we assume that the cell averages (2.32) are available at some time level t and supress the dependence of all the variables on time to simplify the notation).

Computation of Hyperbolic Numerical Fluxes

Following [66], in order to compute the hyperbolic fluxes, $\mathbf{H}_{j+\frac{1}{2}}$, we first use the cell averages (2.32) to reconstruct a conservative second-order piecewise linear interpolant:

$$\widetilde{\mathbf{u}}_j(x) = \overline{\mathbf{u}}_j + (\mathbf{u}_x)_j(x - x_j), \quad x \in [x_{j-\frac{1}{2}}, x_{j+\frac{1}{2}}], \tag{2.34}$$

where $(\mathbf{u}_x)_j$ are (at least) first-order approximations of the partial derivative $\mathbf{u}_x(x_j, t))$, computed using the nonlinear limiter described in (1.68) to ensure a nonoscillatory nature of the reconstruction (2.34).

The hyperbolic numerical fluxes are then computed according to (1.95) as

$$\mathbf{H}_{j+\frac{1}{2}} = \frac{a^+_{j+\frac{1}{2}}\mathbf{f}\left(\mathbf{u}^-_{j+\frac{1}{2}}\right) - a^-_{j+\frac{1}{2}}\mathbf{f}\left(\mathbf{u}^+_{j+\frac{1}{2}}\right)}{a^+_{j+\frac{1}{2}} - a^-_{j+\frac{1}{2}}} + \frac{a^+_{j+\frac{1}{2}}a^-_{j+\frac{1}{2}}}{a^+_{j+\frac{1}{2}} - a^-_{j+\frac{1}{2}}}\left[\mathbf{u}^+_{j+\frac{1}{2}} - \mathbf{u}^-_{j+\frac{1}{2}}\right]. \tag{2.35}$$

Here $\mathbf{f}$ is the nonlinear convective flux vector function, defined in (2.31), $\mathbf{u}^{\pm}_{j+\frac{1}{2}}$ are point values of piecewise linear reconstruction (2.34):

$$\mathbf{u}^+_{j+\frac{1}{2}} = \widetilde{\mathbf{u}}_{j+1}(x_{j+\frac{1}{2}}) = \overline{\mathbf{u}}_{j+1} - \frac{\Delta x}{2}(\mathbf{u}_x)_{j+1}, \qquad \mathbf{u}^-_{j+\frac{1}{2}} = \widetilde{\mathbf{u}}_j(x_{j+\frac{1}{2}}) = \overline{\mathbf{u}}_j + \frac{\Delta x}{2}(\mathbf{u}_x)_j,$$

and $a^{\pm}_{j+\frac{1}{2}}$ the right- and left-sided local speeds, which are obtained from the largest and smallest eigenvalues of the Jacobian $\frac{\partial \mathbf{f}}{\partial \mathbf{u}}$ and can be estimated by

$$a^+_{j+\frac{1}{2}} = \max\left\{u^-_{j+\frac{1}{2}} + c^-_{j+\frac{1}{2}}, u^+_{j+\frac{1}{2}} + c^+_{j+\frac{1}{2}}, 0\right\}, \quad a^-_{j+\frac{1}{2}} = \min\left\{u^-_{j+\frac{1}{2}} - c^-_{j+\frac{1}{2}}, u^+_{j+\frac{1}{2}} - c^+_{j+\frac{1}{2}}, 0\right\}, \tag{2.36}$$

where u is the macroscopic velocity and $c = \sqrt{\frac{\gamma p}{\rho}}$ is the speed of sound (see Section 1.1.2). Note that the piecewise linear reconstruction provides second-order accuracy. A piecewise parabolic reconstruction would provide a third-order method, and so on.

Computation of Parabolic Numerical Fluxes

The parabolic numerical fluxes, $\mathbf{P}_{j+\frac{1}{2}}$, are computed (see Section 1.2.3) by expressing the parabolic flux (2.31) in the following computationally apt form:

$$\mathbf{D}(\mathbf{u}) = \frac{\partial}{\partial x}\begin{pmatrix} \tau W_x \\ \tau u W_x + \tau S_x \\ \tau\left(\frac{u^2}{2} + \frac{c^2}{\gamma - 1}\right)W_x + \tau u S_x + \tau Q_x \end{pmatrix}. \tag{2.37}$$

Note that since viscosity and and thermal conductivity are taken proportional to τ, $\mathbf{D}(\mathbf{u})$ is also proportional to τ. The terms in (2.37) are defined below (note that $W_x = \frac{\rho}{\tau} w$):

$$\begin{aligned} W_x &= (\rho u^2 + p)_x, \\ S_x &= 2up_x + Vu_x, \quad V = \left(\rho u^2 + p\left(\gamma + \mathrm{Sc}\left(\frac{4}{3} + \left(\frac{5}{3} - \gamma\right)B\right)\right)\right), \\ Q_x &= G\rho_x - Fp_x, \quad G = \mathrm{R}T\left(\frac{\mathrm{Sc}\gamma}{\mathrm{Pr}(\gamma-1)}\mathrm{R}T + \frac{\gamma u^2}{\gamma - 1}\right), \quad F = \left(\frac{\mathrm{Sc}\gamma}{\mathrm{Pr}(\gamma-1)}\mathrm{R}T + \frac{u^2}{\gamma-1}\right). \end{aligned} \tag{2.38}$$

The parabolic numerical flux is then written in component form as $\mathbf{P}_{j+\frac{1}{2}} = \left(P^{(1)}_{j+\frac{1}{2}}, P^{(2)}_{j+\frac{1}{2}}, P^{(3)}_{j+\frac{1}{2}}\right)^T$, where the individual components are computed in the following manner:

$$P^{(1)}_{j+\frac{1}{2}} = \tau_{j+\frac{1}{2}} \Delta W_j, \tag{2.39}$$

$$P^{(2)}_{j+\frac{1}{2}} = P^{(1)}_{j+\frac{1}{2}} u_{j+\frac{1}{2}} + \tau_{j+\frac{1}{2}} \Delta S_j, \tag{2.40}$$

$$P^{(3)}_{j+\frac{1}{2}} = P^{(1)}_{j+\frac{1}{2}} \left(\frac{u^2_{j+\frac{1}{2}}}{2} + \frac{c^2_{j+\frac{1}{2}}}{\gamma - 1}\right) + \tau_{j+\frac{1}{2}} u_{j+\frac{1}{2}} \Delta S_j + \tau_{j+\frac{1}{2}} \Delta Q_j, \tag{2.41}$$

where $u_{j+\frac{1}{2}} := \dfrac{u^+_{j+\frac{1}{2}} + u^-_{j+\frac{1}{2}}}{2}$ and $c_{j+\frac{1}{2}} := \dfrac{c^+_{j+\frac{1}{2}} + c^-_{j+\frac{1}{2}}}{2}$. In (2.39)–(2.41), we have the expression $\Delta W_j, \Delta S_j$ and ΔQ_j, which are given by

$$\begin{aligned} \Delta W_j &= \frac{W_{j+1} - W_j}{\Delta x}, \\ \Delta S_j &= 2u_{j+\frac{1}{2}}\left(\frac{p_{j+1} - p_j}{\Delta x}\right) + V_{j+\frac{1}{2}}\left(\frac{u_{j+1} - u_j}{\Delta x}\right), \\ \Delta Q_j &= F_{j+\frac{1}{2}}\left(\frac{\overline{\rho}_{j+1} - \overline{\rho}_j}{\Delta x}\right) - G_{j+\frac{1}{2}}\left(\frac{p_{j+1} + p_j}{\Delta x}\right), \end{aligned}$$

with, for example, $W_j = W(\mathbf{u}_j)$, $V_{j+\frac{1}{2}} = V(\mathbf{u}_{j+\frac{1}{2}})$ and $\mathbf{u}_{j+\frac{1}{2}} := \dfrac{\mathbf{u}^+_{j+\frac{1}{2}} + \mathbf{u}^-_{j+\frac{1}{2}}}{2}$.

Temporal Integration

The resulting semi-discretization (2.33) is a system of time-dependent ODEs that should be solved by a stable ODE solver of an appropriate order. The stiffness of this system makes the choice of integrator important. For the quasi-gas dynamic experiments, we use the nonlinear SSP Runge-Kutta method (1.118) from [43] presented in Section 1.2.4. The ability to precisely control the CFL number with respect to the amount of diffusion prescribed by the model allows for the most accurate and efficient results. For the more computational challenging Navier-

Stokes simulations we have used the explicit third-order large stability domain Runge-Kutta method, called DUMKA ([93, 94]) presented in Section 1.2.4.

2.3 Numerical Experiments

In this section we present results of numerical experiments performed on the one-dimensional single-gas laser ablation problem. The process of growing thin films using a nanosecond pulse of a focused laser beam involves the ablation, or evaporation, of the target material and its subsequent deposit onto the substrate. The ablation of the target material results in the formation of a plasma which is a very complex process involving a Coulomb explosion [22, 6], where the solid's bonds are broken by the atomic motion caused by the excitation energy delivered by the laser resulting in a dynamic plasma bunch. The charged atomic particles of the plasma expand on to the substrate surface. The applied problem modeled here attempts to describe the dynamics of this expansion using the quasi-gas dynamic (QGD) equations. It should be noted here that the dynamics under investigation take place upon the substrate. The one-dimensional model describes the density, pressure and velocity of the expansion in the direction parallel to the surface of the substrate. This is in contrast to laser experiments that measure drilling depth, e.g. [32], where the one-dimensional problem measures distance orthogonal to the surface.

The use of fluid dynamic equations to model thin film growth is supported by [23, 72]. Since the expansion takes place in a low pressure setting, and the quality of the thin film depends on the deposition rate, it is important to avoid shock formations since they negatively impact the quality of the thin film [36, 72]. The physiochemical processes that lead to shock waves are difficult to measure in physical experiments. Thus, a computer simulation of the process which is able to lend light to the factors that lead to the generation of shock waves is very much desirable.

In the single-gas experiment we model the plasma expansion as a carbon-jet expanding into a vacuum. This is represented by an extremely large high-pressure, high-temperature front that expands into a low-pressure, low-temperature atmosphere meant to model a vacuum. This is known as relaxation after explosion [72]. The set up of the problem is very much akin to shock tube or dam-break problems. The fluid dynamic equation used to model the expansion are systems of nonlinear hyperbolic conservation laws. Of course, there are numerical difficulties that arise in the numerical approximation of these equations. In fact, the shock tube problem is a tool used to test the accuracy of numerical methods, [110], since the solution to, e.g., the shock tube problem evolved by Euler's equations of gas dynamics, involves a rarefaction wave, contact discontinuity, and shock wave.

In [72, 36], the numerical method employed is a basic finite difference scheme. A com-

mon hinderance of finite difference schemes is the appearance of spurious oscillations behind a discontinuity in the solution. Furthermore, stability constraints on the forward Euler scheme require $\Delta t \sim (\Delta x)^2$.

To solve the one-dimensional laser ablation problem in [72, 36], a standard second-order central difference, (1.113), is used to approximate the spatial derivatives and forward Euler, (1.111), is used to approximate the time derivatives. The computer simulation is carried out on a rectangular mesh, $X \times T$, where $X = \{x_i : i = 0 \dots N_x - 1, x_i = x_0 + i\Delta x, x_0 = -\Delta x/2\}$ and $T = \{t_j : j = 0 \dots N_t - 1, t_j = t_0 + j\Delta t, t_0 = 0\}$. Here we have N_x and N_t indicating the number of internal nodes for the spatial and temporal discretizations. In order to resolve a solution, the mesh parameters are set at $\Delta x = 0.45 \times 10^{-6}$ ($N_x = 45000$), which prescribes $\Delta t = 2 \times 10^{-13}$ ($N_t = 2 \times 10^7$). In difference form, the boundary conditions are taken as (2.43).

In the following, we are able to decrease the magnitude of the spatial discretization by an order of magnitude and, by applying efficient numerical integrators, greatly reduce the computation time. The savings achieved in the numerical computation of the plasma expansion due to laser ablation problem allow for the simulation of the numerical experiments necessary to gain insight into the factors leading to shock formation.

The choice of which model to use in the simulation of laser ablation is nuanced and depends on, among other things, the balance between accuracy and efficiency demanded by the researcher. The full Navier-Stokes simulation provides highly accurate results at high computational cost, due to the numerical stability constraints imposed by the stiffness of the problem. It is noted that heretofore the full Navier-Stokes simulation of laser ablation had not been performed.

The QGD simulations provide an excellent, albeit smoothed, approximation of the Navier-Stokes equations at fantastic computational efficiency. The relaxation parameter can either be a function of the solution (2.44) or held constant. As previously noted, as $\tau \to 0$, the QGD model approaches Navier-Stokes. We provide results describing this behavior. In fact, the computational savings are substantial for both cases, while providing an extremely accurate representation of the Navier-Stokes results.

In all the numerical experiments below, the spatial discretization is achieved by applying the central-upwind scheme [66] presented in Chapter 1. The choice in time discretization methods requires special care in realizing desired objectives. The SSP Runge-Kutta method proves to be the best choice for the single-gas QGD problems. Note, for all experiments, computation was carried out on a MacPro with 2 Quadcore Intel Xeon processors with 2.66 GHz processor speed and 8 GB of RAM. In addition to allowing us to manipulate the relaxation parameter and limiting the slope in the reconstruction steps, the method also allows us to choose the CFL number to control the numerical stability and ensure that the oscillations that occur near zero stay positive. In this way, we are able to produce desirably accurate results with a cost-

effective, positivity-preserving method. However, the SSP Runge-Kutta method is less effective in computing the full Navier-Stokes simulation. The CFL number here becomes prohibitively small. In this case, we apply the DUMKA time-stepping method. This method provides a carefully chosen, varying time-step in order to maintain stability while efficiently solving the problem.

Single Gas

Under consideration is the spread of the plasma of molecular carbon C_2 in a vacuum. Carbon has constant parameters $R = 346.25$, $\gamma = 7/5$, $\omega = 0.74$, $Pr = 14/19$ and $Sc = 0.746$. We consider the system (2.13) - (2.15) subject to the initial conditions,

$$(p(x,0), T(x,0), u(x,0)) = \begin{cases} (p^{(1)}, T^{(1)}, 0), & \text{if } x \leq 5 \times 10^{-6} \text{ m}, \\ (p^{(2)}, T^{(2)}, 0), & \text{if } x > 5 \times 10^{-6} \text{ m}. \end{cases} \tag{2.42}$$

The boundaries of the domain are taken to be solid walls. The boundary conditions are taken to be $u = 0$, $\frac{\partial \rho}{\partial x} = 0$, and $\frac{\partial T}{\partial x} = 0$. It is noted that more sophisticated moving interface methods exist, see [80].

The calculation domain is taken to be $0 \leq x \leq L = 0.02$ m. After the laser pulse, at $t = 0$, there is a thin region, $x \leq l = 5 \times 10^{-6}$, where the gas achieves high-pressure and high-temperature while the rest of the domain is at low-pressure and low-temperature. The time of integration is taken to be $0 \leq t \leq t_f = 4\mu s$. The conservative variables ρ, ρu, and E at $t = 0$ are found using (1.37) and (2.18) and noting that $\rho u = 0$ over the entire domain initially since $u = 0$ initially. The boundary conditions are implemented numerically as follows,

$$\begin{aligned} &\bar{\rho}_0 = \bar{\rho}_1, \quad \bar{u}_0 = -\bar{u}_1, \quad \bar{p}_0 = \bar{p}_1, \\ &\bar{\rho}_{N-1} = \bar{\rho}_{N-2}, \quad \bar{u}_{N-1} = -\bar{u}_{N-2}, \quad \bar{p}_{N-1} = \bar{p}_{N-2}, \end{aligned} \tag{2.43}$$

where, e.g. $\bar{\rho}$, denotes the cell average of the given quantity and N is the grid size.

Example I verifies the ability of the scheme to qualitatively capture the dynamics of the expansion using a coarser grid. Furthermore, we perform a grid refinement study which shows convergence of the solutions. We also present an analysis of the relaxation parameter τ, which is calculated, according to [72], by the formula

$$\tau = \frac{\alpha \Delta x}{Sc \cdot c}. \tag{2.44}$$

Note that in this formulation, τ is proportional to the spatial step size and c, the speed of sound in the gas, which itself is a function of the solution at each grid point. In [72], $\alpha = 0.6$. In fact, this parameter may be chosen to facilitate numerical stability. As previously mentioned, the

QGD equations tend to the NS equations as $\tau \to 0$. With this in mind, we seek to minmize the effect of τ in order to achieve a closer representation of a NS simulation. However, as is expected in the full NS simulation, numerical stability becomes an issue and thus we must balance our desire to run the full NS simulation with the desire to have a stable and efficient method, especially keeping in mind our goal of expanding the numerical scheme to a two-dimensional model. In this spirit we analyze the relaxation parameter and show that it may also be chosen independent of the solution. Results obtained using a constant value for the parameter τ are compared with results from the full Navier-Stokes simulation.

We also demonstrate the ability to run simulations with more physically accurate initial conditions. To match the physical experiments, the pressure in the strike zone must be increased by orders of magnitude. In [72], in order to resolve a solution, this increase in pressure in the strike zone demanded an undesirable increase in the pressure of the surrounding atmosphere.

Example II provides results that match this experiment. To more realistically model the physical experiment we want to minimize the pressure in the surrounding atmosphere which, in the single-gas model, is meant to mimic a vacuum. In Example III, we show the ability to implement significantly lower pressure in this region, thus obtaining a more physically appropriate representation of the physical experiments. Example IV provides results for the variation of the size of the strike zone. Finally, Example V provides details for the Navier-Stokes simulation and a summary of the three models.

2.3.1 Example I

In this section we review results obtained computing the solution to the single-gas laser ablation problem with the initial conditions given by (2.42) with,

$$\begin{aligned} &p^{(1)} = 10^8 \text{ Pa}, \quad p^{(2)} = 3 \text{ Pa}, \\ &T^{(1)} = 3 \times 10^4 \text{ K}, \quad T^{(2)} = 300 \text{ K}, \end{aligned} \tag{2.45}$$

and boundary conditions given by (2.43). These initial conditions coincide with 'Case **B**' in [72].

The solutions to the laser ablation problem are first computed using the full QGD model. The results computed using three spatial cell sizes are provided, namely $\Delta x = 4 \times 10^{-6}$ m, $\Delta x = 2 \times 10^{-6}$ m and $\Delta x = 4.44 \times 10^{-7}$ m. The plots are of the normalized density versus time at specified locations along the spatial domain, namely $x = 5\ mm$ and $x = 11\ mm$. In other words, the plot gives the view of the plasma expansion for someone standing at the indicated distance from the laser strike as time evolves. The density is normalized by $\rho \times 10^4/\rho^{(1)}$, with $\rho^{(1)} = p^{(1)}/(T^{(1)}R)$. Note, this normalization procedure is carried out on all results in this section. The data for these time plots are sampled at 100 equally spaced points along the time

domain. As noted above, the results presented here for the QGD simulations are obtained using the SSP RK time integrator. In general, the goal is to minimize the quasi-gas dynamics diffusion, which is controlled by the relaxation parameter, while also minimizing the smoothing performed via θ in the minmod function (1.69). The relaxation parameter is calculated via (2.44), where α is chosen as small possible. Note that as α decreases the numerical stability issues present in the full Navier-Stokes simulation become more dominant. This results in necessarily decreasing the CFL number, which of course increases computation time. Table 2.1 shows the interplay between these parameters. The constants c_1 and c_2 control the convective and diffusive CFL constraints, respectively. I.e.,

$$\Delta t = \min\left(c_1\left(\frac{\Delta x}{a_{\max}}\right), c_2(\Delta x)^2\right) \tag{2.46}$$

Note that $a_{\max}$ is the largest in modulus of the left and right local speeds calculated in (2.36). Table 2.1 shows the effects on computational time due to the adjustment of these parameters.

Table 2.1: QGD Computational Parameters

	θ	α	c_1	c_2	Run Time
1	1.3	0.6	0.45	0.5	34m 52.381s
2	1.55	0.6	0.45	0.5	34m 22.113s
3	1.55	0.6	0.45	1.0	17m 16.509s
4	1.55	0.6	0.45	1.65	10m 36.695s
5	1.55	0.275	0.45	1.65	10m 44.895s

We see that c_2, the parameter controlling the CFL number associated with diffusion has a great impact on run time. Furthermore, we see that decreasing α, which provides sharper resolution of the frontal shock, has a small effect on the run time. See Figure 2.5 to observe the smoothing that occurs with larger values of α. The parameters that we chose to run the following QGD simulations with are

$$\theta = 1.55,\ \alpha = 0.275,\ c_1 = 0.45,\ c_2 = 1.65. \tag{2.47}$$

Table 2.1 is by no means an exhaustive list, but is meant to give the reader insight into the effects of these parameters so that the numerical scheme may be tuned to specific needs.

Figure 2.1 presents results obtained using spatial cell size $\Delta x = 4 \times 10^{-6}$ m. The results capture the qualitative behavior including the shock front formation present at $x = 11\ mm$.

This step is the shock wave that under certain conditions may appear in front of the main flux. The conditions leading to the appearance of this laser jet front are important since the shocks are detrimental to the quality of the thin film produced by the spread of the plasma over the substrate.

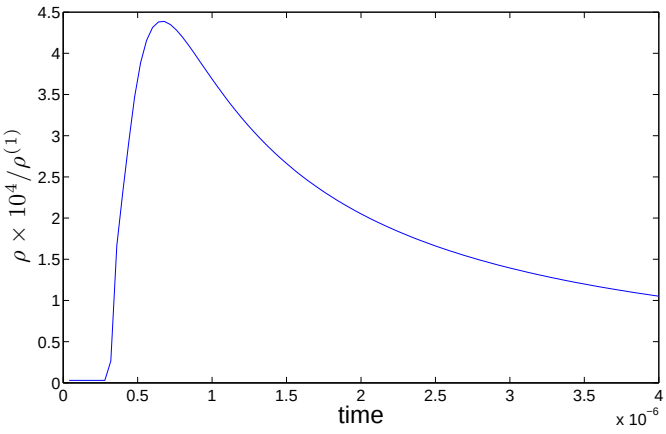

(a) $x = 5mm$

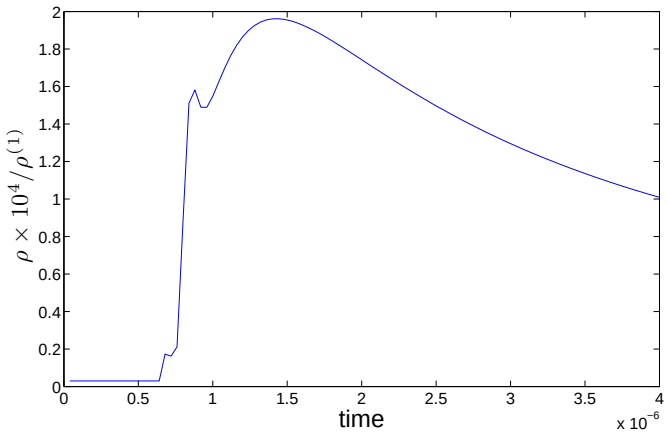

(b) $x = 11mm$

Figure 2.1: **Example I** Solution (normalized density) plotted against time at the indicated distance from the strike zone, computed on grid with $\Delta x = 4 \times 10^{-6}$ m.

In Figure 2.2, we supply results for mesh size $\Delta x = 2 \times 10^{-6}$ m. The density is less than what is obtained with $\Delta x = 4 \times 10^{-6}$ m, which is consistent with the non-monotonic convergence as the cell size decreases, see Figure 2.4.

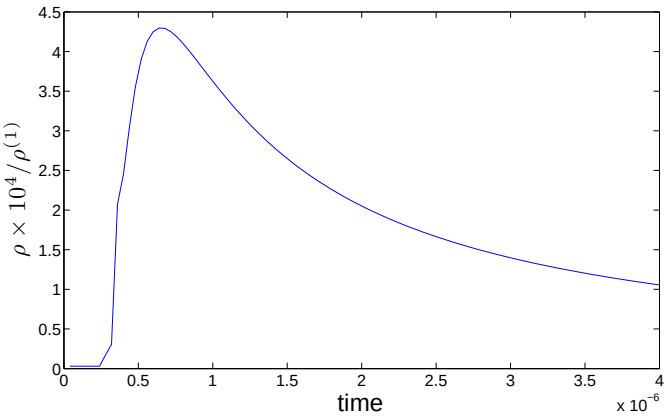

(a) $x = 5mm$

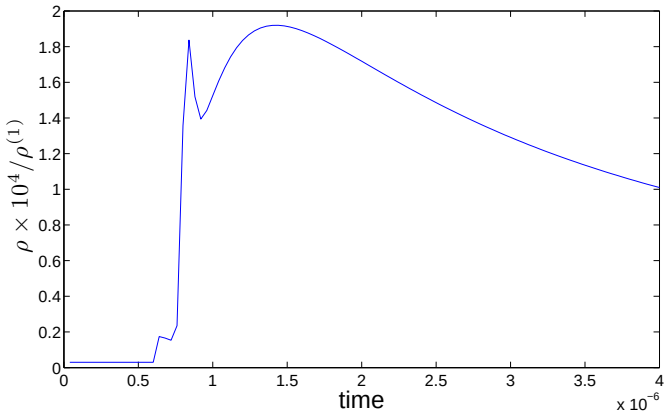

(b) $x = 11mm$

Figure 2.2: **Example I** Solution (normalized density) plotted against time at the indicated distance from the strike zone, computed on grid with $\Delta x = 2 \times 10^{-6}$ m.

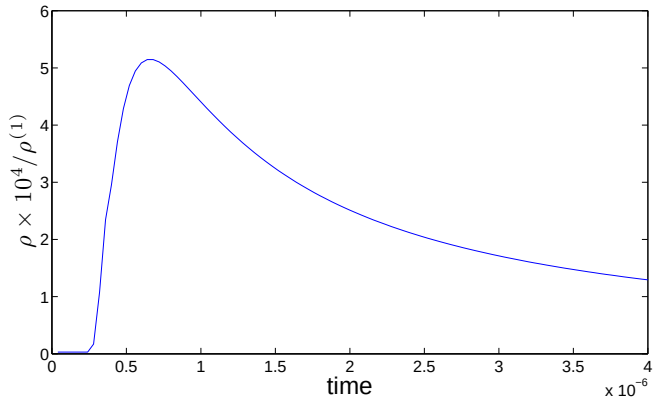

(a) $x = 5mm$

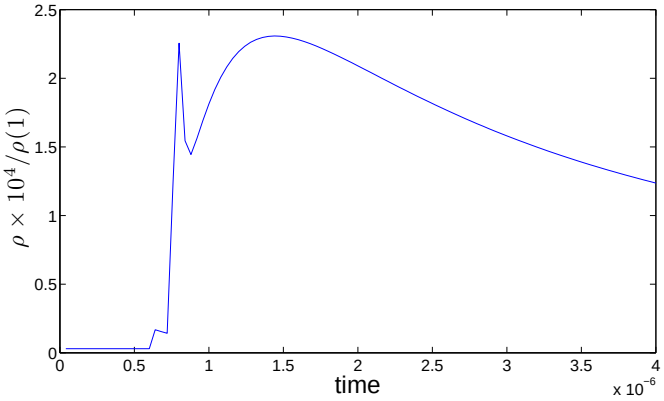

(b) $x = 11mm$

Figure 2.3: **Example I** Solution (normalized density) plotted against time at the indicated distance from the strike zone, computed on grid with $\Delta x = 4.44 \times 10^{-7}$ m.

Figure 2.3 provides a reference solution using $\Delta x = 4.44 \times 10^{-7}$ m. The amplitude of these plots exceed those in [72], pointing to less numerical dissipation. The step character in the results model the shock wave that appears in front of the jet and is to be expected. The increasing resolution of the spike in these plots indicate an increasingly better approximation of the laser jet front.

The results obtained in [72] were computed using a standard second-order central difference method to approximate the spatial derivatives and first-order forward differences for the time derivatives. The finite difference scheme requires a cell size of $\Delta x = 4.44 \times 10^{-7}$ m. In addition, the forward Euler time integrator requires a time step on the order of $(\Delta x)^2$.

The central-upwind scheme applied here is able to resolve a solution with a much larger cell size. In fact, we are able to resolve solutions with $\Delta x = 9.995 \times 10^{-6}$ m. This decrease in spatial grid points of over ninety percent, coupled with the use of an efficient ODE solver to integrate the semi-discrete scheme, provides substantial computational savings.

Figure 2.4 provides a plot of the convergence of the scheme to the solution given in [72].

Relaxation Parameter Analysis As previously mentioned, the relaxation parameter τ is tied to the solution. In particular, at each time step, τ must be calculated using updated values of pressure and density. We want to analyze the effect this parameter has on solutions and ascertain if it could be decoupled from the solution.

First, we present results of the numerical experiments where the magnitude of τ is progressively decreased through the manipulation of the constant α in (2.44). Figure 2.5 provides plots of normalized density versus time at $x = 11\ mm$ as α decreases. The results are obtained using the cell size $\Delta x = 4 \times 10^{-6}$ m and the computational parameters given in (2.47), save the varying values for α. The initial conditions are given in (2.45). As can be seen, the shock front becomes more sharply resolved as α decreases, in accordance with what is expected regarding the smoothing effect of the relaxation parameter. Secondly, we conduct experiments implementing a constant value for τ. Analysis of the values taken on by τ during the QGD simulation provides approximate bounds. It was found that $3.047 \times 10^{-10} \leq \tau \leq 9.98 \times 10^{-9}$. The constant τ experiments were conducted using the initial conditions given in (2.45) and a spatial cell size $\Delta x = 4 \times 10^{-6}$ m. The computational parameters must be chosen carefully to compute a solution when τ is held constant.

Both the minmod parameter and the CFL constraint for diffusion must both be set at lower values to compute solutions in these experiments. We were unable to compute solutions for $\theta = 1.55$, the value used in the previous QGD experiments, with the CFL condition kept at an appropriate level for efficient computation. In this experiment we chose to hold $\theta = 1.3$ and $c_1 = 0.45$. The value for c_2, the CFL constraint on diffusion, must be chosen corresponding to the value the constant τ is set.

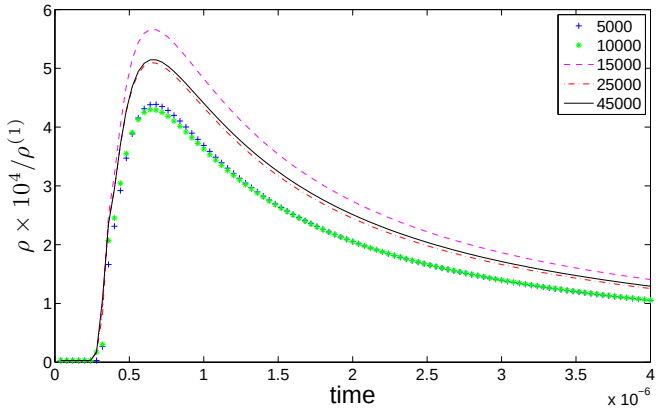

(a) $x = 5mm$

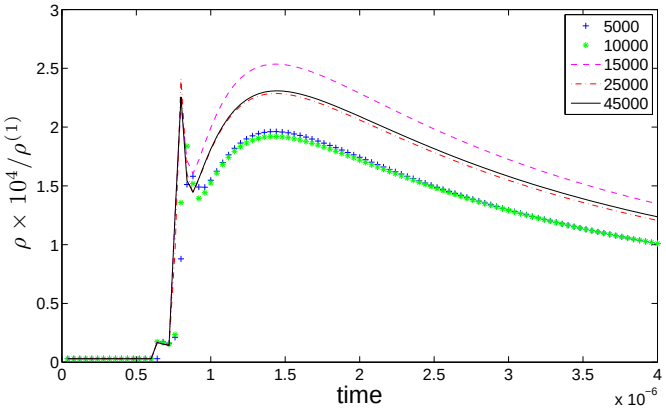

(b) $x = 11mm$

Figure 2.4: **Example I** Convergence of the solution (normalized density) plotted against time at the indicated distance from the strike zone. Computed on grid with Δx inversely proportional to the indicated number of grid points.

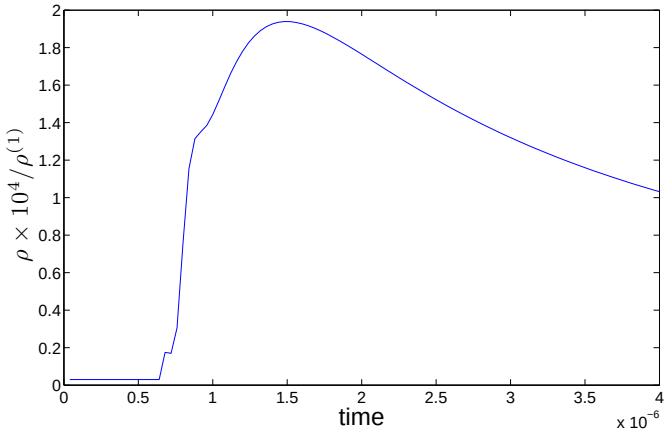

(a) $\tau \sim 0.6$

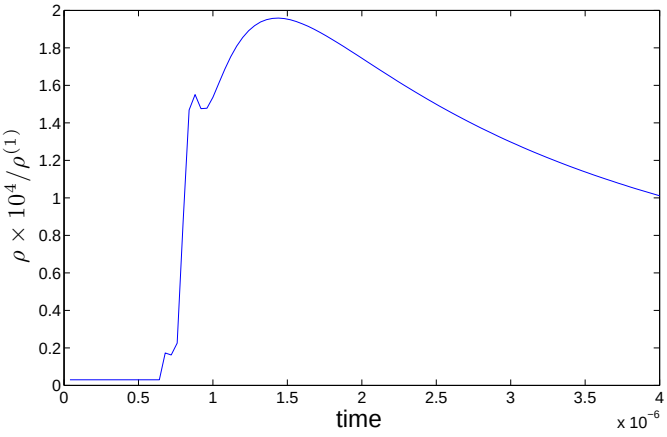

(b) $\tau \sim 0.3$

Figure 2.5: **Example I** Smoothing of the solution diminishes as relaxation parameter τ decreases. Solution (normalized density) is plotted against time at a distance $x = 11mm$ from the strike zone for the indicated parameter, computed on grid with $\Delta x = 4 \times 10^{-6}$ m.

With regards to the balance of efficiency and accuracy, we found $\tau = 10^{-9}$ to be an ideal choice for the parameter. The resolution of the solution is favorable and comparable to our previous results. For this simulation we were able to compute results using $c_2 = 0.5$. The run time for this simulation is 33 m 12.849 s. Note that this is significantly longer than the QGD simulation.

We were also able to obtain a result for $\tau = 10^{-8}$. This result is of course smoothed in comparison, due to the larger amount of diffusion being allowed by the relaxation parameter. However, to produce results here we need to lower $c_2 = 0.2$ which results in a run time of 83 m 14.245 s. This is of course less than ideal, both in efficiency and accuracy. The plots for these two experiments are compared in Figures 2.6 and 2.7, for $x = 5\ mm$ and $x = 11\ mm$ respectively. Note the increased resolution of the shock front in Figure 2.7, which is expected with the smaller amount of diffusion.

Finally, we attempted to obtain results for $\tau = 10^{-10}$. Using the RK time integration requires an extremely small CFL number to resolve the solution, which results in an unacceptable run time. Using the DUMKA time-stepping procedure produces results in a relatively efficient manner. In fact, the procedure produces results for $\tau = 10^{-10}$ at a run time of 37 m 21.505 s. These results are plotted in Figure 2.8. Note the extreme resolution of the shock fronts visible in both plots. This is consistent with the NS results, see Figures 2.13(c) and 2.14(d), and agree with the expected effect of decreasing τ. Note, however, the unsteady resolution due to the increasing numerical instability.

So, we see that the full QGD simulation provides an acceptable approximation to the full Navier-Stokes simulation at an extreme computational saving, approximately ten minutes versus nearly 38 hours for the full Navier-Stokes simulation. Decoupling the relaxation parameter from the solution and making it constant is able to provide results that approach more closely the Navier-Stokes simulation, with only a slight loss of computational efficiency. A summary of the three models is provided in Section 4.5.

2.3.2 Example II

In order to accurately model the physical experiments, the pressure in the strike zone is increased by an order of magnitude. However, this places increased strain on numerical methods. In [72], to resolve a solution, the increase in pressure in the strike zone demanded an increase in $p^{(2)}$. In this example we review results obtained computing the solution to the laser ablation problem with the initial conditions given by (2.42) with,

$$\begin{aligned} p^{(1)} &= 10^{10}\ \text{Pa}, \quad p^{(2)} = 10^{3}\ \text{Pa}, \\ T^{(1)} &= 10^{4}\ \text{K}, \quad T^{(2)} = 300\ \text{K}. \end{aligned} \tag{2.48}$$

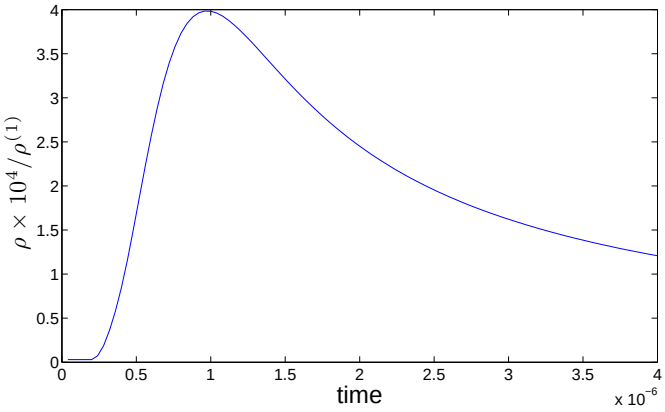

(a) $\tau = 10^{-8}$

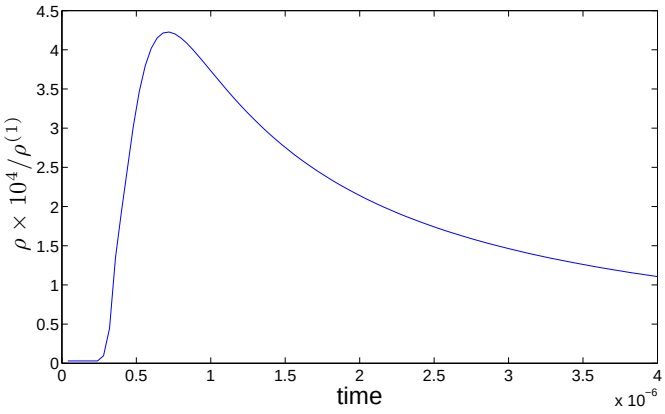

(b) $\tau = 10^{-9}$

Figure 2.6: **Example I** Constant τ solutions (normalized density) plotted against time at a distance $x = 5mm$ from the strike zone, computed on grid with $\Delta x = 4 \times 10^{-6}$ m.

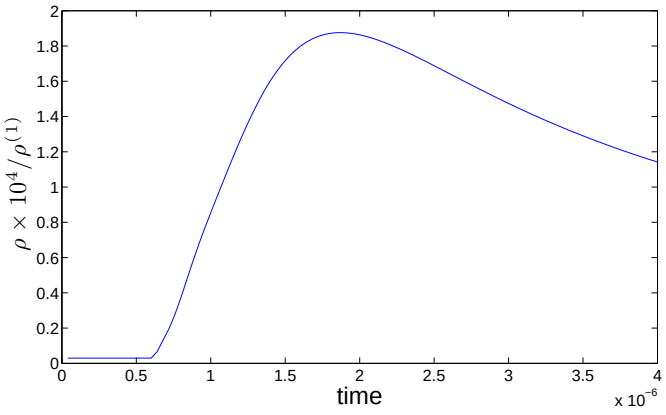

(a) $\tau = 10^{-8}$

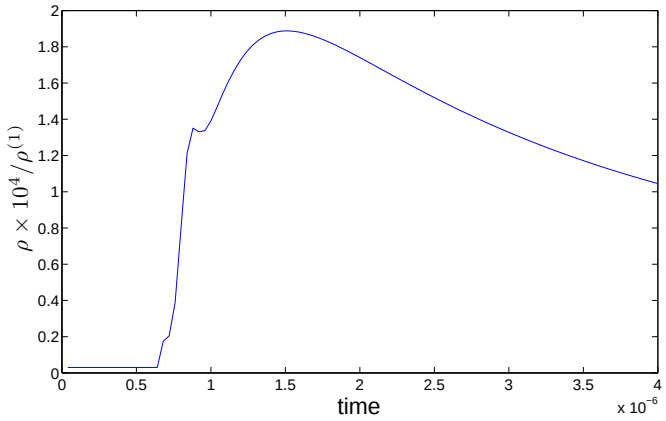

(b) $\tau = 10^{-9}$

Figure 2.7: **Example I** Constant τ solutions (normalized density) plotted against time at a distance $x = 11mm$ from the strike zone, computed on grid with $\Delta x = 4 \times 10^{-6}$ m.

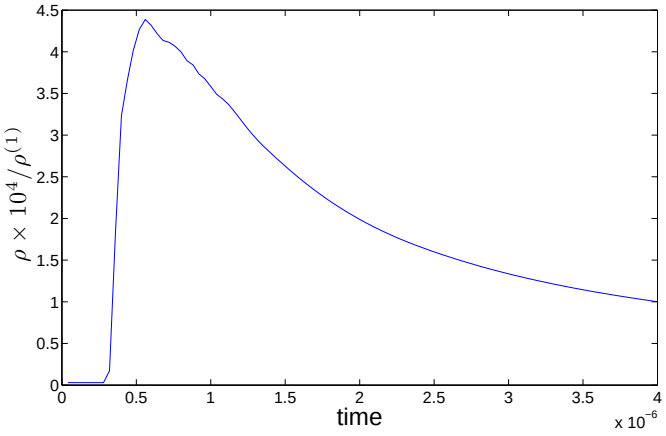

(a) $x = 5mm$

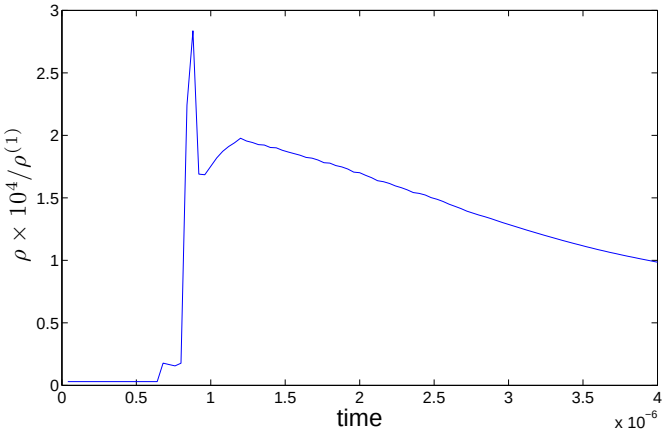

(b) $x = 11mm$

Figure 2.8: **Example I** Constant $\tau = 10^{-10}$ solutions (normalized density) plotted against time at the indicated distance from the strike zone, computed on grid with $\Delta x = 4 \times 10^{-6}$ m using DUMKA ODE solver.

and boundary conditions given by (2.43). These initial conditions coincide with 'Case **D**' in [72]. This experiment is actually a 'preliminary' result on the way to the more realistic initial conditions implemented in the next example. In this experiment the pressure of the carbon gas in the strike zone and in the 'vacuum' atmosphere are increased. Figure 2.9 provides plots of the results computed using a cell size of $\Delta x = 4 \times 10^{-6}$ m.

Notice the visible lag in the appearance of the shock front at $x = 11\ mm$, Figure 4.2.9(b). This is the effect of the high pressure atmosphere slowing down the expansion.

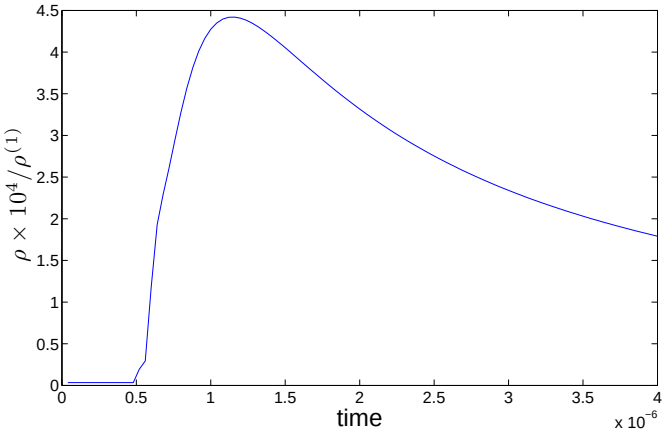

(a) $x = 5mm$

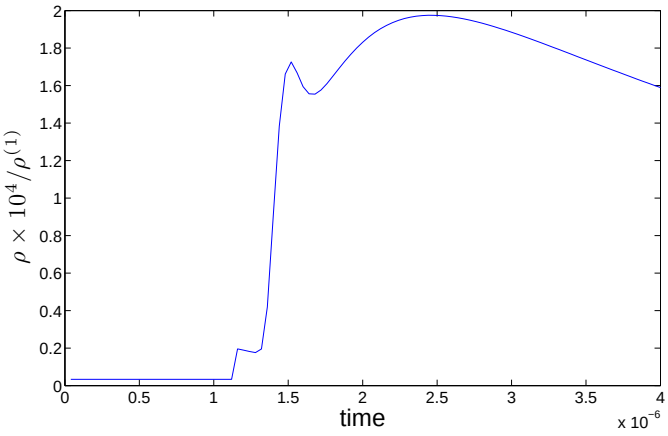

(b) $x = 11mm$

Figure 2.9: **Example II** Solution (normalized density) plotted against time at the indicated distance from the strike zone, computed on grid with $\Delta x = 4 \times 10^{-6}$ m.

2.3.3 Example III - More Physically Realistic Initial Conditions

In this example we implement more physically appropriate initial conditions. In particular, we would like a better representation of the vacuum into which the plasma expands when $p^{(1)}$ is increased to a experimentally desired magnitude. The pressure $p^{(2)}$, in the atmosphere, should be set as low as possible to more realistically model the physical experiment. The scheme implemented here is able to produce results when $p^{(2)} \sim \mathcal{O}(1)$. Again, we consider the laser ablation problem with the initial conditions given by (2.42) with

$$\begin{aligned} p^{(1)} &= 10^{10} \text{ Pa}, \quad p^{(2)} = 3 \text{ Pa}, \\ T^{(1)} &= 10^4 \text{ K}, \quad T^{(2)} = 300 \text{ K}, \end{aligned} \tag{2.49}$$

and boundary conditions given by (2.43).

The results provided in Figure 2.10 demonstrate the ability of the numerical scheme to compute a solution to this demanding problem. We see that the shock front is smoothed away in this experiment. It is again noted that these results were computed with a spatial cell size of $\Delta x = 4 \times 10^{-6}$ m, and that they have not been previously obtained.

2.3.4 Example IV - Strike Zone

Next, we vary the size of the strike region to observe the effect on the solution. In particular, we want to see how this affects the pre-shock visibile in the previously obtained plots of the density at a distance $x = 11$ mm from the target. It should be noted that as the initial strike region becomes smaller, the mesh size must increase in order to have a grid fine enough to capture $p^{(1)}$ in at least one cell. I.e., $x_1 = \frac{1}{2}\Delta x \leq l$. Thus, the mesh size $N \geq \frac{L}{2l}$.

We consider the laser ablation problem with initial conditions given by (2.42) and boundary conditions given by (2.43). The initial values of pressure and temperature are taken from the first example. I.e.,

$$\begin{aligned} p^{(1)} &= 10^8 \text{ Pa}, \quad p^{(2)} = 3 \text{ Pa}, \\ T^{(1)} &= 3 \times 10^4 \text{ K}, \quad T^{(2)} = 300 \text{ K}. \end{aligned} \tag{2.50}$$

In this experiment, first we decrease the strike region to $x \leq l = 2 \times 10^{-6}$ m. Figure 2.11 provides the results. To resolve the solution in this case, the cell size must be decreased to $\Delta x = 2 \times 10^{-6}$ m, which is the value used here. Next we increase the strike region to $x \leq l = 7.5 \times 10^{-6}$ m. The result for this case is provided in Figure 2.12. Notice that decreasing the size of the strike zone has little effect on the plots. However, increasing the strike zone noticeably affects the solution. The increased volume of high pressure and temperature results

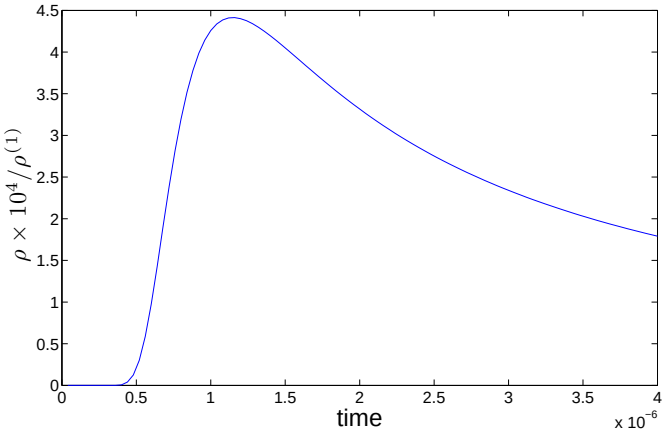

(a) $x = 5mm$

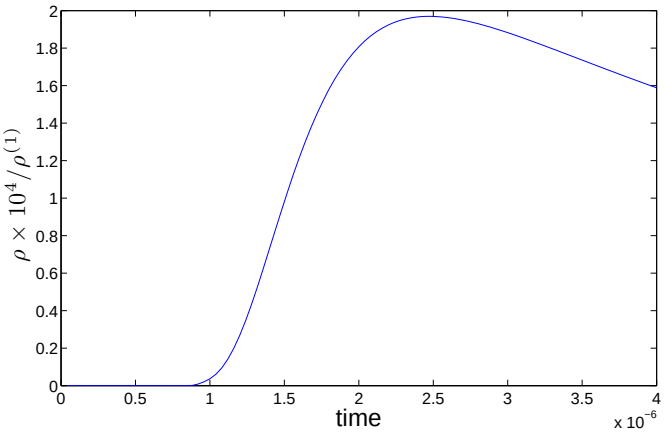

(b) $x = 11mm$

Figure 2.10: **Example III** Solution (normalized density) plotted against time at the indicated distance from the strike zone, computed on grid with $\Delta x = 4 \times 10^{-6}$ m.

in a higher density expansion.

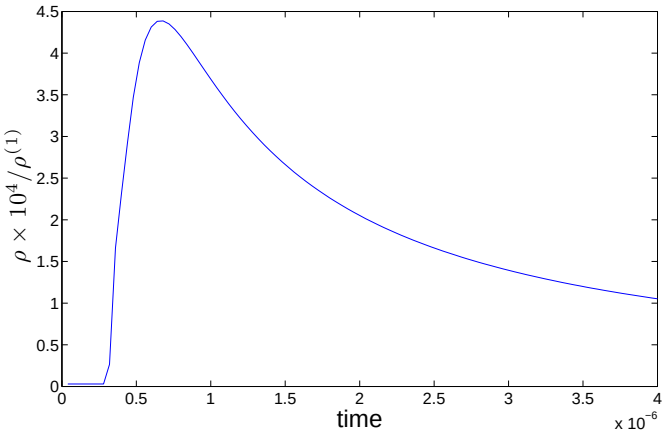

(a) $x = 5mm$

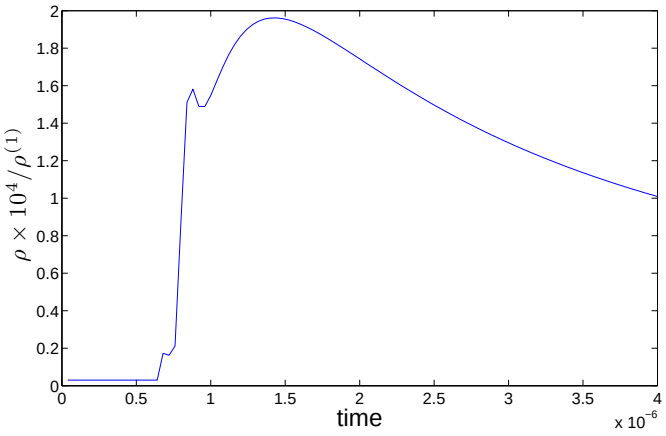

(b) $x = 11mm$

Figure 2.11: **Example IV** Decrease the size of the strike zone: $l = 2\mu m$. Solution (normalized density) plotted against time at the indicated distance from the strike zone, computed on grid with $\Delta x = 2 \times 10^{-6}$ m.

2.3.5 Example V - Navier-Stokes Model

In this section we present results obtained by applying the Navier-Stokes model to the laser ablation problem and compare the results of the three different models applied to the single-gas problem. These models are given below.

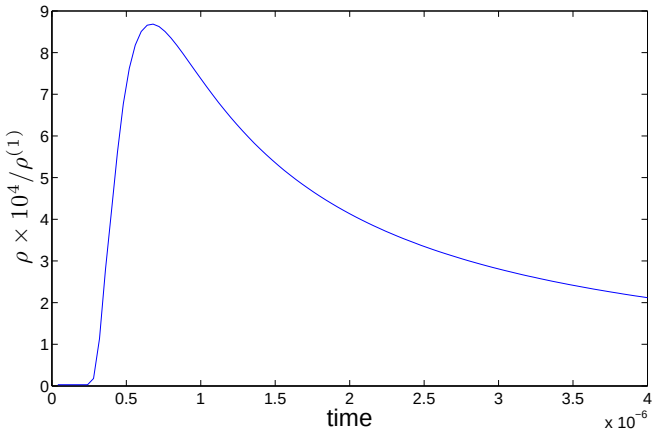

(a) $x = 5mm$

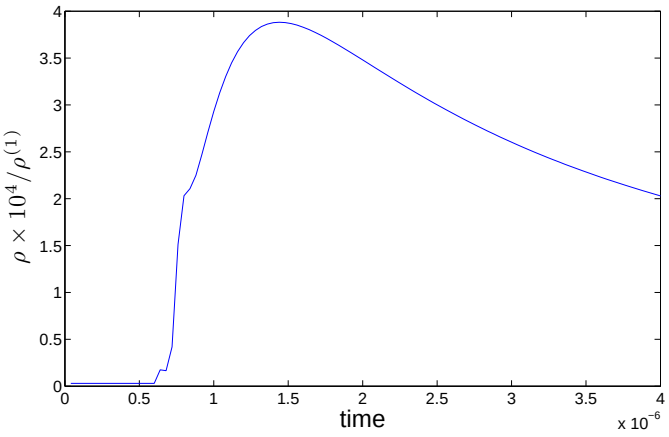

(b) $x = 11mm$

Figure 2.12: **Example IV** Increase the size of the strike zone: $l = 7.5\mu m$. Solution (normalized density) plotted against time at the indicated distance from the strike zone, computed on grid with $\Delta x = 4 \times 10^{-6}$ m.

1. Quasi-Gas Dynamics: τ is dependent on solution at each step.

2. Constant τ: τ is a constant parameter.

3. Navier-Stokes.

Recall that the relaxation parameter τ is used to provide computational stability by adding numerical dissipation. With τ eliminated from the QGD equations, i.e. the Navier-Stokes equations, resolving the solution with the given initial conditions becomes more challenging. One of the main goals of this project is to resolve the solution to the Navier-Stokes equations with the initial conditions given by the laser ablation problem, which had previously not been accomplished. The scheme implemented here is able to resolve a solution for this problem, accurately resolving shocks with a cost efficient mesh size.

Recall, the dynamic viscosity in the QGD equations is computed proportional to τ. For the Navier-Stokes equations, the dynamic viscosity η is computed via equation (2.28). The standard conditions for carbon are given by $T^* = 300$ K and $\eta^* = 1.66 \times 10^{-5}$ kg/ms. The simulations are run with a spatial mesh width given by $\Delta x = 4 \times 10^{-6}$ m. The initial conditions for the problem are given in (2.51).

$$\begin{aligned} p_1 &= 10^8 \text{ pa}, \quad T_1 = 3 \times 10^4 \text{ K}, \\ p_2 &= 3 \text{ pa}, \quad T_2 = 300 \text{ K}. \end{aligned} \tag{2.51}$$

The DUMKA time-stepping procedure is used to compute the Navier-Stokes solution to the problem. Due to stiffness of the problem and the numerical stability issues presented by Navier-Stokes' equations, $\theta = 1.0$ is the only value for this parameter that provides enough smoothing to produce a solution. It is obvious that the QGD equations provide a much more reasonable approach to obtaining approximations to the laser ablation problem.

Figures 2.13 and 2.14 provide results, at $x = 5$ mm and $x = 11$ mm respectively, comparing the solutions obtained using the three models. We see that the results provided by the constant τ simulation and by the QGD simulation provide a nice resolution of the shock front at $x = 11$ mm. Although neither match the sharp resolution of the expansion as well as the Navier-Stokes simulation, the computational savings in these approximations lead us to determine that the QGD method is the most effective model in approximating the plasma expansion.

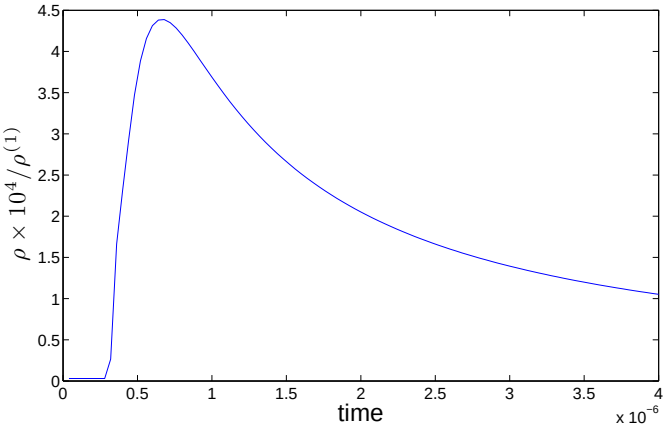

(a) QGD

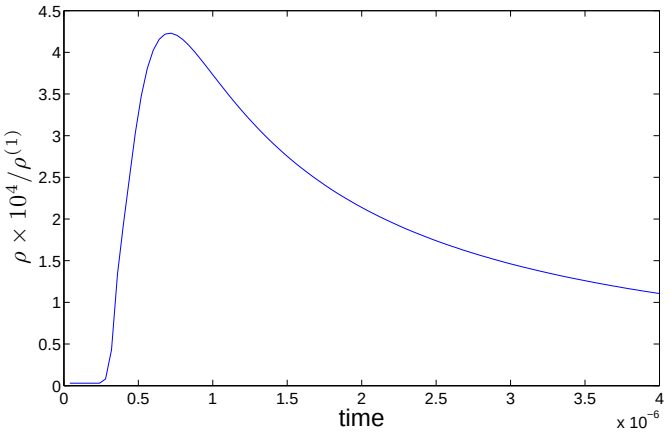

(b) $\tau = 10^{-9}$

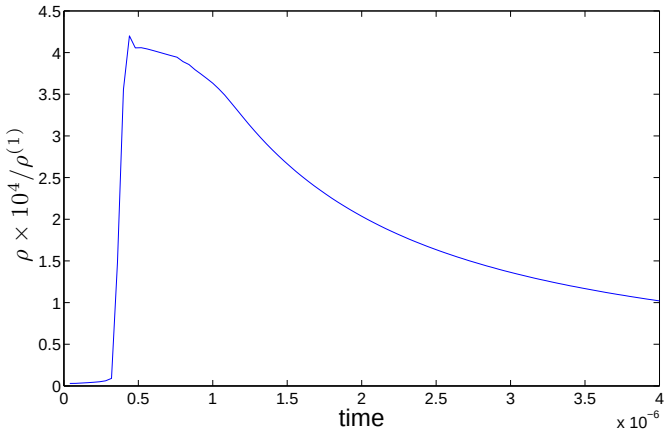

(c) NS

Figure 2.13: **Example V** Comparison of three single-gas models. Solution (normalized density) is plotted against time at a distance $x = 5mm$ from the strike zone, computed on grid with $\Delta x = 4 \times 10^{-6}$ m.

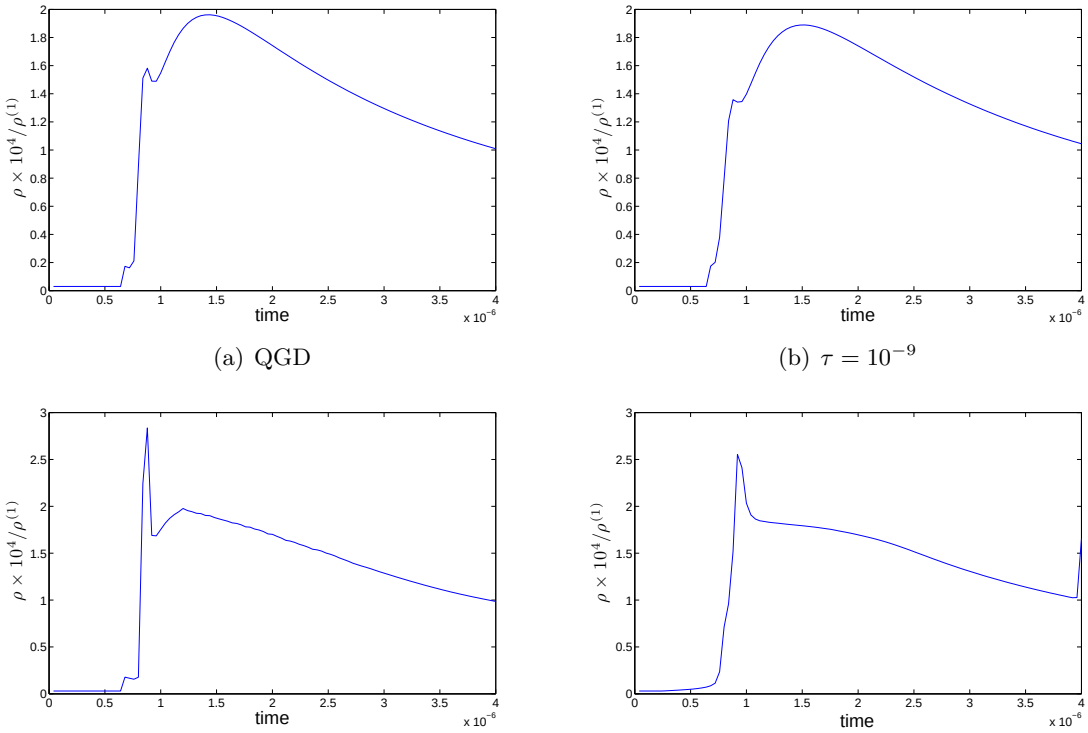

(a) QGD (b) $\tau = 10^{-9}$

(c) $\tau = 10^{-10}$ (d) NS

Figure 2.14: **Example V** Comparison of three single-gas models. Solution (normalized density) is plotted against time at a distance $x = 11mm$ from the strike zone, computed on grid with $\Delta x = 4 \times 10^{-6}$ m.

Chapter 3

One-Dimensional Laser Ablation - Binary Gas

3.1 Mathematical Model

More realistically, ablation occurs in a low-pressure gaseous medium. The expanding laser plasma is more accurately modeled by describing the binary gas mixture in order to analyze the interaction of shock waves emerging during the expansion of the laser jet. This analysis allows one to determine the minimum pressure at which the buffer gas begins to adversely affect the the expansion of the carbon flow. In practical applications it is desirable to determine the conditions under which the velocity of the carbon flow is approximately equal to the velocity of the shock wave in the buffer gas. Drift in the location of shocks is common in the computation of this system. The numerical scheme employed here is able to accurately resolve the location of the shocks. In the following we consider the expansion of a carbon laser jet in a domain filled with low-pressure nitrogen.

The dynamics of interaction between two different gases is considered using the quasi-gas dynamic system of equations for a binary gas mixture [35]. Each component a and b of the gas are described by three functions of the Eulerian coordinate x and time t. We have $\rho_a(x,t)$ - gas density, $u_a(x,t)$ - macroscopic velocity, and $p_a(x,t)$ - pressure of gas a, with analogous descriptions for gas b. The equations for each gas are derived similarly to the single-

gas equations, (2.13)-(2.16), and are given by

$$\frac{\partial \rho_a}{\partial t} + \frac{\partial j_a}{\partial x} = 0, \tag{3.1}$$

$$\frac{\partial (\rho_a u_a)}{\partial t} + \frac{\partial (j_a u_a)}{\partial x} + \frac{\partial p_a}{\partial x} = \frac{\partial \Pi_a}{\partial x} + S_a^u, \tag{3.2}$$

$$\frac{\partial E_a}{\partial t} + \frac{\partial (j_a H_a)}{\partial x} + \frac{\partial q_a}{\partial x} = \frac{\partial \Pi_a u_a}{\partial x} + S_a^E, \tag{3.3}$$

$$j_a = \rho_a (u_a - w_a), \quad w_a = \frac{\tau}{\rho_a} \frac{\partial}{\partial x} (\rho_a u_a^2 + p_a). \tag{3.4}$$

The viscous stress tensor and the heat flux are given by

$$\Pi_a = \Pi_a^{NS} + \tau \left[u_a \left(\rho_a u_a (u_a)_x + (p_a)_x \right) + \left(u_a (p_a)_x + \gamma_a p_a (u_a)_x \right) \right], \tag{3.5}$$

$$\Pi_a^{NS} = \left(\frac{4}{3} \eta_a + \eta_a \left(\frac{5}{3} - \gamma_a \right) \right) \frac{\partial u_a}{\partial x}, \tag{3.6}$$

$$q_a = q_a^{NS} - \tau \rho_a u_a \left[\frac{u_a}{\gamma_a - 1} \frac{\partial}{\partial x} \left(\frac{p_a}{\rho_a} \right) + p_a u_a \frac{\partial}{\partial x} \left(\frac{1}{\rho_a} \right) \right], \tag{3.7}$$

$$q_a^{NS} = -\kappa_a \frac{\partial T_a}{\partial x}. \tag{3.8}$$

Note the equations for gas b are analogous and can be obtained by substituting the subscript b into the above equations. Also, note that the Navier-Stokes viscous stress tensor is computed slightly differently, by omitting the coefficient B.

The formulation of the system is completed by adding exchange terms describing the momentum and energy transfer between the gas mixture components. S_a^u and S_a^E give the exchange terms, respectively, for the momentum and energy of gas a, and S_b^u and S_b^E give these terms for gas b. The exchange terms are calculated as follows:

$$S_a^u = \nu_{ab} \rho_a (\bar{u}_a - u_a), \tag{3.9}$$

$$S_a^E = \nu_{ab} (\bar{E}_a - E_a), \tag{3.10}$$

$$S_b^u = -S_a^u, \tag{3.11}$$

$$S_b^E = -S_a^E. \tag{3.12}$$

Here ν_{ab} is the frequency of collisions between molecules of gases a and b,

$$\nu_{ab} = \frac{p_a}{\eta_a^*} \Omega_a \sqrt{\frac{M_a + M_b}{2 M_b}} \frac{\rho_b}{\rho_a} \frac{M_a}{M_b}, \tag{3.13}$$

with

$$\Omega_a = \frac{30}{(7-2\omega_a)(5-2\omega_a)} \tag{3.14}$$

$$\eta_a^* = \eta_a^0 \left(\frac{T_a}{T_a^0}\right)^{\omega_a}, \tag{3.15}$$

and ω_a being the index describing the intermolecular interaction in gas a. For diatomic nitrogen N_2, $\omega_a = 0.74$. The dynamic viscosity and temperature of N_2 under standard conditions is given respectively as $\eta_a^0 = 1.66 \times 10^{-5}$ and $T_a^0 = 300$K. The molar masses of the gases are $M_a = 0.028$ kg/mol and $M_b = 0.024$ kg/mol.

The other values in the exchange terms, (3.9) - (3.12), are calculated by

$$\bar{u}_a = \frac{(M_a u_a + M_b u_b)}{(M_a + M_b)}, \tag{3.16}$$

$$\bar{E}_a = \frac{\rho_a \bar{u}_a^2/2 + \rho_a R_a \bar{T}_a}{(\gamma_a - 1)}, \tag{3.17}$$

$$\bar{T}_a = T_a + \frac{2M_a M_b}{(M_a + M_b)^2}\left(T_b - T_a + \frac{1}{6R_b}(u_b - u_a)^2\right). \tag{3.18}$$

Here we have the gas constants $R_a = 296.8$ and $R_b = 346.25$.

The dynamic viscosity η_a and the thermal conductivity κ_a are related to the relaxation parameter τ by

$$\eta_a = \frac{\tau p_a}{\mathrm{Sc}_a}, \quad \kappa_a = \frac{\eta_a \gamma_a R_a}{\mathrm{Pr}_a(\gamma_a - 1)}. \tag{3.19}$$

The corresponding coefficients for gas b can be found by substituting the subscript a with b. The remaining parameters are given as $\gamma_a = \gamma_b = 7/5$, $\omega_a = \omega_b = 0.74$, $\mathrm{Pr}_a = \mathrm{Pr}_b = 14/19$, and $\mathrm{Sc}_a = \mathrm{Sc}_b = 0.756$.

3.2 Numerics

The numerics for the binary gas model are treated in much the same way as the numerics for the single gas model. Again we rewrite the system in the vector form

$$\mathbf{u}_t + \mathbf{f}(\mathbf{u})_x = \mathbf{D}(\mathbf{u}). \tag{3.20}$$

Except, in this case the vectors each contain six components and the diffusion vectors is appended by the momentum and energy exchange terms.

$$\mathbf{u} = \begin{pmatrix} \rho_a \\ \rho_a u_a \\ E_a \\ \rho_b \\ \rho_b u_b \\ E_b \end{pmatrix}, \quad \mathbf{f}(\mathbf{u}) = \begin{pmatrix} \rho_a u_a \\ \rho_a u_a^2 + p_a \\ (E_a + p_a)u_a \\ \rho_b u_b \\ \rho_b u_b^2 + p_b \\ (E_b + p_b)u_b \end{pmatrix}, \quad \mathbf{D}(\mathbf{u}) = \begin{pmatrix} (\rho_a w_a)_x \\ (\Pi_a + \rho_a w_a u_a)_x + S_a^u \\ (\Pi_a u_a - q_a + w_a(E_a + p_a))_x + S_a^E \\ (\rho_b w_b)_x \\ (\Pi_b + \rho_b w_b u_b)_x + S_b^u \\ (\Pi_b u_b - q_b + w_b(E_b + p_b))_x + S_b^E \end{pmatrix}. \tag{3.21}$$

We again consider a uniform spatial grid, $x_j = j\Delta x, \quad x_{j\pm\frac{1}{2}} = (j \pm \frac{1}{2})\Delta x$, and compute the cell averages according to equation (2.32). The cell averages are evolved in time according to equation (2.33). The hyperbolic $\mathbf{H}_{j+\frac{1}{2}}$ and parabolic $\mathbf{P}_{j+\frac{1}{2}}$ numerical fluxes are described below.

Hyperbolic Flux

The hyperbolic numerical fluxes are computed analogously to the description in the single gas model, following [66] . The important difference to keep in mind is that $\mathbf{H}_{j+\frac{1}{2}}$ is now a vector containing six components. With this in mind, we proceed as before. In particular, we use the cell averages to reconstruct a conservative second-order piecewise linear interpolant via equation (2.34). We again use the generalized minmod function given in (1.69) to limit the slopes in the reconstruction. The hyperbolic numerical fluxes are then computed using equation (2.35) with point values determined in the same manner and the local speeds estimated again by (2.36).

Parabolic Flux

Again, keeping in mind that $\mathbf{P}_{j+\frac{1}{2}}$ is now a vector containing six components, the parabolic flux is constructed identically to that for the single gas except for the addition of the momentum and energy transfer terms coupling the system. These terms are not fluxes and so care must be taken to add them outside of the finite differences.

Temporal Integration

For the binary gas problem we have used the explicit third-order large stability domain Runge-Kutta method, called DUMKA and developed in[93, 94]. This high-order integration produces accurate results, and its larger stability domains (in comparison with the standard Runge-Kutta methods) allow for larger time steps; the explicit form retains simplicity, and the embedded for-

mulas permit an efficient stepsize control. In practice these methods preserve all the advantages of explicit methods and work as fast as implicit methods (see [94] for details).

3.3 Numerical Experiments

In this section we present results of the numerical experiments conducted on the one-dimensional binary-gas model. In this model the laser carbon jet expands into a nitrogen atmosphere. First we justify the use of the scheme with direct comparisons to results found in [115]. We then determine the lowest pressure admissible for the gas present in the atmosphere in Section 5.2. Similar to the single-gas experiments, we implement a version of the QGD model using a constant value for the relaxation parameter. We present these results in Section 5.3. Please note that the DUMKA time-stepping procedure is used for all binary experiments.

In the following experiments we consider the expansion of a carbon (Gas a) laser jet into a nitrogen (Gas b) atmosphere. This more accurately models the physical experiments. We would like to analyze the interaction of the shock waves that emerge during the physical process. The parameters for gas a and gas b are $\gamma_a = \gamma_b = 7/5$, $\omega_a = \omega_b = 0.74$, $Pr_a = Pr_b = 14/19$ and $Sc_a = Sc_b = 0.746$. The molar masses of the gases are $M_a = 0.028$ kg/mol and $M_b = 0.024$ kg/mol. The gas constants are $R_a = 296.8$ and $R_b = 346.25$. We consider the system (3.1) - (3.3) subject to the initial conditions,

$$(p_a(x,0), T_a(x,0), u_a(x,0)) = (p_a, T_a, 0), \quad 0 \le x \le 0.02 \text{ m}. \tag{3.22}$$

$$(p_b(x,0), T_b(x,0), u_b(x,0)) = \begin{cases} (p_b^{(1)}, T_b^{(1)}, 0), & \text{if } x \le 5 \times 10^{-6} \text{ m}, \\ (p_b^{(2)}, T_b^{(2)}, 0), & \text{if } x > 5 \times 10^{-6} \text{ m}. \end{cases} \tag{3.23}$$

The domain boundaries are taken to be solid walls. The boundary conditions for both gases are taken to be $u = 0$, $\frac{\partial \rho}{\partial x} = 0$, and $\frac{\partial T}{\partial x} = 0$.

The calculation domain is taken to be $0 \le x \le L = 0.02m$. After the laser pulse, at $t = 0$, there is a thin region, $x \le l = 5 \times 10^{-6}$, where gas b has high pressure and high temperature, while on the rest of the domain, it is at low pressure and temperature. Gas a is taken as constant on the entire domain initially. The time domain is taken to be $0 \le t \le t_f = 4\mu s$. The conservative variables ρ, ρu, and E at $t = 0$ are found using (2.18) and (1.37) and noting that $\rho u = 0$ over the entire domain initially since $u = 0$ initially.

The boundary conditions for both gases are implemented numerically as they were in the

single-gas case. I.e.,

$$\begin{aligned}
&\bar{\rho}_0 = \bar{\rho}_1, \quad \bar{u}_0 = -\bar{u}_1, \quad \bar{p}_0 = \bar{p}_1, \\
&\bar{\rho}_{N-1} = \bar{\rho}_{N-2}, \quad \bar{u}_{N-1} = -\bar{u}_{N-2}, \quad \bar{p}_{N-1} = \bar{p}_{N-2},
\end{aligned} \tag{3.24}$$

where N is the number of grid points.

The relaxation parameter is chosen according to the formula given for the single gas problem, with the parameter $\alpha = 0.6$. Namely,

$$\tau_a = \tau_b = \frac{0.6\Delta x}{\mathrm{Sc} \cdot c}, \tag{3.25}$$

where c=$\sqrt{\gamma_a R_a T_a}$ is the speed of sound in nitrogen.

3.3.1 Example *A*

In this section we present results from the computation of the binary gas laser ablation problem with initial conditions given by (3.22) - (3.23). The initial values of pressure and temperature for the different simulations are given below. Note that the changes between simulations are in the pressure of gas a and the temperature and pressure of gas b in the strike zone. The initial values that do not vary between simulations are,

$$T_a = 300 \text{ K}, \quad p_b^{(2)} = 10^3 \text{ Pa}, \quad T_b^{(2)} = 300 \text{ K}. \tag{3.26}$$

An increase in the pressure of the buffer gas is implemented in Version **2**. Versions **3** and **4** are characterized by a decrease in the pressure of the carbon gas in the strike zone. The initial conditions for the Versions $\mathbf{1-4}$ are given below.

$$\text{Version}\mathbf{1}: p_a = 10^3 \text{ Pa}, \quad p_b^{(1)} = 10^{10} \text{ Pa}, \quad T_b^{(1)} = 10^4 \text{ K}. \tag{3.27}$$

$$\text{Version}\mathbf{2}: p_a = 10^4 \text{ Pa}, \quad p_b^{(1)} = 10^{10} \text{ Pa}, \quad T_b^{(1)} = 10^4 \text{ K}. \tag{3.28}$$

$$\text{Version}\mathbf{3}: p_a = 10^3 \text{ Pa}, \quad p_b^{(1)} = 10^9 \text{ Pa}, \quad T_b^{(1)} = 3 \times 10^4 \text{ K}. \tag{3.29}$$

$$\text{Version}\mathbf{4}: p_a = 10^4 \text{ Pa}, \quad p_b^{(1)} = 10^9 \text{ Pa}, \quad T_b^{(1)} = 3 \times 10^4 \text{ K}. \tag{3.30}$$

The spatial cell size is given as $\Delta x = 4 \times 10^{-6}$. The minmod parameter is set at $\theta = 1.5$, except for Version **2** where $\theta = 1.3$ is necessary to resolve a solution.

Figures 3.1 - 3.4 provide the corresponding results. It is noted that the results produced are in agreement with those produced in [115]. When compared to previously obtained results, the scheme produces substantially sharper resolution of the shock fronts. As important, the results presented here display a much better alignment of the shock expansion in each gas. Numerical

drift had previously contributed to a separation in the approximations of the expansion of the shocks.

3.3.2 Example *B* - Low Pressure

In this experiment we wanted to determine the lowest admissible pressure $p_b^{(2)}$, the pressure of carbon in the atmosphere. Physically, we would like this value to be as low as possible. The initial conditions are the same as Version **1**, except for the lower value for $p_b^{(2)}$.

$$T_a = 300 \text{ K}, \quad p_b^{(2)} = 151 \text{ Pa}, \quad T_b^{(2)} = 300 \text{ K}. \tag{3.31}$$

$$p_a = 10^3 \text{ Pa}, \quad p_b^{(1)} = 10^{10} \text{ Pa}, \quad T_b^{(1)} = 10^4 \text{ K} \tag{3.32}$$

The lowest admissible pressure achieved is $p_b^{(2)} = 151$ Pa, which is a full order of magnitude lower than previously obtained. Figure 3.5 shows the result plotted at $x = 5\ mm$ and $x = 11\ mm$ using a spatial cell size given by $\Delta x = 4 \times 10^{-6}$ m. When compared with the results using the initial conditions given in Version **1**, see Figure 3.1, we see that at $x = 11\ mm$ a smoother shock front is apparent in the experiment with the lower atmospheric pressure. This is consistent with the expectation that having less pressure allows for a smoother spreading of the plasma.

3.3.3 Example *C* - Constant τ

For this experiment we consider the binary-gas problem with the initial conditions given by (3.27). The minmod parameter $\theta = 1.5$. Again, we use a spatial cell size given by $\Delta x = 4 \times 10^{-6}$ m.

A numerical analysis of the relaxation parameter was carried out analogously with the analysis in Section 4.5, with similar results. The value for the relaxation parameter in the constant τ experiments is chosen according to optimum efficiency and accuracy. As with the single-gas experiments, we found $\tau = 10^{-9}$ gives us a desirable approximation. We see, in Figures 3.6 and 3.7, that the constant τ simulation provides a sharper resolution than QGD simulation. We also found that for the binary gas model, the constant τ model actually provides us with a modest computational-time savings.

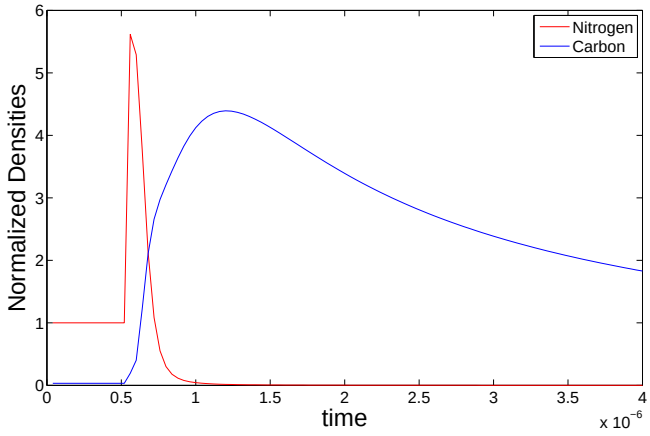

(a) $x = 5mm$

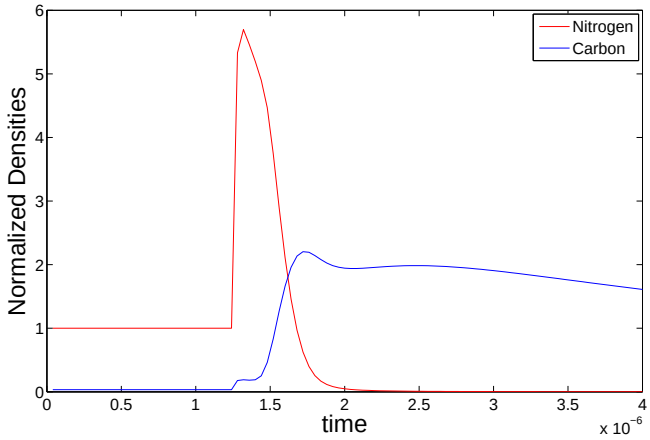

(b) $x = 11mm$

Figure 3.1: **Example A** (Version **1**) Solution (normalized density) plotted against time at the indicated distance from the strike zone, computed on grid with $\Delta x = 4 \times 10^{-6}$ m.

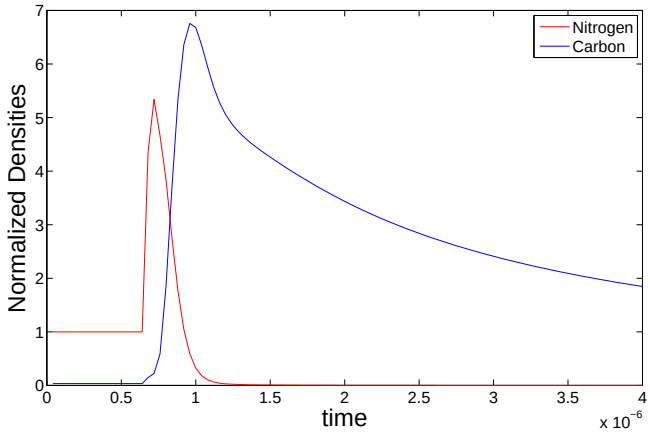

(a) $x = 5mm$

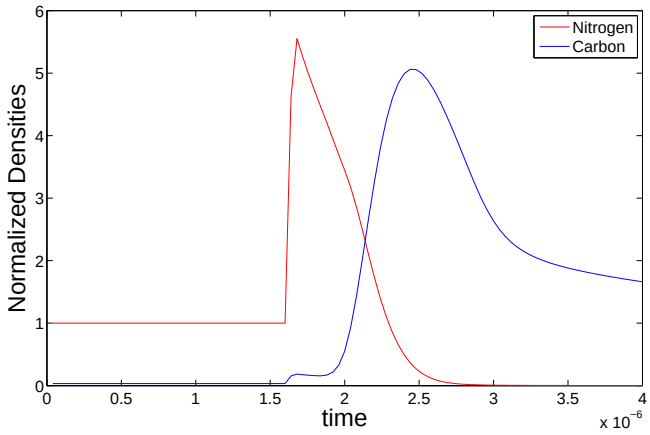

(b) $x = 11mm$

Figure 3.2: **Example A** (Version **2**) Solution (normalized density) plotted against time at the indicated distance from the strike zone, computed on grid with $\Delta x = 4 \times 10^{-6}$ m.

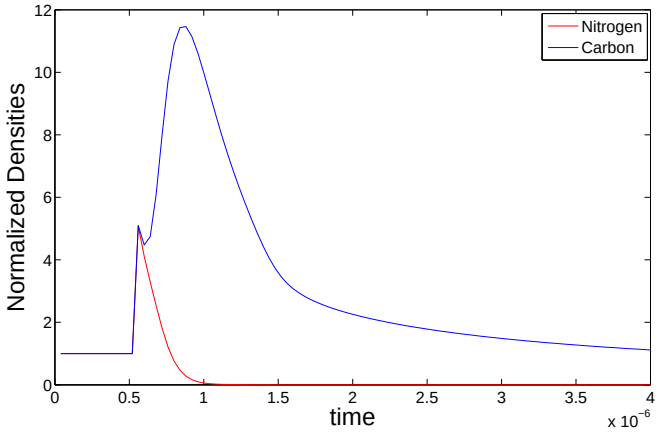

(a) $x = 5mm$

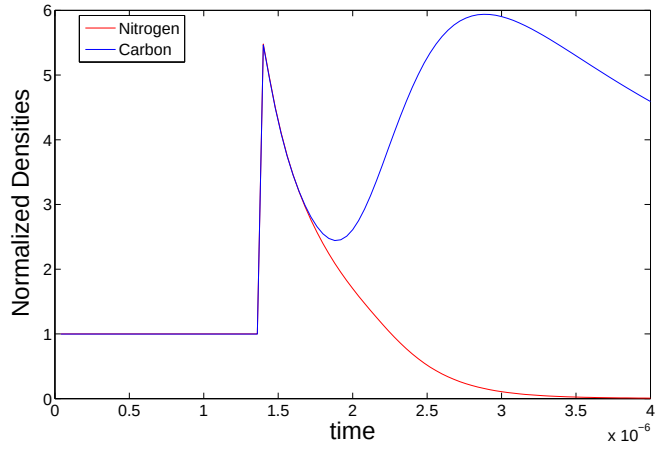

(b) $x = 11mm$

Figure 3.3: **Example A** (Version **3**) Solution (normalized density) plotted against time at the indicated distance from the strike zone, computed on grid with $\Delta x = 4 \times 10^{-6}$ m.

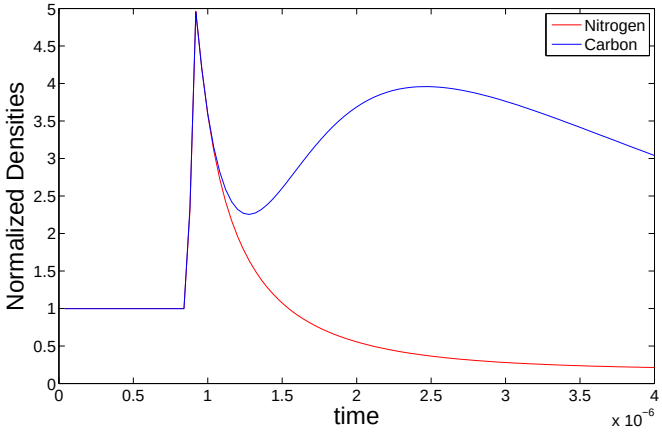

(a) $x = 5mm$

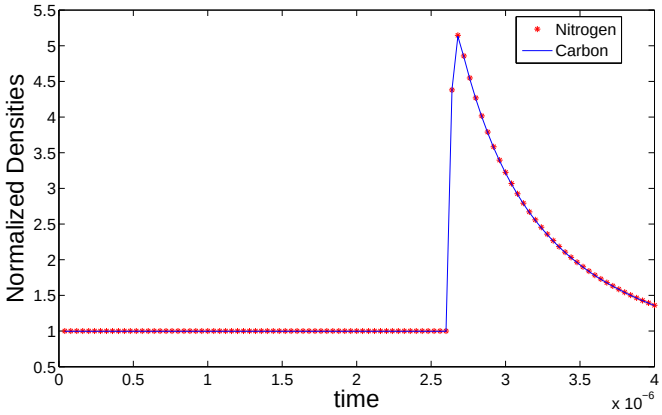

(b) $x = 11mm$

Figure 3.4: **Example A** (Version **4**) Solution (normalized density) plotted against time at the indicated distance from the strike zone, computed on grid with $\Delta x = 4 \times 10^{-6}$ m.

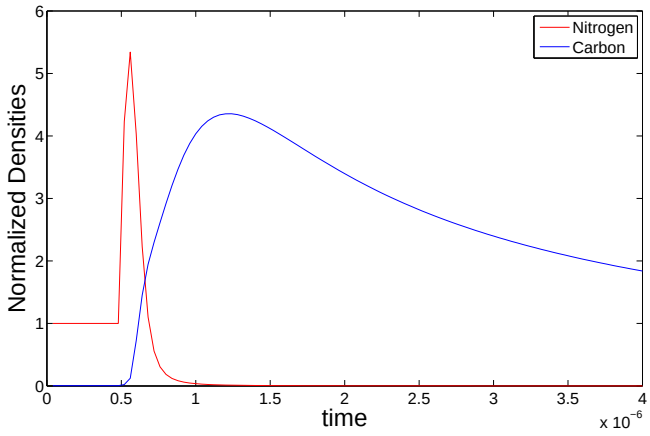

(a) $x = 5mm$

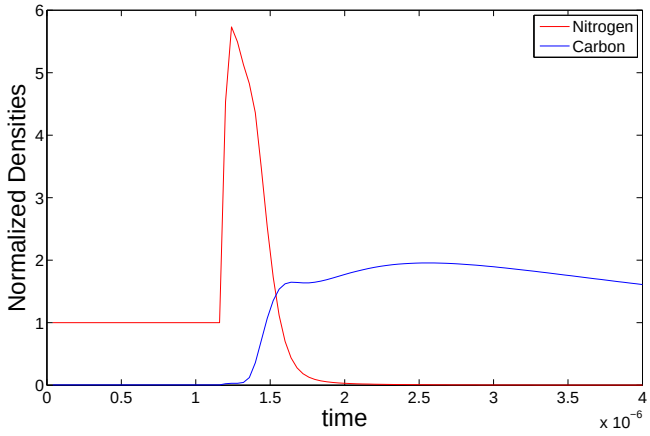

(b) $x = 11mm$

Figure 3.5: **Example B** - Lowest admissible initial atmospheric pressure. Solution (normalized density) plotted against time at the indicated distance from the strike zone, computed on grid with $\Delta x = 4 \times 10^{-6}$ m.

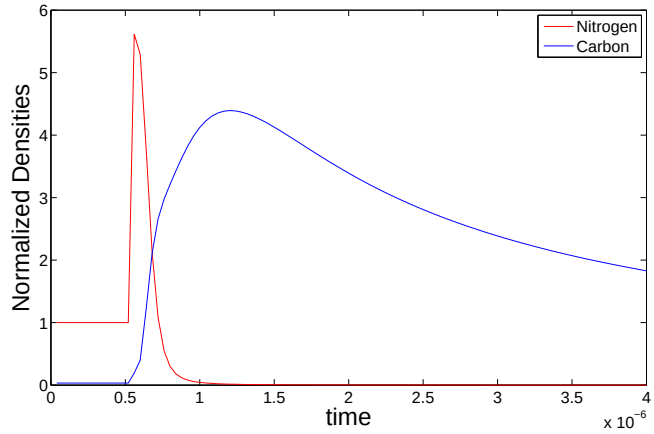

(a) QGD

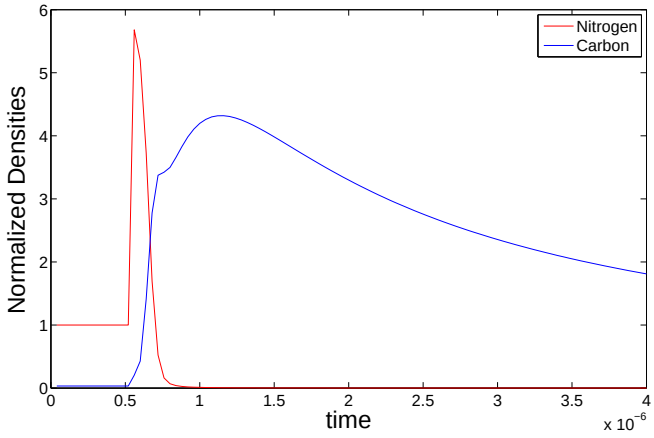

(b) Constant $\tau = 10^{-9}$

Figure 3.6: **Example C** Comparison of the QGD model with constant τ model for the binary gas problem. Solution (normalized density) is plotted against time at a distance $x = 5mm$ from the strike zone, computed on grid with $\Delta x = 4 \times 10^{-6}$ m.

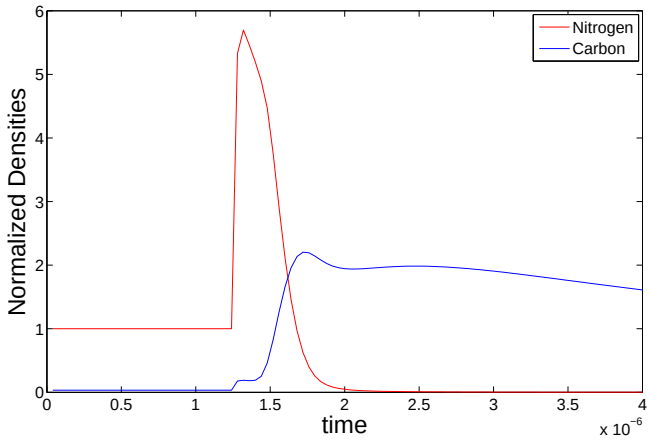

(a) QGD

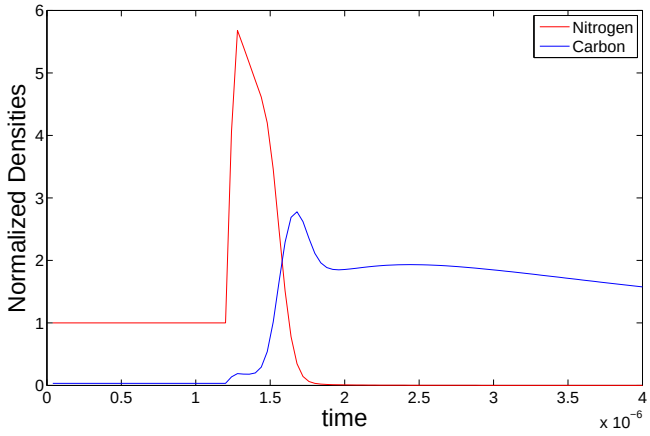

(b) Constant $\tau = 10^{-9}$

Figure 3.7: **Example C** Comparison of the QGD model with constant τ model for the binary gas problem. Solution (normalized density) is plotted against time at a distance $x = 11mm$ from the strike zone, computed on grid with $\Delta x = 4 \times 10^{-6}$ m.

Chapter 4

Quasi Two-Dimensional Radially Symmetric Laser Ablation

4.1 Mathematical Model

This section presents the quasi two-dimensional, radially symmetric representation of the QGD equations. This model is derived by rewriting the equations in polar coordinates. Then, by taking advantage of symmetry, we can reduce the dependence of the system to the single space variable, r:

$$\frac{\partial \rho}{\partial t} + \frac{1}{r}\frac{\partial (r j_{mr})}{\partial r} = 0 \tag{4.1}$$

$$\frac{\partial (\rho u_r)}{\partial t} + \frac{1}{r}\frac{\partial (r j_{mr} u_r)}{\partial r} + \frac{\partial p}{\partial r} = \frac{1}{r}\frac{\partial (r \Pi^{(rr)})}{\partial r} \tag{4.2}$$

$$\frac{\partial E}{\partial t} + \frac{1}{r}\frac{\partial (r j_{mr} H)}{\partial r} + \frac{1}{r}\frac{\partial (r q^{(r)})}{\partial r} = \frac{1}{r}\frac{(r u_r \partial \Pi^{(rr)})}{\partial r} \tag{4.3}$$

In the above equations, the r notation indicates the r components of the notated variable. E.g., u_r signifies the r component of velocity. Since this is the only component in the derivation, the notation is dropped in the following. The mass flux density (j_m), viscosity component (Π), and

heat flux (q) are given below.

$$j_m = \rho u - \tau \left(\frac{1}{r} \frac{\partial (r\rho u^2)}{\partial r} + \frac{\partial p}{\partial r} \right) \tag{4.4}$$

$$\Pi = \mu \left(2\frac{\partial u}{\partial r} - \left[\frac{2}{3} - \frac{\zeta}{\mu} \right] \frac{1}{r} \frac{\partial (ru)}{\partial r} \right) + \tau \rho u \left(u \frac{\partial u}{\partial r} + \frac{1}{\rho} \frac{\partial p}{\partial r} \right) + \tau \left(u \frac{\partial p}{\partial r} + \gamma p \frac{1}{r} \frac{\partial (ru)}{\partial r} \right) \tag{4.5}$$

$$q = -\kappa \frac{\partial T}{\partial r} - u \left[\frac{\tau \rho}{\gamma - 1} \left(u \frac{\partial}{\partial r} \left(\frac{p}{\rho} \right) \right) + \tau \rho p \left(u \frac{\partial}{\partial r} \left(\frac{1}{\rho} \right) \right) \right] \tag{4.6}$$

The coefficients for dynamic viscosity μ, thermal conductivity κ, and bulk viscosity ζ, are related to the relaxation parameter τ. The formulas for these are given below.

$$\tau = \alpha \frac{\Delta r_{\min}}{c_s} \tag{4.7}$$

$$\mu = \tau p \mathrm{Sc} \tag{4.8}$$

$$\zeta = \tau p \left(\frac{5}{3} - \gamma \right) \tag{4.9}$$

$$\kappa = \frac{\mu \gamma R}{\mathrm{Pr}(\gamma - 1)} \tag{4.10}$$

The speed of sound in an ideal gas is c_s and the parameter α are determined experimentally. In the above formulas we have $c_s = (\gamma R T_2)^{\frac{1}{2}} = 381.3$ m/s, where T_2 is the temperature of an ideal gas. The remaining parameters are given as $R = 346.25$ is the gas constant, $\gamma = 1.4$ is the adiabatic index, and Sc=0.746 and Pr=14/19 are the Schmidt and Prandtl numbers respectively.

Multiplying equations (4.1)-(4.2) through by the spatial variable r gives us the following configuration of the equations.

$$\frac{\partial (r\rho)}{\partial t} + \frac{\partial (r j_m)}{\partial r} = 0 \tag{4.11}$$

$$\frac{\partial (r\rho u)}{\partial t} + \frac{\partial (r j_m u)}{\partial r} + r \frac{\partial p}{\partial r} = \frac{\partial (r\Pi)}{\partial r} \tag{4.12}$$

$$\frac{\partial (rE)}{\partial t} + \frac{\partial (r j_m H)}{\partial r} + \frac{\partial (rq)}{\partial r} = \frac{\partial (ru\Pi)}{\partial r} \tag{4.13}$$

Note that the conservative variables are now given by the vector $\mathbf{u} = (r\rho, r\rho u, rE)^T$. Now, in order to obtain a more numerically workable derivation, we expand the mass flux density in each equation according to its formula.

Equation (4.11)

Substituting the equation for the mass flux density, (4.4), into the conservation of mass equation, (4.11), give us the following representation of the formula.

$$\frac{\partial(r\rho)}{\partial t} + \frac{\partial}{\partial r}\left[r\left(\rho u - \tau\left(\frac{1}{r}\frac{\partial(r\rho u^2)}{\partial r} + \frac{\partial p}{\partial r}\right)\right)\right] = 0 \implies$$
$$\frac{\partial(r\rho)}{\partial t} + \frac{\partial(r\rho u)}{\partial r} = \frac{\partial}{\partial r}\left(\tau\frac{\partial}{\partial r}(r\rho u^2) + \tau r\frac{\partial p}{\partial r}\right) \tag{4.14}$$

Equation (4.12)

The equation for conservation of momentum is expanded as follows. Again, we substitute the equation for the mass flux density, (4.4), into the conservation of momentum equation, (4.12). Note that the substitution, $r\frac{\partial p}{\partial r} = \frac{\partial(rp)}{\partial r} - p$, is used in the following expansion.

$$\frac{\partial(r\rho u)}{\partial t} + \frac{\partial}{\partial r}\left[ru\left(\rho u - \tau\left(\frac{1}{r}\frac{\partial(r\rho u^2)}{\partial r} + \frac{\partial p}{\partial r}\right)\right)\right] + \frac{\partial(rp)}{\partial r} - p = \frac{\partial(r\Pi)}{\partial r} \implies$$
$$\frac{\partial(r\rho u)}{\partial t} + \frac{\partial(r(\rho u^2 + p))}{\partial r} = \frac{\partial}{\partial r}(r\Pi) + \frac{\partial}{\partial r}\left(\tau u\frac{\partial}{\partial r}(r\rho u^2) + \tau r u\frac{\partial p}{\partial r}\right) + p \tag{4.15}$$

Equation (4.13)

The final equation in this section, the conservation of energy, is expanding similarly. Note that the formula for enthalpy, $H = \frac{E+p}{\rho}$ is used in the derivation.

$$\frac{\partial(rE)}{\partial t} + \frac{\partial}{\partial r}\left[r\left(\rho u - \tau\left(\frac{1}{r}\frac{\partial(r\rho u^2)}{\partial r} + \frac{\partial p}{\partial r}\right)\right)H\right] = \frac{\partial(ru\Pi)}{\partial r} - \frac{\partial(rq)}{\partial r} \implies$$
$$\frac{\partial(rE)}{\partial t} + \frac{\partial\left(ru(E+p)\right)}{\partial r} = \frac{\partial}{\partial r}(r\Pi u) - \frac{\partial}{\partial r}(rq) + \frac{\partial}{\partial r}\left(\tau H\frac{\partial}{\partial r}(r\rho u^2)\right) + \frac{\partial}{\partial r}\left(\tau r H\frac{\partial p}{\partial r}\right) \tag{4.16}$$

4.2 Numerics

We use the one-dimensional version of the second-order central-upwind scheme [66] to solve the radially symmetric QGD equations. Note that in the sequel, the subscript r notation refers to the spatial derivative. First we rewrite the system derived in equations (4.14)-(4.15) in vector form:

$$\mathbf{u}_t + \mathbf{f}(\mathbf{u})_r = \mathbf{D}(\mathbf{u}). \tag{4.17}$$

Here, $\mathbf{u}$ is the unknown vector of conservative variables, $\mathbf{f}$ represents the the convective nonlinear flux and $\mathbf{D}$ the nonlinear diffusion term:

$$\mathbf{u} = \begin{pmatrix} r\rho \\ r\rho u \\ rE \end{pmatrix}, \quad \mathbf{f}(\mathbf{u}) = \begin{pmatrix} r\rho u \\ r(\rho u^2 + p) \\ ru(E+p) \end{pmatrix},$$

$$\mathbf{D}(\mathbf{u}) = \begin{pmatrix} \frac{\partial}{\partial r}\left(\tau \frac{\partial}{\partial r}(r\rho u^2) + \tau r \frac{\partial p}{\partial r}\right) \\ \frac{\partial}{\partial r}(r\Pi) + \frac{\partial}{\partial r}\left(\tau u \frac{\partial}{\partial r}(r\rho u^2) + \tau r u \frac{\partial p}{\partial r}\right) + p \\ \frac{\partial}{\partial r}(r\Pi u) - \frac{\partial}{\partial r}(rq) + \frac{\partial}{\partial r}\left(\tau H \frac{\partial}{\partial r}(r\rho u^2)\right) + \frac{\partial}{\partial r}\left(\tau r H \frac{\partial p}{\partial r}\right) \end{pmatrix}. \tag{4.18}$$

Note that the additional term for pressure in the second component of the diffusion flux is not actually a flux and will be handled outside of the parabolic flux.

Again we consider a uniform grid of size Δr and use the notation: $r_j = j\Delta r$, $r_{j\pm\frac{1}{2}} = (j \pm \frac{1}{2})\Delta r$. The cell averages are computed according to

$$\overline{\mathbf{u}}_j(t) = \frac{1}{\Delta r} \int_{r_{j-\frac{1}{2}}}^{r_{j+\frac{1}{2}}} \mathbf{u}(r,t)\, dr. \tag{4.19}$$

The semi-discrete version of the PDE is given by

$$\frac{d}{dt}\overline{\mathbf{u}}_j(t) = -\frac{\mathbf{H}_{j+\frac{1}{2}}(t) - \mathbf{H}_{j-\frac{1}{2}}(t)}{\Delta r} + \frac{\mathbf{P}_{j+\frac{1}{2}}(t) - \mathbf{P}_{j-\frac{1}{2}}(t)}{\Delta r} + (0, p, 0)^T. \tag{4.20}$$

The hyperbolic $\mathbf{H}_{j+\frac{1}{2}}$ and parabolic $\mathbf{P}_{j+\frac{1}{2}}$ numerical fluxes are constructed as follows.

Hyperbolic Flux

The hyperbolic numerical fluxes are computed identically to the one-dimensional single gas problem, [66]. In particular, we use the cell averages to reconstruct a conservative second-order piecewise linear interpolant via equation (2.34). We again use the generalized minmod function given in (1.69) to limit the slopes in the reconstruction. The hyperbolic numerical fluxes are then computed using equation (2.35) with point values determined in the same manner and the local speeds estimated again by (2.36). Note that the spatial variable r is cancelled out in the calculation of the local speeds.

Parabolic Flux

To compute the parabolic numerical fluxes, $\mathbf{P}_{j+\frac{1}{2}}$, we first rewrite the diffusion in a way similar to the derivation of the parabolic fluxes in the single gas model (see Section 1.2.3). This,

again, is to take advantage of redundant information to ease computation. In the following, let $W = r\rho u^2$ and recall enthalpy is given by $H = (E + p)/\rho$. The diffusion is then written as

$$\mathbf{D}(\mathbf{u}) = \begin{pmatrix} \tau W_r + \tau r p_r \\ u(\tau W_R + \tau r p_r) + r\Pi \\ H(\tau W_r + \tau r p_r) + r\Pi u - rq \end{pmatrix}. \tag{4.21}$$

Observing the flux written this way makes apparent the information we will be able to reuse. Namely, $r\Pi$ and $\tau W_r + \tau r p_r$. The viscous stress tensor Π is given as

$$\Pi = z_1 u_r + z_2 (ru)_r + z_3 p_r, \tag{4.22}$$

where the coefficents in (4.22) are given as

$$z_1 = 2\mu + \tau\rho u^2, \tag{4.23}$$

$$z_2 = -\mu\beta\frac{1}{r} + \tau\gamma p\frac{1}{r}, \tag{4.24}$$

$$z_3 = 2\tau u. \tag{4.25}$$

The heat flux is treated a bit more carefully to avoid the calculation of extraneous derivatives. In particular, we would like to express the temperature gradient in terms of pressure and density. The flux is repeated below for convenience,

$$q = -\kappa T_r + \left(-\frac{\tau u^2 \rho}{\gamma - 1}\left(\frac{p}{\rho}\right)_r\right) + \left(-\tau\rho p u^2 \left(\frac{1}{\rho}\right)_r\right). \tag{4.26}$$

The first term in equation (4.26) is rewritten as

$$-\kappa T_r = -\frac{\mu\gamma R}{\mathrm{Pr}(\gamma - 1)} T_r = \left(\frac{-\tau\gamma R \mathrm{Sc}}{\mathrm{Pr}(\gamma - 1)}\right) p T_r \doteq c_1 p T_r. \tag{4.27}$$

Now we use the ideal gas law, $T = \frac{p}{\rho R}$ to express the temperature gradient as

$$T_r = \frac{1}{R}\left(\frac{p}{\rho}\right)_r, \tag{4.28}$$

and the product rule to expand the gradient of $\frac{p}{\rho}$ as

$$\left(\frac{p}{\rho}\right)_r = \frac{p_r\rho - p\rho_r}{\rho^2}. \tag{4.29}$$

Now we can express equation (4.27) as follows:

$$c_1 p T_r = \frac{c_1}{R} p \left(\frac{p_r \rho - p \rho_r}{\rho^2} \right) = \frac{c_1}{R} \left(\frac{p}{\rho} p_r - \frac{p^2}{\rho^2} \rho_r \right) = \frac{c_1}{R} \left(RT p_r - (RT)^2 \rho_r \right) \tag{4.30}$$

$$= c_1 (T p_r - RT^2 \rho_r). \tag{4.31}$$

Using again the expansion in (4.29), the second term becomes

$$\frac{-\tau}{\gamma - 1} \left(u^2 \rho \left(\frac{p}{\rho} \right)_r \right) \doteq c_2 \left(u^2 \rho \left(\frac{p_r \rho - p \rho_r}{\rho^2} \right) \right) \tag{4.32}$$

$$= c_2 \left(u^2 p_r - \frac{u^2 p}{\rho} \rho_r \right). \tag{4.33}$$

Similarly, the third term can be written as

$$-\tau \left(\rho p u^2 \left(\frac{1}{\rho} \right)_r \right) = -\tau \left(\rho p u^2 \left(\frac{-\rho_r}{\rho^2} \right) \right) \tag{4.34}$$

$$= \tau \frac{p u^2}{\rho} \rho_r. \tag{4.35}$$

So, we can write the heat flux as

$$q = c_1 (T p_r - RT^2 \rho_r) + c_2 (u^2 p_r - \frac{u^2 p}{\rho} \rho_r) + \tau \frac{p u^2}{\rho} \rho_r \tag{4.36}$$

$$= (c_1 T + c_2 u^2) p_r + (-c_1 RT^2 - c_2 \frac{u^2 p}{\rho} + \tau \frac{p u^2}{\rho}) \rho_r, \tag{4.37}$$

where

$$c_1 = \left(\frac{-\tau \gamma R \mathrm{Sc}}{\mathrm{Pr}(\gamma - 1)} \right), \tag{4.38}$$

$$c_2 = -\frac{\tau}{\gamma - 1}. \tag{4.39}$$

The parabolic numerical flux is written in component form as $\mathbf{P}_{j+\frac{1}{2}} = \left(P^{(1)}_{j+\frac{1}{2}}, P^{(2)}_{j+\frac{1}{2}}, P^{(3)}_{j+\frac{1}{2}} \right)^T$. The individual components are computed similarly to the equations (2.39)-(2.41) in the single gas section. E.g.,

$$P^{(1)}_{j+\frac{1}{2}} = \tau_{j+\frac{1}{2}} \left(\frac{\overline{W}_{j+1} - \overline{W}_j}{\Delta r} \right) + \tau_{j+\frac{1}{2}} r_{j+\frac{1}{2}} \left(\frac{\overline{p}_{j+1} - \overline{p}_j}{\Delta r} \right) \tag{4.40}$$

Again, the bar notation indicates cell averages, and the $j + \frac{1}{2}$ terms are evaluated at the flux boundaries.

Temporal Integration

For the radially symmetric problem we have used the explicit third-order large stability domain Runge-Kutta method, called DUMKA and developed in[93, 94]. This high-order integration produces accurate results, and its larger stability domains (in comparison with the standard Runge-Kutta methods) allow for larger time steps; the explicit form retains simplicity, and the embedded formulas permit an efficient stepsize control. In practice these methods preserve all the advantages of explicit methods and work as fast as implicit methods (see [94] for details).

4.3 Numerical Experiments

We reduce the complexity of the two-dimensional problem by introducing a radially symmetric model. The model is presented in polar coordinates with the assumption that there is no variation in the θ direction. By taking advantage of this symmetry we are able to reduce the equations to a dependence on only the single spatial variable r. In addition to giving us insight in to the behavior of the two-dimensional problem with a simple, efficient method, computing the radially symmetric solution provides a valuable validation of multi-dimensional results [77].

Under consideration is the spread of the plasma of molecular carbon C_2 in a vacuum. Carbon has constant parameters $R = 346.25$, $\gamma = 7/5$, $\omega = 0.74$, $Pr = 14/19$ and $Sc = 0.746$.

The schematic in Figure 5.1 gives the set-up for the two-dimensional laser ablation problem including the boundary conditions. These initial conditions are implemented in one dimension as follows.

The initial velocity is zero everywhere, i.e. $u = 0$. The initial conditions for pressure and temperature are given in the experiments below. The calculation domain is given by $0 \leq x \leq L = 0.02$ m. After the laser pulse, at $t = 0$, there is a small region where the strike results in a high-pressure and high-temperature region, given by $0 \leq x \leq l = 5.45 \times 10^{-5}$ m. The time domain is taken to be $0 \leq t \leq t_f = 4\mu s$.

The boundary conditions are given in Figure 5.1. Since our problem has been simplified to one-dimension, we implement the boundary conditions numerically as follows. Note, N is the number of grid points.

$$\begin{aligned} \bar{\rho}_0 = \bar{\rho}_1, \quad \bar{u}_0 = -\bar{u}_1, \quad \bar{p}_0 = \bar{p}_1 \\ \bar{\rho}_{N+1} = \bar{\rho}_N, \quad \bar{u}_{N+1} = \bar{u}_N, \quad \bar{p}_{N+1} = \bar{p}_N \end{aligned} \tag{4.41}$$

The polar coordinates demand extra care when implementing the boundary conditions. This is because our conservative variables are given by $(r\rho, r\rho u, rE)^T$. So we must take into account the sign and value of r at the boundary. Note that $r_0 = -\Delta r/2 = -r_1$ and $r_{N+1} = r_N + \Delta r$.

So, for example, when we want to determine the boundary conditions at $r = 0$, we get the

following expressions.

$$(r\rho)_0 = r_0\rho_0 = (-r_1)\rho_1 = -(r\rho)_1 \tag{4.42}$$

$$(r\rho u)_0 = r_0\rho_0 u_0 = (-r_1)\rho_1(-u_1) = (r\rho u)_1 \tag{4.43}$$

$$(rE)_0 = r_0 E_0 = (-r_1)(E_1) = -(rE)_1 \tag{4.44}$$

Note that the boundary conditions for energy are determined through the equation of state. The boundary conditions at $r = L$ are given below.

$$(r\rho)_{N+1} = r_{N+1}\rho_{N+1} = (r_N + \Delta r)\rho_N = (r_N + \Delta r)\frac{(r\rho)_N}{r_N} = \frac{r_N + \Delta r}{r_N}(r\rho)_N \tag{4.45}$$

$$(r\rho u)_{N+1} = r_{N+1}\rho_{N+1}u_{N+1} = (r_N + \Delta r)\rho_N(-u_N) = -(r_N + \Delta r)\frac{(r\rho)_N u_N}{r_N} = -\frac{r_N + \Delta r}{r_N}(r\rho u)_N \tag{4.46}$$

$$(rE)_{N+1} = r_{N+1}E_{N+1} = (r_N + \Delta r)E_N = (r_N + \Delta r)\frac{(rE)_N}{r_N} = \frac{r_N + \Delta r}{r_N}(rE)_N \tag{4.47}$$

4.3.1 Experiment 1

First we run the quasi two-dimensional radially symmetric simulation with the initial conditions given for the two-dimensional problem. The initial pressure and temperature are

$$\begin{aligned} p_1 &= 10^8\text{Pa}, \quad T_1 = 5 \times 10^4 \text{ K}, \\ p_2 &= 10^3\text{Pa}, \quad T_2 = 300 \text{ K}. \end{aligned} \tag{4.48}$$

The simulation is run with $\theta = 1.3$ and $\Delta r = 5 \times 10^{-5}$ m. The relaxation parameter is given by equation (4.7) with $\alpha = 0.3$, which is determined experimentally. We are able to take such a relatively large value for r due to the size of the initial strike zone in the two-dimensional problem. This results in a blazing computation time. The run time for this experiment is about 15 seconds! Figure 4.1 gives the results for the experiment. Note that the high pressure in the atmosphere radically slows the expansion, so much so that the plasma jet does not even reach $x = 11$ mm in the allotted time. Note this is consistent with the corresponding results we find in the two-dimensional simulation.

4.3.2 Experiment 2

Next we attempt to lower the atmospheric pressure, p_2, while maintaining the remaining physical conditions constant. Again, the simulation is run with $\theta = 1.3$ and $\Delta r = 5 \times 10^{-5}$ m. The relaxation parameter is given by equation (4.7) with $\alpha = 0.3$. First we lower the pressure in

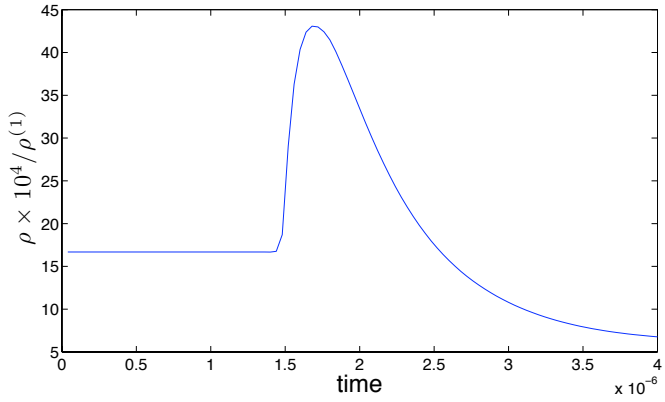

(a) $x = 5mm$

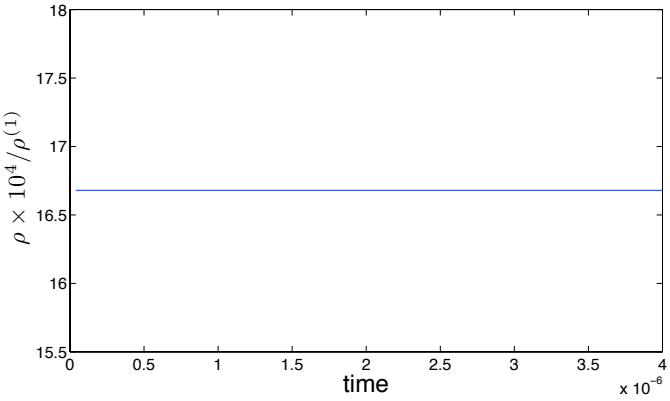

(b) $x = 11mm$

Figure 4.1: **Experiment 1** Solution (normalized density) plotted against time at the indicated distance from the strike zone, computed on grid with $\Delta x = 5 \times 10^{-5}$ m.

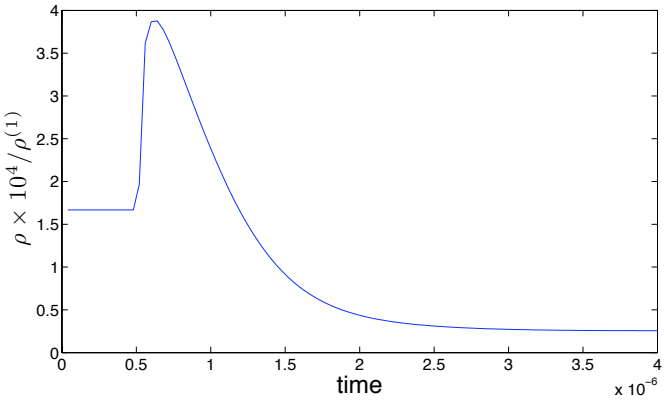

(a) $x = 5mm$

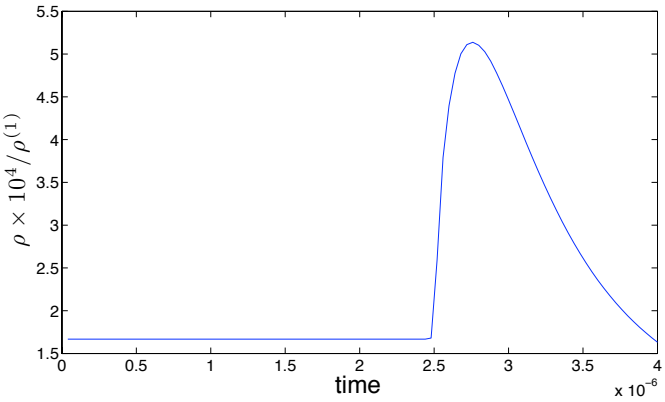

(b) $x = 11mm$

Figure 4.2: **Experiment 2** Solution (normalized density) plotted against time at the indicated distance from the strike zone, computed on grid with $\Delta x = 5 \times 10^{-5}$ m.

the expansion atmosphere to $p_2 = 100$ Pa. The initial conditions are given by

$$\begin{aligned} p_1 &= 10^8 \text{Pa}, \quad T_1 = 5 \times 10^4 \text{ K}, \\ p_2 &= 10^2 \text{Pa}, \quad T_2 = 300 \text{ K}. \end{aligned} \tag{4.49}$$

The results for this numerical experiment are given in Figure 4.2. Note that the expansion is much quicker due to the lower atmospheric pressure. Next, we try to lower this pressure to $p_2 = 10$ Pa. In this case, the simulation is unable to complete the simulation. It produces results only through the time $t \approx 2.8\mu s$. Note that this corresponds to the time the at which the expansion hits the outer boundary.

4.3.3 Experiment 3

In this experiment, we increase the pressure in the strike zone to $p_1 = 10^9$ Pa. Then we again determine how low we can bring the pressure in the expansion atmosphere. Again, the simulation is run with $\theta = 1.3$ and $\Delta r = 5 \times 10^{-5}$ m. The relaxation parameter is given by equation (4.7) with $\alpha = 0.3$. We see in Figure 4.3 the results to the problem with the following initial conditions,

$$\begin{aligned} p_1 = 10^9 \text{Pa}, \quad T_1 = 5 \times 10^4 \text{ K}, \\ p_2 = 10^3 \text{Pa}, \quad T_2 = 300 \text{ K}. \end{aligned} \tag{4.50}$$

The expansion is nearly identical to the the Experiment 2, due to the similarity in the pressure gradient of the initial condition. Again, the run times are about 15 seconds.

Next we try to the run the simulation with the pressure p_2 lowered by an order of magnitude. Again, we find the simulation runs until the time $t \approx 2.9\mu s$, which again matches the time that the expansion hits the outer boundary.

4.3.4 Experiment 4

In this section we attempt to run the radially symmetric model with the initial conditions given as

$$\begin{aligned} p_1 = 10^8 \text{Pa}, \quad T_1 = 5 \times 10^4 \text{ K}, \\ p_2 = 3 \text{Pa}, \quad T_2 = 300 \text{ K}. \end{aligned} \tag{4.51}$$

We attempt to resolve a solution by manipulating the minmod parameter θ and the constant α that controls the relaxation parameter τ.

We begin by lowering the minmod parameter θ. Recall that θ controls the slope limiter in the reconstruction of the piecewise linear interpolant used in the computation of the hyperbolic numerical flux. The parameter $\theta \in [1, 2]$, where $\theta = 1$ provides the greatest amount of smoothing. In trying to compute a solution with the large initial pressure gradient, we found that even with $\theta = 1.0$, the scheme was not able to complete the simulation.

Next, holding $\theta = 1.0$, we increase the value of α. This adds additional smoothing through its control of the artificial viscosity. We were only able to reach a full simulation when $\alpha = 0.8$. This is the amount of additional viscosity needed to slow the expansion. In fact, the relaxation parameter may be made more oscillatory at this point. The plot in Figure 4.4, provides the results obtained with $\theta = 1.3$ and $\alpha = 0.8$, computed on a grid with$\Delta x = 5 \times 10^{-5}$ m. Although the numerical scheme is able to resolve a solution to the problem with initial conditions given

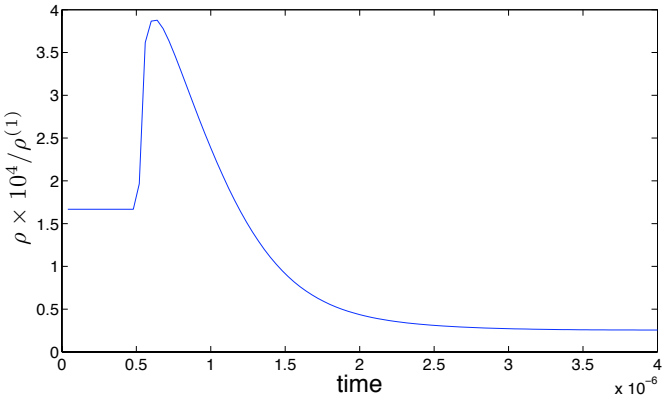

(a) $x = 5mm$

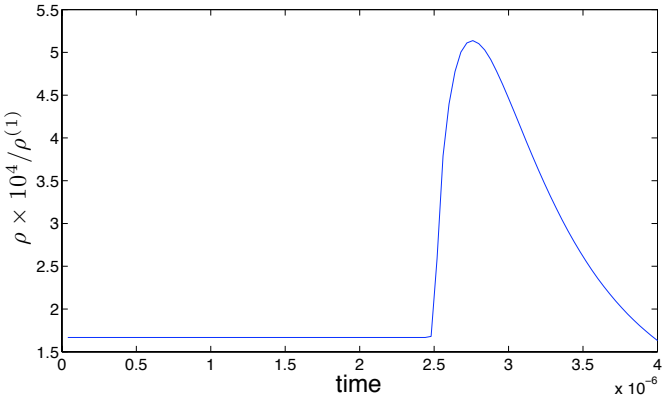

(b) $x = 11mm$

Figure 4.3: **Experiment 3** Solution (normalized density) plotted against time at the indicated distance from the strike zone, computed on grid with $\Delta x = 5 \times 10^{-5}$ m.

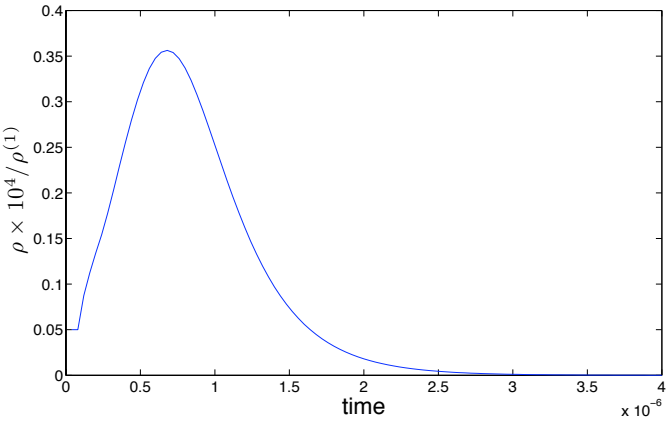

(a) $x = 5mm$

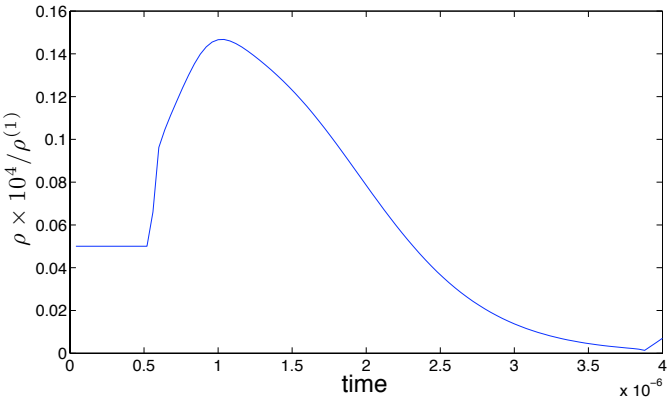

(b) $x = 11mm$

Figure 4.4: **Experiment 4** Solution (normalized density) plotted against time at the indicated distance from the strike zone, computed on grid with $\Delta x = 5 \times 10^{-5}$ m.

in (4.51), we see that the unnatural value for the relaxation parameter results in a solution that is less than appealing.

Chapter 5

Two-Dimensional Laser Ablation

5.1 Mathematical Model

In this section we present the two-dimensonal (2D) QGD system of equations. It is noted that the computation of this model had not ever been done before. The 2D simulation provides insight into the full three-dimensional (3D) simulation. The 2D simulation ignores the direction orthogonal to the workpiece which greatly simplifies the equations that need to be solved. By ignoring this vertical direction we are ignoring the heat transfer that takes place at the strike zone between the energy of the laser and the workpiece. By assuming that all of this energy is available for the expansion, we are simplifying the dynamics of the expansion of the plasma. The full 3D simulation would give a much better and physically realistic representation of the physical problem.

The gas is described by its density ρ, velocity components $\mathbf{q} = (u, v)^T$, and energy E. The total energy per unit volume E is calculated using the equation of state given in equation (1.48), and the total specific enthalpy H is calculated by $H = (E + p)/\rho$. The QGD equations are given below.

$$\frac{\partial \rho}{\partial t} + \frac{\partial j^{(x)}}{\partial x} + \frac{\partial j^{(y)}}{\partial y} = 0, \tag{5.1}$$

$$\frac{\partial (\rho u)}{\partial t} + \frac{\partial (j^{(x)} u)}{\partial x} + \frac{\partial (j^{(y)} u)}{\partial y} + \frac{\partial p}{\partial x} = \frac{\partial \Pi^{(xx)}}{\partial x} + \frac{\partial \Pi^{(yx)}}{\partial y}, \tag{5.2}$$

$$\frac{\partial (\rho v)}{\partial t} + \frac{\partial (j^{(x)} v)}{\partial x} + \frac{\partial (j^{(y)} v)}{\partial y} + \frac{\partial p}{\partial y} = \frac{\partial \Pi^{(xy)}}{\partial x} + \frac{\partial \Pi^{(yy)}}{\partial y}, \tag{5.3}$$

$$\frac{\partial E}{\partial t} + \frac{\partial (j^{(x)} H)}{\partial x} + \frac{\partial (j^{(y)} H)}{\partial y} + \frac{\partial q^{(x)}}{\partial x} + \frac{\partial q^{(y)}}{\partial y} = \frac{\partial}{\partial x}\left(\Pi^{(xx)} u + \Pi^{(xy)} v\right) + \frac{\partial}{\partial y}\left(\Pi^{(yx)} u + \Pi^{(yy)} v\right). \tag{5.4}$$

The terms $j^{(x)}$ and $j^{(y)}$ represent the transport of density in the x and y directions averaged over time. They are given by the formuals,

$$j^{(x)} = \rho(u - w^{(x)}), \quad w^{(x)} = \frac{\tau}{\rho}\left[\frac{\partial(\rho u^2)}{\partial x} + \frac{\partial(\rho uv)}{\partial y} + \frac{\partial p}{\partial x}\right], \tag{5.5}$$

$$j^{(y)} = \rho(v - w^{(y)}), \quad w^{(y)} = \frac{\tau}{\rho}\left[\frac{\partial(\rho uv)}{\partial x} + \frac{\partial(\rho v^2)}{\partial y} + \frac{\partial p}{\partial y}\right]. \tag{5.6}$$

Again, the relaxation parameter τ is present to control these extra diffusive terms. The components of the viscosity tensor are given below.

$$\Pi^{(xx)} = \eta\left(2\frac{\partial u}{\partial x} - \left[\frac{2}{3} - \frac{\zeta}{\eta}\right]\text{div }\vec{u}\right) + \tau\gamma p \text{ div } \vec{u} + \tau\rho u\left(u\frac{\partial u}{\partial x} + v\frac{\partial u}{\partial y}\right) + \tau\left(2u\frac{\partial p}{\partial x} + v\frac{\partial p}{\partial y}\right) \tag{5.7}$$

$$\Pi^{(xy)} = \eta\left(\frac{\partial v}{\partial x} + \frac{\partial u}{\partial y}\right) + \tau\rho u\left(u\frac{\partial v}{\partial x} + v\frac{\partial v}{\partial y} + \frac{1}{\rho}\frac{\partial p}{\partial y}\right) \tag{5.8}$$

$$\Pi^{(yx)} = \eta\left(\frac{\partial u}{\partial y} + \frac{\partial v}{\partial x}\right) + \tau\rho v\left(u\frac{\partial u}{\partial x} + v\frac{\partial u}{\partial y} + \frac{1}{\rho}\frac{\partial p}{\partial x}\right) \tag{5.9}$$

$$\Pi^{(yy)} = \eta\left(2\frac{\partial v}{\partial y} - \left[\frac{2}{3} - \frac{\zeta}{\eta}\right]\text{div }\vec{u}\right) + \tau\gamma p \text{ div } \vec{u} + \tau\rho v\left(u\frac{\partial v}{\partial x} + v\frac{\partial v}{\partial y}\right) + \tau\left(u\frac{\partial p}{\partial x} + 2v\frac{\partial p}{\partial y}\right) \tag{5.10}$$

Finally, the heat flux is given by

$$q^{(x)} = -\kappa\frac{\partial T}{\partial x} - u \cdot R^q \tag{5.11}$$

$$q^{(y)} = -\kappa\frac{\partial T}{\partial y} - v \cdot R^q, \tag{5.12}$$

where

$$R^q = \tau\rho\frac{1}{\gamma - 1}\left[u\frac{\partial}{\partial x}\left(\frac{p}{\rho}\right) + v\frac{\partial}{\partial y}\left(\frac{p}{\rho}\right)\right] + \tau\rho p\left[u\frac{\partial}{\partial x}\left(\frac{1}{\rho}\right) + v\frac{\partial}{\partial y}\left(\frac{1}{\rho}\right)\right]. \tag{5.13}$$

Note that the viscous stress tensor and heat flux can be written with the respective terms from Navier-Stokes' equations, which differs from these equations by the presence of the relaxation parameter τ. In fact, as $\tau \to 0$ we are left with the Navier-Stokes equations (see equations (1.38)-(1.41)).

The coefficients for dynamic viscosity η, thermal conductivity κ, and bulk viscosity ζ, are

related to the relaxation parameter τ. These are given below:

$$\tau = \alpha \frac{\min(\Delta x, \Delta y)}{c_s}, \tag{5.14}$$

$$\alpha = 0.3, \quad c_s = (\gamma R T_2)^{\frac{1}{2}}, \tag{5.15}$$

$$\eta = \tau p \mathrm{Sc}, \tag{5.16}$$

$$\zeta = \tau p \left(\frac{5}{3} - \gamma \right), \tag{5.17}$$

$$\kappa = \frac{\eta \gamma R}{\mathrm{Pr}(\gamma - 1)}. \tag{5.18}$$

Now we would like to rearrange the terms in (5.1) - (5.4) so the left-hand side is the Euler's equations and the diffusive terms are on the right. This is done by expanding the j terms.

Equation (5.1)

The equation is repeated below for convenience.

$$\frac{\partial \rho}{\partial t} + \frac{\partial j^{(x)}}{\partial x} + \frac{\partial j^{(y)}}{\partial y} = 0, \tag{5.19}$$

Expanding $j^{(x)}$ and $j^{(y)}$ and combining like derivatives gives us

$$\frac{\partial \rho}{\partial t} + \frac{\partial (\rho u)}{\partial x} + \frac{\partial (\rho v)}{\partial y} = \frac{\partial}{\partial x}\left[\tau \left(\frac{\partial (\rho u^2 + p)}{\partial x} + \frac{\partial (\rho u v)}{\partial y} \right)\right] + \frac{\partial}{\partial y}\left[\tau \left(\frac{\partial (\rho u v)}{\partial x} + \frac{\partial (\rho v^2 + p)}{\partial y} \right)\right]. \tag{5.20}$$

Equation (5.2)

The equation is repeated below for convenience.

$$\frac{\partial (\rho u)}{\partial t} + \frac{\partial (j^{(x)} u)}{\partial x} + \frac{\partial (j^{(y)} u)}{\partial y} + \frac{\partial p}{\partial x} = \frac{\partial \Pi^{(xx)}}{\partial x} + \frac{\partial \Pi^{(yx)}}{\partial y}. \tag{5.21}$$

Again, expanding $j^{(x)}$ and $j^{(y)}$ and combining like derivatives gives us the following.

$$\begin{aligned} \frac{\partial (\rho u)}{\partial t} + \frac{\partial (\rho u^2 + p)}{\partial x} + \frac{\partial (\rho u v)}{\partial y} = {} & \frac{\partial}{\partial x}\left[\tau u \left(\frac{\partial (\rho u^2 + p)}{\partial x} + \frac{\partial (\rho u v)}{\partial y} \right)\right] \\ & + \frac{\partial}{\partial y}\left[\tau u \left(\frac{\partial (\rho u v)}{\partial x} + \frac{\partial (\rho v^2 + p)}{\partial y} \right)\right] + \frac{\partial \Pi^{(xx)}}{\partial x} + \frac{\partial \Pi^{(yx)}}{\partial y}. \end{aligned} \tag{5.22}$$

The viscous stress tensors are written as

$$\frac{\partial \Pi^{(xx)}}{\partial x} = \frac{\partial}{\partial x}\left[\left(2\eta - \beta\eta + \tau\gamma p + \tau\rho u^2\right) u_x + \left(-\beta\eta + \tau\gamma p\right) v_y + \left(\tau\rho uv\right) u_y + (2\tau u) p_x + (\tau v) p_y\right], \tag{5.23}$$

$$\frac{\partial \Pi^{(yx)}}{\partial y} = \frac{\partial}{\partial y}\left[(\tau\rho uv) u_x + (\eta + \tau\rho v^2) u_y + \eta v_x + (\tau v) p_x\right]. \tag{5.24}$$

Note that above and in the following the subscript notation refers to partial derivatives. E.g., $u_x = \frac{\partial u}{\partial x}$. Also, for simplicity of notation $\beta = \left[\frac{2}{3} - \frac{\zeta}{\eta}\right]$.

Equation (5.3)

The derivation here is similar to that for equation (5.2).

$$\frac{\partial(\rho v)}{\partial t} + \frac{\partial(j^{(x)} v)}{\partial x} + \frac{\partial(j^{(y)} v)}{\partial y} + \frac{\partial p}{\partial y} = \frac{\partial \Pi^{(xy)}}{\partial x} + \frac{\partial \Pi^{(yy)}}{\partial y}. \tag{5.25}$$

Again, expanding $j^{(x)}$ and $j^{(y)}$ and combining like derivatives gives us the following.

$$\begin{aligned}\frac{\partial(\rho v)}{\partial t} + \frac{\partial(\rho uv)}{\partial x} + \frac{\partial(\rho v^2 + p)}{\partial y} = {} & \frac{\partial}{\partial x}\left[\tau v\left(\frac{\partial(\rho u^2 + p)}{\partial x} + \frac{\partial(\rho uv)}{\partial y}\right)\right] \\ & + \frac{\partial}{\partial y}\left[\tau v\left(\frac{\partial(\rho uv)}{\partial x} + \frac{\partial(\rho v^2 + p)}{\partial y}\right)\right] + \frac{\partial \Pi^{(xy)}}{\partial x} + \frac{\partial \Pi^{(yy)}}{\partial y}.\end{aligned} \tag{5.26}$$

The viscous stress tensors are written as

$$\frac{\partial \Pi^{(xy)}}{\partial x} = \frac{\partial}{\partial x}\left[(\eta + \tau\rho u^2) v_x + (\tau\rho uv) v_y + \eta u_y + (\tau u) p_y\right], \tag{5.27}$$

$$\frac{\partial \Pi^{(yy)}}{\partial y} = \frac{\partial}{\partial y}\left[\left(2\eta - \beta\eta + \tau\gamma p + \tau\rho v^2\right) v_y + \left(-\beta\eta + \tau\gamma p\right) u_x + \left(\tau\rho uv\right) v_x + (\tau u) p_x + (2\tau v) p_y\right]. \tag{5.28}$$

Equation (5.4)

The equation is repeated below for convenience.

$$\frac{\partial E}{\partial t} + \frac{\partial(j^{(x)} H)}{\partial x} + \frac{\partial(j^{(y)} H)}{\partial y} + \frac{\partial q^{(x)}}{\partial x} + \frac{\partial q^{(y)}}{\partial y} = \frac{\partial}{\partial x}\left(\Pi^{(xx)} u + \Pi^{(xy)} v\right) + \frac{\partial}{\partial y}\left(\Pi^{(yx)} u + \Pi^{(yy)} v\right). \tag{5.29}$$

First note that

$$j^{(x)}H = (E+p)u - (E+p)w^{(x)}, \tag{5.30}$$

$$j^{(y)}H = (E+p)v - (E+p)w^{(y)}. \tag{5.31}$$

Recall that the total enthaply is given by $H = (E+p)/\rho$. Expanding $j^{(x)}$ and $j^{(y)}$ and combining like derivatives gives us

$$\begin{aligned}\frac{\partial E}{\partial t} + \frac{\partial\left((E+p)u\right)}{\partial x} + \frac{\partial\left((E+p)v\right)}{\partial y} &= \frac{\partial}{\partial x}\left((E+p)w^{(x)}\right) + \frac{\partial}{\partial y}\left((E+p)w^{(y)}\right) \\ &+ \frac{\partial}{\partial x}\left(-q^{(x)}\right) + \frac{\partial}{\partial y}\left(-q^{(y)}\right) \\ &+ \frac{\partial}{\partial x}\left(\Pi^{(xx)}u + \Pi^{(xy)}v\right) + \frac{\partial}{\partial y}\left(\Pi^{(yx)}u + \Pi^{(yy)}v\right). \end{aligned} \tag{5.32}$$

The terms of the right-hand side are expanded as follows.

$$\frac{\partial}{\partial x}\left((E+p)w^{(x)}\right) = \frac{\partial}{\partial x}\left(\tau H(\rho u^2 + p)_x + \tau H(\rho uv)_y\right), \tag{5.33}$$

$$\frac{\partial}{\partial y}\left((E+p)w^{(y)}\right) = \frac{\partial}{\partial y}\left(\tau H(\rho uv)_x + \tau H(\rho v^2 + p)_y\right). \tag{5.34}$$

Recalling equation (5.13), we get for the heat fluxes

$$\begin{aligned}\frac{\partial}{\partial x}\left(-q^{(x)}\right) &= \frac{\partial}{\partial x}\left[\kappa T_x + uR\right] \\ &= \frac{\partial}{\partial x}\left[\kappa T_x + \frac{\tau\rho u^2}{\gamma-1}\left(\frac{p}{\rho}\right)_x + \frac{\tau\rho uv}{\gamma-1}\left(\frac{p}{\rho}\right)_y + \tau\rho u^2 p\left(\frac{1}{\rho}\right)_x + \tau\rho uvp\left(\frac{1}{\rho}\right)_y\right]. \end{aligned} \tag{5.35}$$

$$\begin{aligned}\frac{\partial}{\partial y}\left(-q^{(y)}\right) &= \frac{\partial}{\partial y}\left[\kappa T_y + vR\right] \\ &= \frac{\partial}{\partial y}\left[\kappa T_y + \frac{\tau\rho uv}{\gamma-1}\left(\frac{p}{\rho}\right)_x + \frac{\tau\rho v^2}{\gamma-1}\left(\frac{p}{\rho}\right)_y + \tau\rho uvp\left(\frac{1}{\rho}\right)_x + \tau\rho v^2 p\left(\frac{1}{\rho}\right)_y\right]. \end{aligned} \tag{5.36}$$

Finally, the advection of viscosity is given by the following.

$$\frac{\partial}{\partial x}\left(\Pi^{(xx)}u\right) = \frac{\partial}{\partial x}\left[(2\eta u - \beta\eta u + \tau\gamma pu + \tau\rho u^3)u_x + (-\beta\eta u + \tau\gamma pu)v_y \right. \\ \left. +(\tau\rho u^2 v)u_y + (2\tau u^2)p_x + (\tau uv)p_y\right], \tag{5.37}$$

$$\frac{\partial}{\partial x}\left(\Pi^{(xy)}v\right) = \frac{\partial}{\partial x}\left[(\eta v + \tau\rho u^2 v)v_x + (\tau\rho uv^2)v_y + (\eta v)u_y + (\tau uv)p_y\right], \tag{5.38}$$

$$\frac{\partial}{\partial y}\left(\Pi^{(yx)}u\right) = \frac{\partial}{\partial y}\left[(\tau\rho u^2 v)u_x + (\eta u + \tau\rho uv^2)u_y + (\eta u)v_x + (\tau uv)p_x\right], \tag{5.39}$$

$$\frac{\partial}{\partial y}\left(\Pi^{(yy)}v\right) = \frac{\partial}{\partial y}\left[(2\eta v - \beta\eta v + \tau\gamma pv + \tau\rho v^3)v_y + (-\beta\eta v + \tau\gamma pv)u_x \right. \\ \left. +(\tau\rho uv^2)v_x + (\tau uv)p_x + (2\tau v^2)p_y\right]. \tag{5.40}$$

5.2 Numerics

In this section, we briefly describe a two-dimensional version of the second-order central-upwind scheme used to numerically solve the two-dimensional QGD equations.

$$\mathbf{u}_t + \mathbf{F}(\mathbf{u})_x + \mathbf{G}(\mathbf{u})_y = \mathbf{D}^{(x)}(\mathbf{u}) + \mathbf{D}^{(y)}(\mathbf{u}). \tag{5.41}$$

Here, $\mathbf{u}$ is the unknown vector of conservative variables, $\mathbf{F}$ represents the the convective nonlinear flux in the x direction and $\mathbf{G}$ represents the the convective nonlinear flux in the y direction. The parabolic diffusion in the x and y directions are represented by $\mathbf{D}^{(x)}$ and $\mathbf{D}^{(y)}$. These vectors are given below.

$$\mathbf{u} = \begin{pmatrix} \rho \\ \rho u \\ \rho v \\ E \end{pmatrix}, \quad \mathbf{F} = \begin{pmatrix} \rho u \\ \rho u^2 + p \\ \rho uv \\ (E+p)u \end{pmatrix}, \quad \mathbf{G} = \begin{pmatrix} \rho v \\ \rho uv \\ \rho v^2 + p \\ (E+p)v \end{pmatrix}, \tag{5.42}$$

$$\mathbf{D}^{(x)}(\mathbf{u}) = \begin{pmatrix} \tau\left(\frac{\partial(\rho u^2+p)}{\partial x} + \frac{\partial(\rho uv)}{\partial y}\right) \\ \tau u\left(\frac{\partial(\rho u^2+p)}{\partial x} + \frac{\partial(\rho uv)}{\partial y}\right) + \Pi^{(xx)} \\ \tau v\left(\frac{\partial(\rho u^2+p)}{\partial x} + \frac{\partial(\rho uv)}{\partial y}\right) + \Pi^{(xy)} \\ (E+p)w^{(x)} - q^{(x)} + \Pi^{(xx)}u + \Pi^{(xy)}v \end{pmatrix}, \tag{5.43}$$

$$\mathbf{D}^{(y)}(\mathbf{u}) = \begin{pmatrix} \tau\left(\frac{\partial(\rho uv)}{\partial x} + \frac{\partial(\rho v^2+p)}{\partial y}\right) \\ \tau u\left(\frac{\partial(\rho uv)}{\partial x} + \frac{\partial(\rho v^2+p)}{\partial y}\right) + \Pi^{(yx)} \\ \tau v\left(\frac{\partial(\rho uv)}{\partial x} + \frac{\partial(\rho v^2+p)}{\partial y}\right) + \Pi^{(yy)} \\ (E+p)w^{(y)} - q^{(y)} + \Pi^{(yx)}u + \Pi^{(yy)}v \end{pmatrix}. \tag{5.44}$$

In the following discussion we consider (for simplicity) a uniform two-dimensional spatial grid of size Δx and Δy in the x and y directions, respectively. The grid points are given by (x_j, y_k), where we use the notation: $x_j = j\Delta x,\ x_{j\pm\frac{1}{2}} = (j \pm \frac{1}{2})\Delta x$ and $y_k = k\Delta y,\ y_{k\pm\frac{1}{2}} = (k \pm \frac{1}{2})\Delta y$. According to the two -dimensional central-upwind approach, the computed solution is realized at each time t in terms of cell averages,

$$\overline{\mathbf{u}}_{j,k}(t) = \frac{1}{\Delta x \Delta y} \int\limits_{x_{j-\frac{1}{2}}}^{x_{j+\frac{1}{2}}} \int\limits_{y_{k-\frac{1}{2}}}^{y_{k+\frac{1}{2}}} \mathbf{u}(x, y, t)\, dxdy, \tag{5.45}$$

which are evolved in time by solving the following system of ODEs:

$$\begin{aligned} \frac{d}{dt}\overline{\mathbf{u}}_j(t) = &- \frac{\mathbf{H}^x_{j+\frac{1}{2},k}(t) - \mathbf{H}^x_{j-\frac{1}{2},k}(t)}{\Delta x} - \frac{\mathbf{H}^y_{j,k+\frac{1}{2}}(t) - \mathbf{H}^y_{j,k-\frac{1}{2}}(t)}{\Delta y} \\ &+ \frac{\mathbf{P}^x_{j+\frac{1}{2},k}(t) - \mathbf{P}^x_{j-\frac{1}{2},k}(t)}{\Delta x} + \frac{\mathbf{P}^y_{j,k+\frac{1}{2}}(t) - \mathbf{P}^y_{j,k-\frac{1}{2}}(t)}{\Delta y}, \end{aligned} \tag{5.46}$$

where the hyperbolic $\mathbf{H}^x_{j+\frac{1}{2},k}$, $\mathbf{H}^y_{j,k+\frac{1}{2}}$ and parabolic $\mathbf{P}^x_{j+\frac{1}{2},k}$, $\mathbf{P}^y_{j,k+\frac{1}{2}}$ numerical fluxes are constructed as follows.

Hyperbolic Flux

In order to compute the hyperbolic fluxes, $\mathbf{H}^x_{j+\frac{1}{2},k}$ and $\mathbf{H}^y_{j,k+\frac{1}{2}}$, we first use the cell averages (5.45) to reconstruct a conservative second-order piecewise linear interpolant:

$$\widetilde{\mathbf{u}}(x, y) = \overline{\mathbf{u}}_{j,k} + (\mathbf{u}_x)_{j,k}(x - x_j) + (\mathbf{u}_y)_{j,k}(y - y_k), \quad x \in [x_{j-\frac{1}{2}}, x_{j+\frac{1}{2}}] \times [y_{k-\frac{1}{2}}, y_{k+\frac{1}{2}}], \tag{5.47}$$

where the slopes in the reconstruction are computed using the generalized minmod reconstruction given in (1.101).

The hyperbolic numerical fluxes are then computed according to the formulas given in

(1.109) and (1.110), which are repeated below for our convenience.

$$\mathbf{H}^x_{j+\frac{1}{2},k}(t) = \frac{a^+_{j+\frac{1}{2},k}\mathbf{F}\left(\mathbf{u}^E_{j,k}\right) - a^-_{j+\frac{1}{2},k}\mathbf{F}\left(\mathbf{u}^W_{j+1,k}\right)}{a^+_{j+\frac{1}{2},k} - a^-_{j+\frac{1}{2},k}} + \frac{a^+_{j+\frac{1}{2},k}a^-_{j+\frac{1}{2},k}}{a^+_{j+\frac{1}{2},k} - a^-_{j+\frac{1}{2},k}}\left[\mathbf{u}^W_{j+1,k} - \mathbf{u}^E_{j,k}\right], \tag{5.48}$$

$$\mathbf{H}^y_{j,k+\frac{1}{2}}(t) = \frac{b^+_{j,k+\frac{1}{2}}\mathbf{G}\left(\mathbf{u}^N_{j,k}\right) - b^-_{j,k+\frac{1}{2}}\mathbf{G}\left(\mathbf{u}^S_{j,k+1}\right)}{b^+_{j,k+\frac{1}{2}} - b^-_{j,k+\frac{1}{2}}} + \frac{b^+_{j,k+\frac{1}{2}}b^-_{j,k+\frac{1}{2}}}{b^+_{j,k+\frac{1}{2}} - b^-_{j,k+\frac{1}{2}}}\left[\mathbf{u}^S_{j,k+1} - \mathbf{u}^N_{j,k}\right]. \tag{5.49}$$

The point values of the piecewise linear reconstruction are denoted by $\mathbf{u}^E_{j,k}$, $\mathbf{u}^W_{j,k}$, $\mathbf{u}^N_{j,k}$, and $\mathbf{u}^S_{j,k}$. The letters correspond to the direction the point value is taken at. E.g., the point values directly east and north from (j,k) are given by

$$\mathbf{u}^E_{j,k} = \overline{\mathbf{u}}_{j,k} + \frac{\Delta x}{2}(\mathbf{u}_x)_{j,k}, \tag{5.50}$$

$$\mathbf{u}^N_{j,k} = \overline{\mathbf{u}}_{j,k} + \frac{\Delta y}{2}(\mathbf{u}_y)_{j,k}. \tag{5.51}$$

The local speeds in the x direction are given by $a^\pm_{j+\frac{1}{2},k}$, and are obtained from the largest and smallest eigenvalues of the Jacobian $\frac{\partial \mathbf{F}}{\partial \mathbf{u}}$ and can be estimated by

$$a^+_{j+\frac{1}{2},k} = \max\left\{u^W_{j+1,k} + c^W_{j+1,k}, u^E_{j,k} + c^E_{j,k}, 0\right\}, \quad a^-_{j+\frac{1}{2},k} = \min\left\{u^W_{j+1,k} - c^W_{j+1,k}, u^E_{j,k} - c^E_{j,k}, 0\right\}, \tag{5.52}$$

where u is the macroscopic velocity in the x direction and $c = \sqrt{\frac{\gamma p}{\rho}}$ is the speed of sound. Note, e.g., $c^E_{j,k}$ is the sound speed evaluated at $\mathbf{u}^E_{j,k}$. The local speeds in the y direction are given by $b^\pm_{j,k+\frac{1}{2}}$, and are obtained from the largest and smallest eigenvalues of the Jacobian $\frac{\partial \mathbf{G}}{\partial \mathbf{u}}$ and can be estimated by

$$b^+_{j,k+\frac{1}{2}} = \max\left\{v^S_{j,k+1} + c^S_{j,k+1}, v^N_{j,k} + c^N_{j,k}, 0\right\}, \quad b^-_{j,k+\frac{1}{2}} = \min\left\{v^S_{j,k+1} - c^S_{j,k+1}, v^N_{j,k} - c^N_{j,k}, 0\right\}, \tag{5.53}$$

where v is the macroscopic velocity in the y direction.

Parabolic Flux

The parabolic numerical fluxes in the x direction are represented by

$$\frac{\mathbf{P}_{j+\frac{1}{2},k}(t) - \mathbf{P}_{j-\frac{1}{2},k}(t)}{\Delta x}, \tag{5.54}$$

while the fluxes in the y direction are represented by

$$\frac{\mathbf{P}_{j,k+\frac{1}{2}}(t) - \mathbf{P}_{j,k-\frac{1}{2}}(t)}{\Delta y}. \tag{5.55}$$

To compute the parabolic numerical fluxes we first notice that the diffusion terms can be written as linear combinations of the form $(VW_x)_x$. E.g., in equation (5.22) letting $V = \tau u$ and $W = \rho u^2 + p$.

There are four types of derivatives that need to be considered. They are,

1. $(VW_x)_x$
2. $(VW_y)_x$
3. $(VW_x)_y$
4. $(VW_y)_y$

Terms such as (1) and (2) are discretized using (5.54), while (3) and (4) are discretized using (5.55). For (1) and, the parabolic numerical flux is given by

$$P_{j+\frac{1}{2},k} = V_{j+\frac{1}{2},k}\left(\frac{\overline{W}_{j+1,k} - \overline{W}_{j,k}}{\Delta x}\right), \tag{5.56}$$

where $V_{j+\frac{1}{2},k}$ is the average of the point values evaluated on either side of the flux boundary and $\overline{W}_{j,k}$ is evaluated at the cell average $\overline{u}_{j,k}$. The mixed derivatives are more complicated. For (2) we can use a centered difference at the flux boundary. I.e.,

$$P_{j+\frac{1}{2},k} = V_{j+\frac{1}{2},k}\left(\frac{W_{j+\frac{1}{2},k+1} - W_{j+\frac{1}{2},k-1}}{2\Delta y}\right). \tag{5.57}$$

The values $W_{j+\frac{1}{2},k+1}$ are computed as averages of the point values at the flux boundaries.

The parabolic numerical flux for (4) is given by

$$P_{j,k+\frac{1}{2}} = V_{j,k+\frac{1}{2}}\left(\frac{\overline{W}_{j,k+1} - \overline{W}_{j,k}}{\Delta y}\right). \tag{5.58}$$

The mixed derivative in (3) is handled similarly to (5.57). I.e.,

$$P_{j,k+\frac{1}{2}} = V_{j,k+\frac{1}{2}}\left(\frac{W_{j+1,k+\frac{1}{2}} - W_{j-1,k+\frac{1}{2}}}{2\Delta x}\right). \tag{5.59}$$

5.3 Numerical Experiments

In this section we present results for two-dimensional single-gas problem. Again, we model the expansion of plasma as a carbon-jet expanding into a vacuum. In the two-dimensional problem, the plasma expands as a high-pressure, high-temperature front in both the x and y directions. It is noted that this is the first time that computation of the two-dimensional laser ablation problem using the QGD equations has been carried out. This has been accomplished by implementing the high-resolution finite volume method coupled with an efficient ODE solver. The two-dimensional expansion is computationally expensive and the ability to freely run simulations is not as convenient as in the one-dimensional case. We hope that steps taken to optimize the code make a thorough numerical investigation possible. Among these steps is the reduction in the number of arrays used.

The QGD model is able to supress the numerical stability issues that arise in the application of the NS equations to this problem. It is noted that the scheme applied to the NS simulation of the two-dimensional laser ablation problem was not able to produce results. This is due to the lack of numerical stability available in the numerical approximation of the NS diffusion. Again, the extra smoothing provided by the temporal averaging in the QGD equations provides usable results. The scheme's ability to accurately and efficiently capture the shock behavior allow for a realistic approximation of the plasma expansion. In fact, the plots of he results show a remarkable simulation of the plasma expansion.

The schematic in Figure 5.1 gives the set-up for the two-dimensional laser ablation problem. The initial velocity is zero everywhere, i.e. $\mathbf{u} = 0$. The initial conditions for pressure and temperature are given below.

$$p_1 = 10^8 \text{Pa}, \quad T_1 = 5 \times 10^4 \text{ K} \tag{5.60}$$

$$p_2 = 10^3 \text{Pa}, \quad T_2 = 300 \text{ K} \tag{5.61}$$

Under consideration is the spread of the plasma of molecular carbon C_2 in a vacuum. Carbon has constant parameters $R = 346.25$, $\gamma = 7/5$, $\omega = 0.74$, $Pr = 14/19$ and $Sc = 0.746$.

The calculation domain is taken to be the square given by $0 \leq x \leq L_x = 0.02$ m and $0 \leq y \leq L_y = 0.02$ m. After the laser pulse, at $t = 0$, there is a small ellipse where the strike results in a high-pressure and high-temperature region. The dimensions of the ellipse are given by $x_{00} = 5.45 \times 10^{-5}$ m and $y_{00} = 2.52 \times 10^{-4}$ m. It should be noted that the size of the strike zone here is on an order of magnitude bigger than that of the one-dimensional setup. This is in fact a quite benevolent situation for the numerical scheme since it allows for a reasonable mesh size. Recall that the mesh size was directly dependent on the size of the strike zone, because we needed to pick up the initial data in the strike zone in at least one cell.

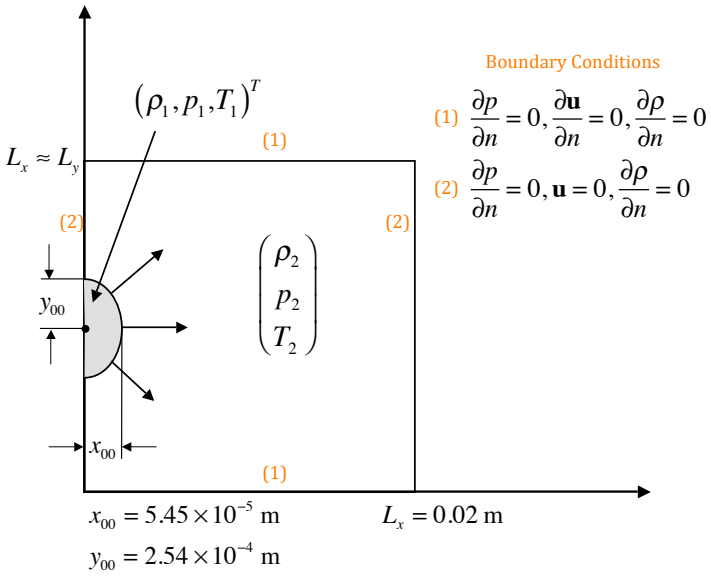

Figure 5.1: Two-dimensional Initial Conditions

The evaporation can be separated into three regimes: the evaporation of the target material, the interaction of the evaporated material with the laser beam resulting in the plasma formation, and the expansion of the plasma [109]. The simulation produced here models the third regime by using gas dynamic equations with appropriate initial conditions. Since the dynamics are being modeled by equations of fluid flow, the velocities of the outward expansion are driven by the pressure gradients of the plasma. The expansion of the plasma is outward along the top of the substrate.

After the initial blast, the model represents a high density, high temperature gas which is contained in a narrow region that is then allowed to expand into a vacuum. Figure 5.2 shows the density of the gas immediately after the nano-second laser pulse. In the two-dimensional set-up we witness a symmetric-like expansion as the energy from the laser transforms the evaporated target material into a plasma. The subsequent deposition of a thin film occurs as the collective motion of the ions and electrons race outward driven by the force of the laser explosion [61].

Figure 5.3 shows the density at the final time, $t = t_f = 4\mu$s. Here we clearly see the front of the expansion as the molecules rush outward. The density drops behind the expansion front as the molecules are carried outward by the velocity of the expansion. Figure 5.4 show the top view of the expansion. Figure (a) shows the density of the gas at $t = 2\mu$s, while Figure (b) shows the expansion at $t = t_f = 4\mu$s. Here we see the concentration of the molecules in a narrow region along the outer boundary of the expansion, and we also see the dynamics of the expansion play out. In these figures we see that the expansion length is elongated out in the x

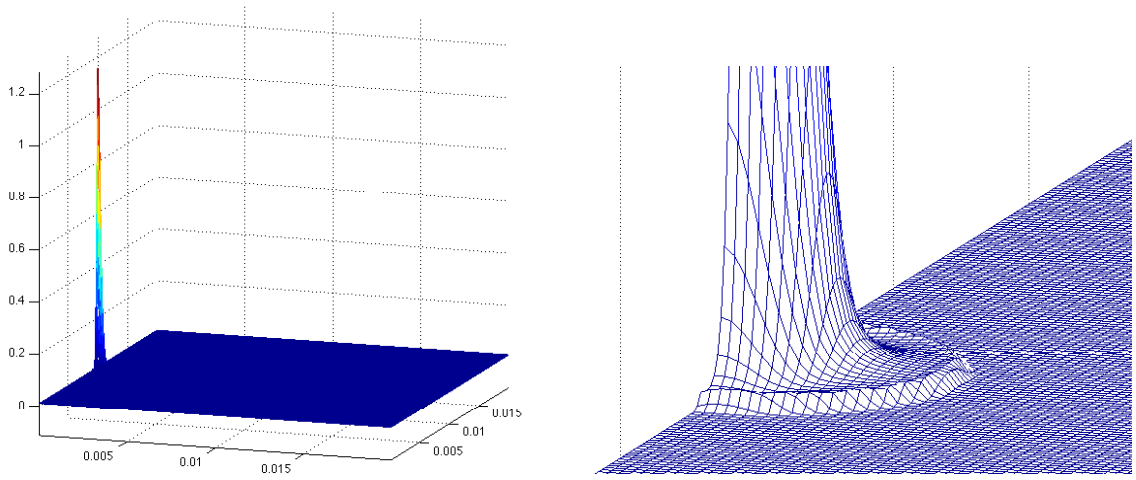

(a) Full domain view

(b) Zoom in on strike zone

Figure 5.2: Solution (density) plotted against the 2D spatial grid immediately after ($t = 0.02\mu$s) the nano-second laser pulse. Plot (a) shows the full picture. Plot (b) is an extreme zoom in to the strike zone

direction. This due to the velocities being dictated by the lengths of the initial configuration of the gas, [109]. The larger velocities occur in the direction of the smaller dimension, in this case the x direction (see Figure 5.1). Figure 5.5 shows the magnitude of the velocities in the x and y directions, Figures (a) and (b) respectively. Figure 5.6 is the top view of the pressure, which is nearly identical to the expansion of density. The symmetry we see in these graphs is expected since the initial conditions were symmetric. If there were, say, a gradient in the initial pressure, we would see this evolve as a non-symmetric solution.

The two-dimensional model gives a much better physical interpretation of the dynamics of the problem than does the one-dimensional view. In particular, we are able to see the elongation of the expansion which match observations of physical experiments. Although the two-dimensional simulation is computationally expensive, the ability to model this problem allows for the continued advancement of the study of this problem and is hopefully a significant step towards a full three-dimensional version.

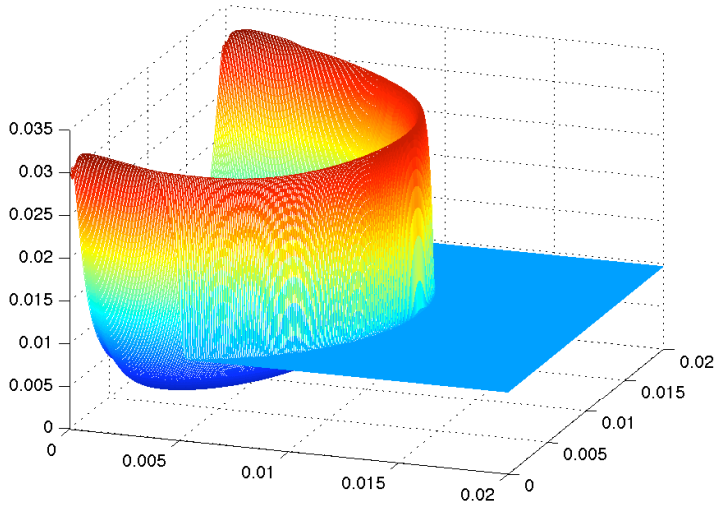

Figure 5.3: Solution (density) plotted against the 2D spatial grid at $t = 4\mu$s

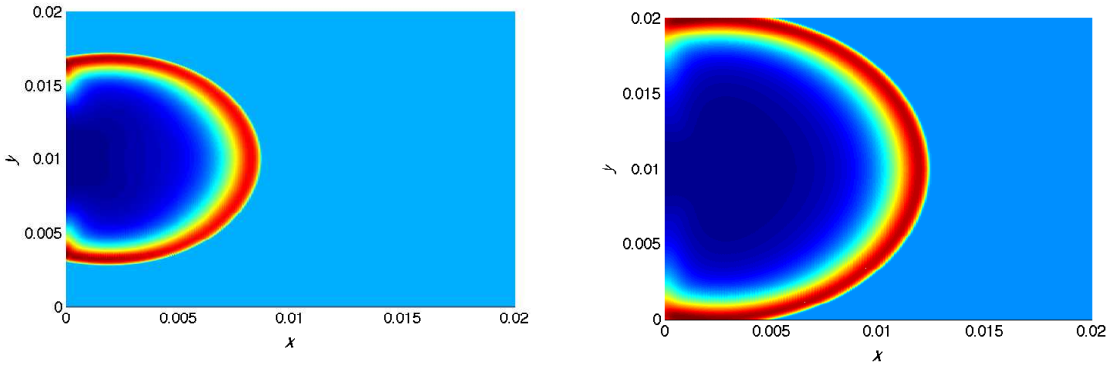

(a) Front View

(b) Back View

Figure 5.4: Solution (density) plotted against the 2D spatial grid at $t = 2\mu$s and $t = 4\mu$s

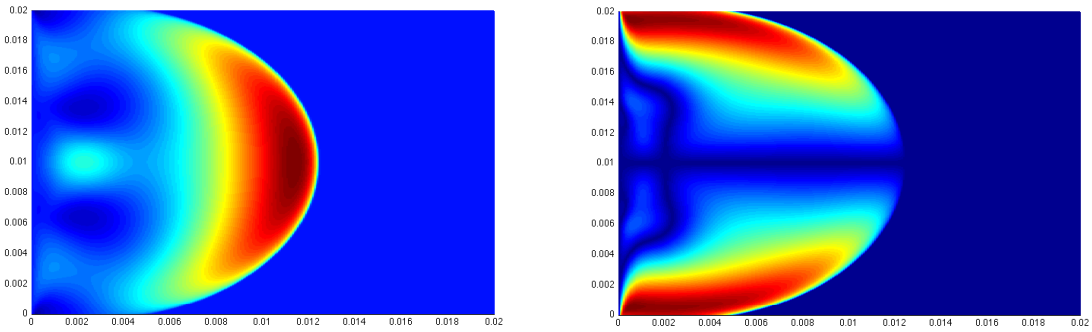

(a) Velocity in the x-direction

(b) Velocity in the y-direction

Figure 5.5: Solution (velocity) plotted against the 2D spatial grid at $t = 4\mu$s: in x and y directions

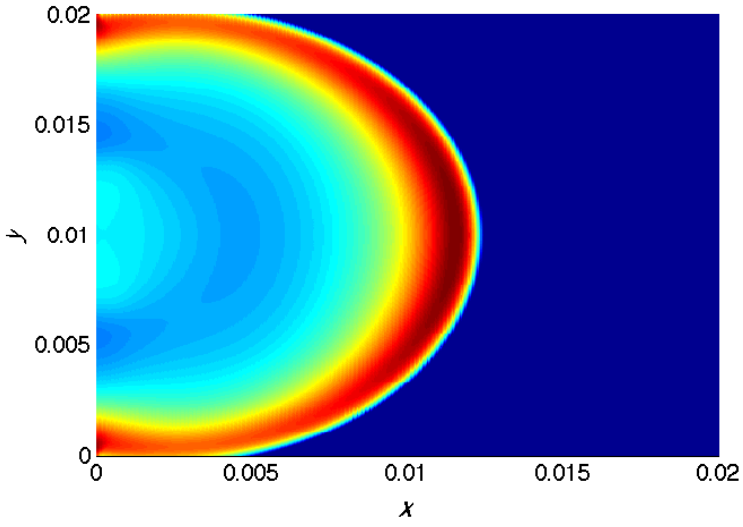

Figure 5.6: Solution (pressure) plotted against the 2D spatial grid at $t = 4\mu$s

Chapter 6

Conclusion

The results of this study show that the computer simulation of the expansion of a plasma jet formed by the pulsed laser evaporation of a graphite target can be efficiently modeled by the quasi-gas dynamic (QGD) equations. The numerical method employed here allows for the accurate modeling of the plasma expansion by considering the plasma as a gas that flows under the equations of fluid dynamics. In fact, the numerical method's ability to accurately and efficiently capture the propagation of the shock-like front even allows for the modeling of the problem to be carried out using the Navier-Stokes (NS) equations. This had not been achievable previously, due to the stability issues that arise in the numerical evaluation of the NS equations with the initial configuration as is for the problem being studied. Furthermore, the efficiency gained allows for the application of the QGD equations to the two-dimensional problem. This too had previously not been calculated. Other numerical methods previously used to solve the problem, such as direct numerical simulations using Monte Carlo methods and, in particular, finite difference methods required enormous computational effort. For example, the one-dimensional problem which was solved numerically using a finite difference method in [72] required a spatial mesh with $45,000$ nodes. Two carry out this simulation in two dimensions would require a $45,000 \times 45,000$ grid, which easily overwhelms computational capacity. Also, due to the considerable computational efficiency gained we are able to produce an in-depth exploration of the model, its parameters and physical conditions. These findings further support the validity of the QGD equations use to simulate the dynamics of the plasma dynamics.

In the single-gas experiments we were able to complete a thorough investigation of the effects on solutions of a wide range of initial conditions as well as the varying of numerical and physical parameters of the problem. The numerical schemes robustness allows for the application of initial conditions which more accurately mimic the physical problem being studied. In particular, we are able to compute solutions when the initial pressure and temperature are raised to the order of magnitude that is present in physical experiments while, importantly,

holding the pressure and temperature in the ambient atmosphere at the low orders of magnitude that are representative of the what is experienced in the laboratory. In previous numerical experiments, the increase in the strike zone's initial conditions was necessarily matched by a proportional increase in the initial conditions of the ambient atmosphere. Also, thanks to the efficiency gained by the application of the numerical scheme, we were able to run a plethora of numerical experiments in order to balance the interplay of the numerical parameters used to control numerical dissipation, artificial viscosity and time stepping in order to achieve the optimal balance between efficiency and accuracy. Finally, we are able to compute solutions to the one-dimensional laser ablation problem using Navier-Stokes to model the expansion. This had previously not been done due to the difficult constraints demanded by the stiffness of the problem. Also, we were able to compare this result with those computed using the quasi-gas dynamics model as well as those previously computed in [72]. Although the Navier-Stokes simulation provides a sharper resolution of the expansion that more accurately represents the physical experiments, the extreme computational savings of the QGD model more than compensates for the extra smoothing experienced with its use. Furthermore, we were able to show that the artificial viscosity provided by the relaxation parameter could effectively be decoupled from the solution, thus allowing for simpler numerical approximations and additional time savings. In fact, we were able to produce results that better approached the NS simulations than did the QGD simulations. Although the computational time in these experiments were longer than the QGD simulations, they were still only a fraction of the full NS computational time.

The Binary gas experiment saw similar accomplishments. Along with increased efficiency and better shock resolution, we saw better control over shock drift. In particular, we were able to align the propagation of the fronts for each gas. Previously, this alignment was not seen as the numerical approximations of the fronts were not aligned. Also, we were able to run a similar analysis on the relaxation parameter and found that the constant τ models provided both increased resolution and better efficiency than the full QGD model.

The radially symmetric model provides results that form the basis of two-dimensional investigation. Not only do the results give us insight into the behavior of the two-dimensional problem, the always act as a verification of the two-dimensional results. Furthermore, they provide an excellent starting point for the approximation of the three-dimensional problem. The lightning-fast computational speeds achieved using the radially symmetric model can be leveraged to build a three-dimensional numerical simulation, using radial symmetry on the ground plane.

The two-dimensional results provide a qualitative and quantitative view of the problem that had not been previously available to researchers. The qualitative analysis provided by this simulation will provide researchers with an effective tool in analyzing the dynamics of the plasma expansion under varying physical conditions. Also, quantitatively the results provide a

breadth and depth that was not available in the one-dimensional solutions. Most importantly, we are able to accurately model the elongated expansion of the plasma jet as it propagates along the substrate. By being able to vividly capture the picture of the expansion, while retaining the ability to drill down on physical parameters, we have provided researchers with a valuable tool in the exploration of the dynamics of this problem.

In the future we would like to conduct further numerical investigations of the full two-dimensional quasi-gas dynamics model applied to the laser ablation problem to confirm it effectiveness at modeling the plasma expansion. Optimization of the two-dimensional numerical scheme will allow for a full exploration of the physical parameters that affect the quality of thin film growth. Furthermore, we plan to work towards a three-dimensional simulation. Although a full three-dimensional simulation may be beyond the scope of computational capacity, we are looking to other techniques to provide a three-dimensional approximation. Included in the ideas for this are parallelization and using the radially symmetric model to obtain a quasi three-dimensional model.

REFERENCES

[1] R. Abgrall, *On essentially non-oscillatory schemes on unstructured meshes: analysis and implementation*, J. Comput. Phys. **114** (1994), 45–58.

[2] ———, *How to prevent pressure oscillations in multicomponent flow calculations: A quasiconservaive approach*, J. Comput. Phys. **125** (1996), 150–160.

[3] D. J. Acheson, *Elementary fluid dynamics*, Clarendon Press Oxford, 1990.

[4] A. Alcrudo and P. Garcia-Navarro, *A high resolution godunov-type scheme in finite volumes for the 2d shallow water equations*, Internat. J. Numer. Meth. Fluids **16** (1993), 489–505.

[5] W. Anderson, J. L. Thomas, and B. van Leer, *Comparison of finite volume flux vecor splittings for the euler equations*, AIAA Journal **24** (1986), 1453–1460.

[6] A. A. Andreev, P. V. Nickles, and K. Yu. Platonov, *Quasi-coulomb explosion of multicomponent laser cluster plasma*, Physics of Plasmas **17** (2010), no. 2, 023110–6.

[7] P. Arminjon and M.-C. Viallon, *Généralisation du schéma de Nessyahu-Tadmor pour une équation hyperbolique à deux dimensions d'espace*, C. R. Acad. Sci. Paris Sér. I Math. **320** (1995), no. 1, 85–88.

[8] P. Arminjon, M.-C. Viallon, and A. Madrane, *A finite volume extension of the lax-friedrichs and nessyahu-tadmor schemes for conservation laws on unstructured grids*, Int. J. Comput. Fluid Dyn. **9** (1997), 1–22.

[9] U. M. Ascher, *Numerical methods for evolutionary differential equations*, Society for Industrial and Applied Mathematics, 2008.

[10] F. Bassi and S. S. Rebay, *High-order accurate discontinuous finite element method for the numerical solution of the compressible navier-stokes equations*, J. Comput. Phys. **131** (1997), 267–279.

[11] G. K. Batchelor, *An introduction to fluid dynamics*, Cambridge University Press, Cambridge, 1999.

[12] E. Becker, *Gas dynamics*, Academic Press, 1968.

[13] M. Ben-Artzi, *Application of the generalised riemann problem method to 1-d compressible flows with interfaces*, J. Comput. Phys. **65** (1986), 170–178.

[14] M. Ben-Artzi and J. Falcovitz, *Generalized Riemann problems in computational fluid dynamics*, Cambridge Monographs on Applied and Computational Mathematics, vol. 11, Cambridge University Press, Cambridge, 2003.

[15] M. J. Berger and J. Oliger, *Adaptive mesh refinement for hyperbolic partial differential equations*, J. Comput. Phys. **53** (1984), 484–512.

[16] L. Bermudez and M. E. Vazquez, *Upwind methods for hyperbolic conservation laws with source terms*, Computers and Fluids **23** (1994), no. 1049-1071.

[17] F. Bianco, G. Puppo, and G. Russo, *High order central schemes for hyperbolic systems of conservation laws*, SIAM J. Sci. Comput **21** (1999), 294–322.

[18] G. A. Bird, *Molecular gas dynamics and the direct simulation of gas flows*, Oxford Engineering Science Series, vol. 42, The Clarendon Press Oxford University Press, New York, 1995.

[19] F. Bouchut, *Nonlinear stability of finite volume methods for hyperbolic conservation laws and well-balanced schemes for sources*, Frontiers in Mathematics, Birkhäuser Verlag, Basel, 2004.

[20] S. Bryson, Y. Epshteyn, A. Kurganov, and G. Petrova, *Well-balanced positivity preserving central-upwind scheme on triangular grids for saint-venant system*, M2AN Math. Model. Numer. Anal. (To Appear).

[21] S. Bryson and D. Levy, *High-order weno schemes for multidimensioanl hamilton-jacobi equations*, SIAM J. Numer. Anal. **41** (2003), 1339–1369.

[22] V. Bychenkov and V. Kovalev, *Coulomb explosion in a cluster plasma*, Plasma Physics Reports **31** (2005), no. 2, 178–183.

[23] M. Capitelli, A. Casavola, G. Colonna, and A. De Giacomo, *Laser-induced plasma expansion: theoretical and experimental aspects*, Spectrochimica Acta Part B: Atomic Spectroscopy **59** (2004), no. 3, 271–289.

[24] E. J. Caramana, M. J. Shashkov, and P. P. Whalen, *Formulations of artificial viscosity for multi-dimensional shock wave computations*, J. Comput. Phys. **144** (1998), 70–97.

[25] Carasso, Raviart, and Serre (eds.), *Proc. first international conference on hyperbolic problems*, Springer, 1986.

[26] T. Chang, G. Q. Chen, and S. Yang, *On the 2-d riemann problem for the compressible euler equations i. interaction of shocks and rarefacion waves*, Discrete Contin. Dynam. Systems **1** (1995), 555–584.

[27] ———, *On the 2-d riemann problem for the compressible euler equations ii. interaction of contact discontinuities*, Discrete Contin. Dynam. Systems **6** (2000), 419–430.

[28] A. Chertock and A. Kurganov, *A simple eulerian finite-volume mthod for compressible fluids in domains with moving boundaries*, Commun. Math. Sci. **6** (2008), 531–556.

[29] A. J. Chorin and J. E. Marsden, *A mathematical introduction to fluid mechanics*, Springer-Verlag, 1993.

[30] J. F. Clarke and M. McChesney, *Dynamics of relaxing gases*, Butterworths, 1976.

[31] B. Cockburn, C. Johnson, C.-W. Shu, and E. Tadmor, *Advanced numerical approximation of nonlinear hyperbolic equations*, CIME Lecture Notes (A. Quarteroni, ed.), Lecture Notes in Mathematics, vol. 1697, Springer-Verlag, 1998.

[32] J. Collins and P. Gremaud, *A simple model for laser drilling*, Mathematics and Computers in Simulation (2010).

[33] L. A. Constantin and A. Kurganov, *Adaptive central-upwind schemes for hyperbolic systems of conservation laws*, Hyperbolic problems: theory, numeric and applications, Yokohama Publishers, 2006, pp. 95–103.

[34] S. D. Conte and C. de Boor, *Elementary numerical analysis*, McGraw-Hill Kogakusha Ltd., 1980.

[35] T. G. Elizarova, *Quasi-gasdynamic equations and numerical methods for viscous flow simulations*, Nauchnyi Mir, Moscow (in Russian), 2007.

[36] T. G.. Elizarova, V. A. Trofimov, and I. A. Shirokov, *Computer simulation of perturbation of a shock wave in nitrogen by optical radiation*, Tech. Phys. **53** (2008), no. 4, 408–414.

[37] B. Engquist and B. Gustafsson (eds.), *Proc. third international conference on hyperbolic problems, vol. i and ii*, Chartwell-Bratt, 1991.

[38] C. W. Gear, *Numerical initial-value problems in ordinary differential equations*, Prentice Hall, Englewood Cliffs, New Jersey, 1971.

[39] A. Glaser and V. Rokhlin, *A new class of highly accurate solvers for ordinary differential equations*, J. Sci. Comput. **38** (208), no. 3, 368–399.

[40] J. Glimm, J. Graham, J. W. Grove, and B. J. Plohr (eds.), *Proc. fifth international conference on hyperbolic problems*, World Scientific, 1996.

[41] E. Godlewski and P.-A. Raviart, *Numerical approximation of hyperbolic systems of conservation laws*, Applied Mathematical Sciences, vol. 118, Springer-Verlag, New York, 1996.

[42] S. K. Godunov, *A difference method for numerical calculation of discontinuous solutions of the equations of hydrodynamics*, Mat. Sb. (N.S.) **47 (89)** (1959), 271–306.

[43] S. Gottlieb, C. Shu, and E. Tadmor, *Strong stability-preserving high-order time discretization methods*, SIAM Review **43** (2001), no. 1, 89–112.

[44] E. Hairer and G. Wanner, *Solving ordinary differential equations i, non-stiff problems*, Springer, Berlin, 1993.

[45] ———, *Solving ordinary differential equations ii, stiff and differential-algebraic problems*, Springer, Berlin, 1996.

[46] M. Han, Y. Crong, and J. Zhou, *Plume dynamics during film and nanoparticles deposition by pulsed laser ablation*, Phys. Lett. A **302** (2002), 182–189.

[47] A. Harten, *High resolution schemes for hyperbolic conservation laws*, J. Comput. Phys. **49** (1983), 357–393.

[48] A. Harten, B. Engquist, S. Osher, and S.R. Chakravarthy, *Uniformly high-order accurate essentially nonoscillatory schemes. III*, J. Comput. Phys. **71** (1987), no. 2, 231–303.

[49] A. Harten and J. M. Hyman, *Self-adjusting grid methods for one-dimensional hyperbolic conservation laws*, J. Comput. Phys. **50** (1983), 235–269.

[50] A. Harten and S. Osher, *Uniformly high-order accurate nonoscillatory schemes. I*, SIAM J. Numer. Anal. **24** (1987), no. 2, 279–309.

[51] F. B. Hildebrand, *Introduction to numerical analysis*, Tata McGraw-Hill, New Delhi, 1974.

[52] A. C. Hindmarsh, *Odepack: A systematized collection of ode solvers*, IMACS Transactions in Scientific Computing **1** (1983), 55.

[53] L. Hormander, *Lectures on nonlinear hyperbolic differential equations*, Mathematiques et Applications **26** (1997).

[54] T. E. Itima, J. Hermann, and Ph. Delaporte, *Combined continuous-microsopic modeling of laser plume expansion*, Appl. Surf. Sci. **208-209** (2003), 27–32.

[55] G.-S Jiang and C.-W. Shu, *Efficient implementation of weighted ENO schemes*, J. Comput. Phys. **126** (1996), no. 1, 202–228.

[56] G.-S. Jiang and E. Tadmor, *Nonoscillatory central schemes for multidimensional hyperbolic conservation laws*, SIAM J. Sci. Comput. **19** (1998), no. 6, 1892–1917 (electronic).

[57] F. John, *Partial differential equations*, Springer-Verlag, 1982.

[58] L. W. Johnson and R. D. Riess, *Numerical analysis*, Addison-Wesley, 1982.

[59] D. Kahaner, C. Moler, and S. Nash, *Numerical methods and software*, Prentice Hall, Englewood Cliffs, New Jersey, 1989.

[60] D. I. Ketcheson, *High order strong stability preserving time integrators and numerical wave propagation methods for hyperbolic pdes*, Ph.D. thesis, University of Washington, 2009.

[61] Thomas C. Killian, *Plasma physics: Cool vibes*, Nature **441** (2006), 297.

[62] D. Kröner, *Numerical schemes for conservation laws*, Wiley-Teubner Series Advances in Numerical Mathematics, John Wiley & Sons Ltd., Chichester, 1997.

[63] P. K. Kundu and I. M Cohen, *Fluid mechanics*, Elsevier, 2008.

[64] A. Kurganov and D. Levy, *Third-order semi-discrete central scheme for conservation laws and convection-diffusion equations*, SIAM J. Sci. Comput. **22** (2000), 1461–1488.

[65] A. Kurganov and C.-T. Lin, *On the reduction of numerical dissipation in central-upwind schemes*, Commun. Comput. Phys. **2** (2007), 141–163.

[66] A. Kurganov, S. Noelle, and G. Petrova, *Semidiscrete central-upwind schemes for hyperbolic conservation laws and hamilton-jacobi equations*, SIAM J. Sci. Comput. **23** (2001), no. 3, 707–740.

[67] A. Kurganov and G. Petrova, *Central schemes and contact discontinuities*, M2AN Math. Model. Numer. Anal. **34** (2000), no. 6, 1259–1275.

[68] _____, *A third-order semi-discrete genuinely multidimensional central scheme for hyperbolic conservation laws and related problems*, Numer. Math. **88** (2001), no. 4, 683–729.

[69] _____, *Central-upwind schemes on triangular grids for hyperbolic systems of conservation laws*, Numer. Methods Partial Differential Equations **21** (2005), 536–552.

[70] A. Kurganov and A. Tadmor, *New high-resolution schemes for nonlinear conservation laws and convection diffusion equations*, J. Comput. Phys. **160** (2000), 241–282.

[71] A. Kurganov and E. Tadmor, *Solution of two-dimensional riemann problems for gas dynamics without riemann problem solvers*, Numer. Methods Partial Differential Equations **18** (2002), 584–608.

[72] Yu. Ya. Kuzyakov, V. A. Trofimov, and I. A. Shirokov, *Computer simulation of graphite target abltion under the action of a nanosecond laser pulse*, Tech. Phys. **53** (2008), no. 2, 154–159.

[73] J. D. Lambert, *Computational methods in ordinary differential equations*, John Wiley & Sons Ltd., 1973.

[74] L. D. Landau and E. M. Lifshitz, *Fluid mechanics*, Translated from the Russian by J. B. Sykes and W. H. Reid. Course of Theoretical Physics, Vol. 6, Pergamon Press, London, 1959.

[75] P. D. Lax and X.-D. Liu, *Solution of two-dimensional riemann problems of gas dynamics by positive schemes*, SIAM J. Sci. Comput. **19** (1998), 319–340.

[76] R. LeVeque, *Finite difference methods for ordinary and partial differential equations*, Society for Industrial and Applied Mathematics, 2007.

[77] R. J. LeVeque, *Finite volume methods for hyperbolic problems*, Cambridge Texts in Applied Mathematics, Cambridge University Press, Cambridge, 2002.

[78] D. Levy, G. Puppo, and G. Russo, *Central WENO schemes for hyperbolic systems of conservation laws*, M2AN Math. Model. Numer. Anal. **33** (1999), no. 3, 547–571.

[79] _____, *Compact central WENO schemes for multidimensional conservation laws*, SIAM J. Sci. Comput. **22** (2000), no. 2, 656–672 (electronic).

[80] Z. Li and K. Ito, *The immersed interface method*, SIAM, Philadelphia, PA, 2006.

[81] K.-A. Lie and S. Noelle, *An improved quadrature rule for the flux-computation in staggered central difference schemes in multidimensions*, J. Sci. Comput. **63** (2003), 1539–1560.

[82] _____, *On the artificial compression method for second-order nonoscillatory central difference schemes for systems of conservation laws*, SIAM J. Sci. Comput. **24** (2003), no. 4, 1157–1174.

[83] _____, *On the artificial compression method for second-order nonoscillatory central difference schemes for systems of conservation laws*, SIAM J. Sci. Comput. **24** (2003), no. 4, 1157–1174.

[84] W. B. Lindquist (ed.), *Current progress in hyperbolic systems: Riemann problems and computations*, American Mathematical Society, 1989.

[85] S.F. Liotta, V. Romano, and G. Russo, *Central schemes for balance laws of relaxation type*, SIAM J. Numer. Anal. **38** (2000), 1337–1356.

[86] X.-D. Liu and S. Osher, *Nonoscillatory high order accurate self-similar maximum principle satisfying shock capturing schemes. I*, SIAM J. Numer. Anal. **33** (1996), no. 2, 760–779.

[87] X.-D. Liu, S. Osher, and T. Chan, *Weighted essentially non-oscillatory schemes*, J. Comput. Phys. **115** (1994), no. 1, 200–212.

[88] X.-D. Liu and E. Tadmor, *Third order nonoscillatory central scheme for hyperbolic conservation laws*, Numer. Math. **79** (1998), no. 3, 397–425.

[89] A. Majda and A. L. Bertozzi, *Vorticity and incompressible flow*, Cambridge University Press, 2002.

[90] M. J. Maron and R. J. Lopez, *Numerical analysis*, Wadsworth, 1991.

[91] J. H. Mathews, *Numerical methods*, Prentice Hall International, Inc., 1987.

[92] R. C. McOwen, *Partial differential equations methods and applications*, Prentice Hall, 2003.

[93] A. A. Medovikov, DUMKA 3 code available at `http://www.math.tulane.edu/~amedovik/`.

[94] _____, *High order explicit methods for parabolic equations*, BIT **38** (1998), no. 2, 372–390.

[95] H. Nessyahu and E. Tadmor, *Nonoscillatory central differencing for hyperbolic conservation laws*, J. Comput. Phys. **87** (1990), no. 2, 408–463.

[96] L. Pareschi, *Central differencing based numerical schemes for hyperbolic conservation laws with relaxation terms*, SIAM J. Numer. Anal. **39** (2001), 1395–1417.

[97] L. Pareschi, G. Puppo, and G. Russo, *Central Runge-Kutta schemes for conservation laws*, SIAM J. Sci. Comput. **26** (2005), no. 3, 979–999 (electronic).

[98] L. Pareschi and G. Russo, *Implicit-Explicit Runge-Kutta schemes and applications to hyperbolic systems with relaxation*, J. Sci. Comput. **25** (2005), no. 1-2, 129–155.

[99] Y. Pinchover and J. Rubinstein, *An introduction to partial differential equations*, Cambridge University Press, 2005.

[100] G. Russo, *Central schemes and systems of balance laws*, Hyperbolic partial differential equations (Hamburg, 2001), Vieweg, Braunschweig, 2002, pp. 59–114.

[101] S. Schecter and M. Shearer, *Undercompressive shocks for nonstrictly hyperbolic conservation laws*, J. Dynamics and Different. Eq. **3** (1989), no. 2, 199–271.

[102] F. W. Sears and G. L. Salinger, *Thermodynamics, kinetic theory and statistical thermodynamics*, Addison-Wesley, 1986.

[103] L. F. Shampine, *Numerical solution of ordinary differential equations*, Chapman and Hall, 1994.

[104] M. Shearer, *The riemann problem for 2x2 systems of hyperbolic conservation laws*, J. Different. Eq. **80** (1989), 343–363.

[105] J. Shi, C. Hu, and C.-W. Shu, *A technique of treating negative weights in weno schemes*, J. Comput. Phys. **175** (2002), no. 1, 108–127.

[106] C.-W. Shu, *High-order finite difference and finite volume WENO schemes and discontinuous Galerkin methods for CFD*, Int. J. Comput. Fluid Dyn. **17** (2003), no. 2, 107–118.

[107] C. W. Shulz-Rinne, *Classificaion of the riemann problem for two-dimensional gas dynamics*, SIAM J. Math. Anal. **24** (1993), 76–88.

[108] C. W. Shulz-Rinne, J. P. Collins, and H. M. Glaz, *Numerical solution of the riemann problem for two-dimensional gas dynamics*, SIAM J. Sci. Comput. **14** (1993), 1394–1394.

[109] R. K. Singh and J. Narayan, *Pulsed-laser evaporation technique for deposition of thin films: Physics and theoretical model*, Physical Review B **41** (1990), no. 13, 8843–859.

[110] G. A. Sod, *A survey of several finite difference methods for systems of nonlinear hyperbolic conservation laws*, J. Comput. Phys. **27** (1978), 1–31.

[111] W. A. Strauss, *Partial differential equations an introduction*, John Wiley & Sons, Inc., 1992.

[112] P.K. Sweby, *High resolution schemes using flux limiters for hyperbolic conservation laws*, SIAM J. Numer. Anal. **21** (1984), no. 5, 995–1011.

[113] E. Tadmor, *"recent advances in partial differential equations and applications" proceedings of a conference in honor of the 70th birthdays of peter d. lax and louis nirenberg*, Approximate solution of nonlinear conservation laws and related equations (Venice) (R. Spigler and S. Venakides, eds.), vol. 54, American Mathematical Society, AMS Proceedings of Symposia in Applied Mathematics, June 1998, pp. 325–368.

[114] E.F. Toro, *Riemann solvers and numerical methods for fluid dynamics: A practical introduction*, third ed., Springer-Verlag, Berlin, Heidelberg, 2009.

[115] V. A. Trofimov and I. A. Shirokov, *Computer simulation of expansion of a carbon laser plasma after ablation in nitrogen atmosphere*, Tech. Phys. **54** (2009), no. 7, 974–980.

[116] A. Tveito and R. Winther, *Introduction to partial differential equations*, Springer-Verlag, 1998.

[117] B. van Leer, *Towards the ultimate conservative difference scheme. V. A second-order sequel to Godunov's method*, J. Comput. Phys. **32** (1979), no. 1, 101–136.

[118] M. L. Wilkins, *Use of artificial viscosity in multidimensional fluid dynamic calculations*, J. Comput. Phys. **36** (1980), 281–303.

[119] E. C. Zachmanoglou and D. W. Thoe, *Introduction to partial differential equations*, Dover Publications, Inc., 1986.

APPENDIX

Appendix A

Mathematics

A.1 Eigenvalues of the Flux Jacobian

A.1.1 One-dimensional Case

In the approximation of conservation laws using the semi-discrete upwind method developed in [66], the local speeds of propagation are prescribed using the eigenvalues of the Jacobian of the hyperbolic flux. The vector of conservative variables are given as $\mathbf{u} = (\rho, \rho u, E)^T = (u_1, u_2, u_3)^T$. The equation of state represented in this context is given below.

$$p = (\gamma - 1)(E - \frac{\rho u^2}{2}) = (\gamma - 1)(u_3 - \frac{u_2^2}{2u_1}) \tag{A.1}$$

The hyperbolic flux is given as

$$\mathbf{F}(\mathbf{u}) = \begin{pmatrix} \rho u \\ \rho u^2 + p \\ u(E+p) \end{pmatrix} = \begin{pmatrix} u_2 \\ \frac{u_2^2}{u_1} + (\gamma - 1)(u_3 - \frac{u_2^2}{2u_1}) \\ \frac{u_2}{u_1}(u_3 + (\gamma - 1)(u_3 - \frac{u_2^2}{2u_1})) \end{pmatrix}. \tag{A.2}$$

The Jacobian, J, of a vector- valued function is defined as the matrix of all first- order partial derivatives with respect to the independent vector. For example, if $F = (F_1(x_1, ..., x_n), ..., F_m(x_1, ...x_n))^T$, then

$$J = \begin{pmatrix} \frac{\partial F_1}{\partial x_1} & \cdots & \frac{\partial F_1}{\partial x_n} \\ \vdots & \ddots & \vdots \\ \frac{\partial F_m}{\partial x_1} & \cdots & \frac{\partial F_m}{\partial x_n} \end{pmatrix} \tag{A.3}$$

So, in order to compute the Jacobian for the hyperbolic flux function, (A.2), we must compute the partial derivatives. These are computed below. Recall the formula for enthalpy is $H =$

$\frac{(E+p)}{\rho}$. This formula is used in the following to simplify some of the expressions.

$$
\begin{aligned}
&\frac{\partial u_2}{\partial u_1} = 0, \quad \frac{\partial u_2}{\partial u_2} = 1, \quad \frac{\partial u_2}{\partial u_3} = 0, \\
&\frac{\partial}{\partial u_1}\left(\frac{u_2^2}{u_1} + p\right) = -\frac{u_2^2}{u_1^2} + (\gamma-1)(\frac{u_2^2}{2u_1^2}) = \frac{u^2}{2}(\gamma-3) \\
&\frac{\partial}{\partial u_2}\left(\frac{u_2^2}{u_1} + p\right) = \frac{2u_2}{u_1} + (\gamma-1)(-\frac{u_2}{u_1}) = u(3-\gamma) \\
&\frac{\partial}{\partial u_3}\left(\frac{u_2^2}{u_1} + p\right) = \gamma - 1 \\
&\frac{\partial}{\partial u_1}\left(\frac{u_2}{u_1}(u_3+p)\right) = -\frac{u_2}{u_1^2}(u_3+p) + \frac{u_2}{u_1}\left((\gamma-1)(\frac{u_2^2}{2u_1^2})\right) = \frac{u^3}{2}(\gamma-1) - uH \\
&\frac{\partial}{\partial u_2}\left(\frac{u_2}{u_1}(u_3+p)\right) = \frac{1}{u_1}(u_3+p) + \frac{u_2}{u_1}\left((\gamma-1)(-\frac{u_2}{u_1})\right) = H - (\gamma-1)u^2 \\
&\frac{\partial}{\partial u_3}\left(\frac{u_2}{u_1}(u_3+p)\right) = \frac{u_2}{u_1}(1+(\gamma-1)) = \gamma u
\end{aligned}
$$

Therefore, the Jacobian of the hyperbolic flux is

$$
\mathbf{F}'(\mathbf{u}) = \begin{pmatrix} 0 & 1 & 0 \\ \frac{u^2}{2}(\gamma-3) & u(3-\gamma) & \gamma-1 \\ \frac{u^3}{2}(\gamma-1) - uH & H-(\gamma-1)u^2 & \gamma u \end{pmatrix}. \tag{A.4}
$$

Now, to find the eigenvalues of the Jacobian we must solve for the roots of the characteristic equation, which is given by

$$
\det \begin{pmatrix} 0-\lambda & 1 & 0 \\ \frac{u^2}{2}(\gamma-3) & u(3-\gamma)-\lambda & \gamma-1 \\ \frac{u^3}{2}(\gamma-1) - uH & H-(\gamma-1)u^2 & \gamma u - \lambda \end{pmatrix} = 0. \tag{A.5}
$$

The characteristic equation can be simplified to the following.

$$
-\lambda^3 + 3u\lambda^2 + \left(-\frac{u^2}{2}(5+\gamma) + (\gamma-1)H\right)\lambda + \left(\frac{u^3}{2}(\gamma+1) - (\gamma-1)uH\right) = 0 \tag{A.6}
$$

It can easily be checked that the eigenvalues of the hyperbolic flux, $u-c, u, u+c$ (where u is the velocity and c is the speed sound), satisfy this equation.

A.1.2 Quasi Two-dimensional Radially Symmetric Case

In the quasi two-dimensional radially symmetric case, the vector of conservative variables are given as $\mathbf{w} = (r\rho, r\rho u, rE)^T = (w_1, w_2, w_3)^T$, where r is the spatial variable. In this case, we

will see that the variable r is cancelled out in the calculations of the partial derivatives and we end up with same Jacobian and eigenvalues as in the one-dimensional case. The hyperbolic flux is given below and is in the same form as the flux given in (A.2).

$$\mathbf{F}(\mathbf{w}) = \begin{pmatrix} r\rho u \\ r(\rho u^2 + p) \\ ru(E+p) \end{pmatrix} = \begin{pmatrix} w_2 \\ \frac{w_2^2}{w_1} + (\gamma-1)(w_3 - \frac{w_2^2}{2w_1}) \\ \frac{w_2}{w_1}(w_3 + (\gamma-1)(w_3 - \frac{w_2^2}{2w_1})) \end{pmatrix} \tag{A.7}$$

Thus, the partial derivatives are of the same form as in the one-dimensional case. It is easily seen that the simplification of the partial derivative expressions results in the elimination of the spatial variable r. Note that the equation of state in terms of these conservative variables is actually r times pressure. I.e.,

$$\begin{aligned} (\gamma-1)\left(w_3 - \frac{1}{2}\frac{w_2^2}{w_1}\right) &= (\gamma-1)\left(rE - \frac{1}{2}\frac{(r\rho u)^2}{r\rho}\right) \\ &= (\gamma-1)\left(rE - \frac{1}{2}r\rho u^2\right) \\ &= r(\gamma-1)\left(E - \frac{1}{2}\rho u^2\right) = rp \end{aligned} \tag{A.8}$$

Take for example the partial derivative of the third component of the flux with respect to u_2.

$$\begin{aligned} \frac{\partial}{\partial w_2}\left(\frac{w_2}{w_1}(w_3 + rp)\right) &= \frac{1}{w_1}(w_3 + rp) + \frac{w_2}{w_1}\left((\gamma-1)(-\frac{w_2}{w_1})\right) \\ &= \frac{1}{r\rho}(rE + rp) + u(\gamma-1)(-u) \\ &= H - (\gamma-1)u^2 \end{aligned} \tag{A.9}$$

Thus we end up with the same Jacobian matrix, which of course leads us to the same eignevalues, namely $u-c, u, u+c$.

A.1.3 Two-dimensional Case

Now we consider the full two-dimensional flux function in the x direction. The conservative variable vector is given as $(\rho, \rho u, \rho v, E)^T = (u_1, u_2, u_3, u_4)^T$. The equation of state is given below.

$$p = (\gamma-1)(E - \frac{\rho(u^2+v^2)}{2}) = (\gamma-1)(u_4 - \frac{u_2^2 + u_3^2}{2u_1}) \tag{A.10}$$

The hyperbolic flux is given as

$$\mathbf{F}(\mathbf{u}) = \begin{pmatrix} \rho u \\ \rho u^2 + p \\ \rho uv \\ u(E+p) \end{pmatrix} = \begin{pmatrix} u_2 \\ \frac{u_2^2}{u_1} + (\gamma - 1)(u_4 - \frac{u_2^2 + u_3^2}{2u_1}) \\ \frac{u_2 u_3}{u_1} \\ \frac{u_2}{u_1}(u_4 + (\gamma - 1)(u_4 - \frac{u_2^2 + u_3^2}{2u_1})) \end{pmatrix}. \tag{A.11}$$

To simplify notation, let $f_{ij} = \frac{\partial f_i}{\partial u_j}$. Then the Jacobian matrix is written as

$$\mathbf{F}'(\mathbf{u}) = \begin{pmatrix} f_{11} & f_{12} & f_{13} & f_{13} \\ f_{21} & f_{22} & f_{23} & f_{24} \\ f_{31} & f_{32} & f_{33} & f_{34} \\ f_{41} & f_{42} & f_{43} & f_{44} \end{pmatrix}. \tag{A.12}$$

After calculating these derivatives and performing the necessary operation to obtain the eigenvalues, we find a the eigenvalues for the two-dimensional Euler flux are given by $u-c, u, u, u+c$.